

University of Southampton Research Repository

Copyright © and Moral Rights for this thesis and, where applicable, any accompanying data are retained by the author and/or other copyright owners. A copy can be downloaded for personal non-commercial research or study, without prior permission or charge. This thesis and the accompanying data cannot be reproduced or quoted extensively from without first obtaining permission in writing from the copyright holder/s. The content of the thesis and accompanying research data (where applicable) must not be changed in any way or sold commercially in any format or medium without the formal permission of the copyright holder/s.

When referring to this thesis and any accompanying data, full bibliographic details must be given, e.g.

Thesis: Author (Year of Submission) "Full thesis title", University of Southampton, name of the University Faculty or School or Department, PhD Thesis, pagination.

Data: Author (Year) Title. URI [dataset]

University of Southampton

Faculty of Engineering and Physical Sciences

Optoelectronics Research Centre

Optoelectronic Oscillators with Hollow-core Fibres

by

Udara Sandamal Mutugala

Thesis for the degree of Doctor of Philosophy

June 2019

University of Southampton

Abstract

Faculty of Physical Sciences and Engineering

Optoelectronics Research Centre

Thesis for the degree of Doctor of Philosophy

Optoelectronic Oscillators with Hollow-core Fibres

by

Udara Sandamal Mutugala

Optoelectronic oscillators (OEOs) are capable of generating microwave signals with high spectral purity (i.e. with high short-term stability) using optical energy sources and optical energy storage elements. Optical fibre delay-lines are commonly used in OEOs as the optical energy storage element and the spectral purity of the generated microwave signals can be increased by increasing the length of the incorporated optical fibre. However since the delay induced by an optical fibre is susceptible to temperature, the ambient temperature induced delay changes in the optical fibre can vary the OEO output signal frequency (by varying loop delay), degrading the long-term stability of the OEO.

This thesis investigates the temperature stability improvement that can be obtained by replacing standard SMF delay-lines in OEOs with long-length hollow-core photonic bandgap fibres (HC-PBGFs). Using 860 m long HC-PBGF with 19-cell core structure, it is shown that when the temperature sensitivity of the HC-PBGF is limited by temperature induced length changes, a temperature stability improvement of more than 15 times can be achieved in an OEO by using a HC-PBGF delay-line instead of an SMF delay-line.

Furthermore by using a 1.09 km long 19-cell HC-PBGF it is shown that by operating the laser source in the OEO at the long-wavelength-edge of the bandgap of the HC-PBGF (where the group velocity gets increased when the temperature is increased), the effect of temperature induced fibre length changes in the HC-PBGF can be further reduced to reach zero and even negative temperature sensitive characteristics. Furthermore it is shown that within a 3 nm wide wavelength window, the temperature sensitivity of this particular fibre is at least 100 times lower than that of an SMF. Phase noise of the long-length HC-PBGF delay-line incorporated OEOs are measured and it is shown that phase noise degradation due to multipath interference in HC-PBGFs can be suppressed by modulating the laser source.

In order to suppress the undesired polarization properties of HC-PBGFs such as polarization dependent loss (PDL) and polarization mode coupling that could potentially degrade the performance of HC-PBGF delay-line incorporated OEOs, two passive fibre-optic depolarizers capable of depolarizing input signals with 20 MHz and 1 MHz linewidths were developed. The characterization results of these depolarizers are also shown in this thesis. These depolarizers are now being commercialized by Phoenix Photonics, UK.

Table of Contents

Table of Contents	i
Table of Figures	v
Research Thesis: Declaration of Authorship	xiii
List of Publications.....	xv
Acknowledgements	xvii
Definitions and Abbreviations.....	xix
Chapter 1 Introduction.....	1
1.1 Thesis Outline	3
Chapter 2 Optoelectronic Oscillator: Background	5
2.1 The Generic Architecture and Operation of an OEO	5
2.2 Obtaining Single-mode Oscillation without Narrow RF Band-Pass Filters.....	7
2.3 Multi-loop OEO Architectures.....	8
2.4 Types of Modulators in OEOs.....	11
2.5 Optical Energy Storage Elements in OEOs Other Than Optical Fibres	12
2.6 Applications of OEOs	13
Chapter 3 Optoelectronic Oscillator: Stability Characterization.....	15
3.1 Short-term Stability.....	15
3.1.1 Heterodyne Techniques	15
3.1.2 Homodyne Techniques.....	16
3.1.3 Photonic-delay Phase Noise Measurement Scheme	17
3.1.3.1 Delay-line Transfer Function	18
3.1.3.2 Measurement of Mixer Voltage Gain Coefficient (K_ϕ)	19
3.1.3.3 Noise Floor Estimation	20
3.1.3.4 Phase Noise Measurement and Processing	20
3.2 Long-term Stability	20
3.2.1 Long-term Frequency Stability Measurement Setup.....	20
3.2.1.1 Reference Signal Generation.....	21

Table of Contents

3.2.2 Allan Deviation	22
3.3 Long-term Stability of Optical Fibre Delay-line Based OEOs	22
3.3.1 Active Long-term Stabilization of OEOs.....	23
3.3.2 Temperature Sensitivity of Optical Fibres	24
Chapter 4 Hollow-core Photonic Bandgap Fibres	27
4.1 Guiding Mechanisms in Microstructured Optical Fibres	27
4.1.1 Index-guiding Fibres.....	27
4.1.2 Photonic-bandgap-guiding Fibres.....	28
4.1.3 Anti-resonant-guiding Fibres	28
4.2 Hollow-core Photonic Bandgap Fibres.....	29
4.2.1 Basics of HC-PBGF Fabrication.....	29
4.2.2 Properties and Applications of HC-PBGFs.....	30
4.2.2.1 Temperature Sensitivity of HC-PBGFs.....	32
Chapter 5 Passive Fibre-optic Depolarizers	35
5.1 Depolarizers in Terms of the Domain of Operation	35
5.2 Passive Fibre-optic Depolarizers for Fibre-optic Systems.....	37
Chapter 6 Incorporating Hollow-core Photonic Bandgap Fibre into Optoelectronic Oscillator	41
6.1 Background	41
6.2 Experimental Setup and Subsystems.....	41
6.2.1 Delay-lines.....	42
6.2.2 Custom EDFA.....	43
6.2.3 Bias-point Locking of the Modulator	44
6.2.4 Thermal Chamber	45
6.2.4.1 Thermal Chamber with Single Heating Element.....	45
6.2.4.2 Thermal Chamber with 10 Peltier Modules.....	46
6.2.5 The OEO Setup	47
6.3 Frequency Drift Measurements.....	48

6.3.1 Frequency Drift Due to All the Components of the OEO Loop	48
6.3.2 Frequency Drift Due to the Components in the OEO Loop Other Than the Delay-line.....	50
6.3.3 Minimum Frequency Drift of the OEO	52
6.3.4 Absolute Long-term Frequency Stability Improvement with the HC-PBGF Delay-line.....	53
6.4 TCD Calculations.....	55
6.5 Phase Noise Measurements.....	56
6.6 Conclusions.....	58
Chapter 7 Exploiting Zero-TCD Characteristics of Hollow-core Photonic Bandgap Fibres to Improve the Thermal Stability of Optoelectronic Oscillators	59
7.1 Introduction.....	59
7.2 Determination of the suitability of the Fibre	59
7.2.1 The 860-m Fibre	60
7.2.2 The 1090-m Fibre	61
7.3 The OEO Setup	63
7.4 Chromatic Dispersion Measurement from the OEO	64
7.5 Frequency Drift Measurements and TCD.....	66
7.6 Allan Deviation at 1610 nm	67
7.7 Phase Noise Measurements.....	68
7.7.1 Without Frequency Modulation of the Laser.....	68
7.7.2 With Frequency Modulation of the Laser	70
7.8 Conclusions.....	72
Chapter 8 Passive Fibre-optic Depolarizers for Narrow-linewidth Signal Depolarization: Configurations, Theoretical Analysis and Simulations	75
8.1 Depolarizer Configurations	75
8.1.1 PM-depolarizer.....	76
8.1.2 SMF-depolarizer	77
8.2 Theoretical Analysis of the Depolarizers.....	78
8.3 Simulations.....	80

Table of Contents

8.3.1 Effect of the Fluctuations of Centre Frequency (f_0) and Induced Time Delays (τ_1 and τ_2)	80
8.3.2 Delay-line Length Requirements	82
8.3.3 Dependency of the DOP on Coupling Ratio Variations of the Coupler	82
8.3.4 Dependency of DOP on Fibre Path Losses in Stage 1	83
8.3.5 Dependency of DOP on Fibre Path Losses in Stage 2	85
8.3.6 Indirect Estimation of Coupling Ratio of the Coupler	86
8.3.7 Dependency of PDL on Fibre Path Losses in Stage 1	86
8.3.8 Dependency of PDL on Fibre Path Losses in Stage 2	87
8.4 Conclusions	87
Chapter 9 Passive Fibre-optic Depolarizers for Narrow-linewidth Signal Depolarization: Fabrication and Characterization	89
9.1 Wavelength Dependency of Couplers	89
9.2 Depolarizer Fabrication Procedure	90
9.3 Depolarizer Characterization	91
9.3.1 Variable Linewidth Input Signal Generation	91
9.3.2 DOP Measurement Setups	93
9.4 Experimental Results	95
9.4.1 PM-depolarizer with 20 and 40 m Delay-lines	95
9.4.2 SMF-depolarizer with 10 and 20 m Delay-lines	96
9.4.3 SMF-depolarizer with 200 and 400 m Delay-lines	97
9.5 Conclusions	98
Chapter 10 Conclusions and Suggestions for Future Work	99
10.1 Suggestions for Future Work	102
Appendix A Analytical Formulas to Calculate how DOP and PDL is Affected by Coupling Ratio Imperfections and Fibre Path Losses	105
List of References	107

Table of Figures

Figure 2-1 Simplified schematic of a generic single-loop OEO. Optical paths are shown in black and electrical paths are shown in red.	5
Figure 2-2 Obtaining single-mode oscillation in an OEO.	6
Figure 2-3 Simplified schematic of a single-loop OEO with a Fabry-Perot etalon. Optical paths are shown in black and electrical paths are shown in red. Note: amplifying components are not shown.....	7
Figure 2-4 Simplified schematic of a dual-loop OEO. Optical paths are shown in black and electrical paths are shown in red. Note: amplifying components are not shown.	9
Figure 2-5 Simplified schematic of an injection locked dual OEO. Optical paths are shown in black and electrical paths are shown in red. Note: amplifying components are not shown.	10
Figure 2-6 Simplified schematic of a coupled-OEO. Optical paths are shown in black and electrical paths are shown in red. Note: electrical amplifying components are not shown.	11
Figure 2-7 Simplified schematic of a Whispering gallery mode (WGM) resonator based OEO. Optical paths are shown in black and electrical paths are shown in red. Note: amplifying components are not shown.	12
Figure 2-8 Simplified schematic of OEO based frequency comb generator [56]. Optical paths are shown in black and electrical paths are shown in red. Note: amplifying components are not shown.	14
Figure 3-1 Schematic of the photonic-delay phase noise measurement scheme. PC: polarization controller, MZM: Mach-Zehnder modulator, OPS: Optical phase shifter, DL: Delay-line, PD: Photodiode, RFA: RF amplification, ESA: Electrical spectrum analyser, VM: Volt meter, SUT: Signal under test. Optical paths are shown in black and electrical paths are shown in red.	17
Figure 3-2 Delay-line transfer function for three different delay-line lengths (100m, 1 km and 5 km).....	19

Table of Figures

Figure 3-3 Reference signal generation and frequency variation measurement setup. PD: Photodiode, RFA: RF amplification, BPF: Band-pass filter, FC: Frequency counter, SUT: Signal under test. Optical paths are shown in black and electrical paths are shown in red.....	21
Figure 4-1 Representative cross-sectional sketch of an index-guiding fibre. Solid core region is surrounded by an air-holed micro structure.....	27
Figure 4-2 Representative cross-sectional sketches of bandgap-guiding fibres. (a) 1-D case: core is surrounded by concentric high and low refractive index layers (Bragg fibre), (b) 2-D case: hollow-core is surrounded by a 2-dimensional periodic air-holed structure.....	28
Figure 4-3 Representative cross-sectional sketches of anti-resonant guiding fibres. (a) Kagomé latticed fibre, (b) nested anti-resonant fibre with simplified cladding structure.	29
Figure 5-1. Schematic of a fibre-Lyot depolarizer [121] with two jointed PM fibre sections with 1:2 length ratio. Birefringent axes of the two fibres are rotated by 45° with respect to each other.....	38
Figure 5-2. Schematic of an input-SOP independent Mach-Zehnder depolarizer with SMF delay-lines [123]. Two depolarizing stages are cascaded through a 50:50 coupler. PBS: Polarization Beam Splitter, PR: Polarization Rotator.	39
Figure 5-3 Schematic of an input-SOP independent Michelson depolarizer with SMF delay-lines [125]. Two depolarizing stages are cascaded through a wave-plate. PBS: Polarization Beam Splitter, PR: Polarization Rotator, FRM: Faraday rotator mirror.	40
Figure 6-1 (a) Cross-sectional SEM image of the 860 m long 19-cell HC-PBGF used as the delay-line (the SEM image was provided by S. R. Sandoghchi) and (b) the 860 m long 19-cell HC-PBGF spooled on a 16 cm diameter spool.	42
Figure 6-2 Insertion loss spectrum of the 860 m long HC-PBGF before splicing with SMF pigtailed (provided by T. D. Bradley).	43
Figure 6-3 Schematic of the custom EDFA. WDM: Wavelength division multiplexer, EDF: Erbium doped fibre.	44
Figure 6-4 The section of the custom EDFA that can be thermally insulated.	44

Figure 6-5 Schematic of the feedback control. TPD: Tap photodiode, TIA: Transimpedance amplifier, LPF: Low-pass filter, MZM, Mach-Zehnder modulator. Optical paths are shown in black and electrical paths are shown in red.....	45
Figure 6-6 Temperature variation inside a polystyrene box when the Arduino UNO microcontroller board based temperature control system was set to vary temperature between 30°C and 40°C with a 20 minutes settling time.	46
Figure 6-7 (a) Outside look and (b) inside look of the thermal chamber with 10 Peltier modules.	46
Figure 6-8 The 10 GHz single loop OEO setup. MZM: Mach-Zehnder modulator, EDFA: Erbium doped fibre amplifier, PC: Polarization controller, DL: Delay-line, Att.: Optical attenuator, PD: Photodiode, RFA: RF amplification, BPF: Band-pass filter. The components within the shaded area ('the other components in the OEO loop') can also induce frequency drifts due to temperature variations. Optical paths are shown in black and electrical paths are shown in red.....	47
Figure 6-9 (a) Frequency drift of the OEO with HC-PBGF delay-line and with SMF delay-line when the entire OEO setup was exposed to ambient temperature variations and (b) ambient temperature variation in the laboratory.....	48
Figure 6-10 Allan deviations of the OEO with HC-PBGF delay-line and with SMF delay-line when the entire OEO setup was exposed to ambient temperature variations.	49
Figure 6-11 All the components of the OEO except the delay-line are exposed to ambient temperature variations. MZM: Mach-Zehnder modulator, EDFA: Erbium doped fibre amplifier, PC: Polarization controller, DL: Delay-line, Att.: Optical attenuator, PD: Photodiode, RFA: RF amplification, BPF: Band-pass filter. Optical paths are shown in black and electrical paths are shown in red.....	50
Figure 6-12 (a) Frequency drift of the OEO with HC-PBGF delay-line and with SMF delay-line when all the components of the OEO except the delay-line were exposed to ambient temperature variations and (b) averaged temperature variation inside the insulation box the delay-lines were placed in.	51
Figure 6-13 Allan deviations of the OEO with HC-PBGF delay-line and with SMF delay-line when all the components of the OEO except the delay-line were exposed to ambient temperature variations.....	51

Table of Figures

Figure 6-14 All the components of the OEO loop are shielded from ambient temperature variations. MZM: Mach-Zehnder modulator, EDFA: Erbium doped fibre amplifier, PC: Polarization controller, DL: Delay-line, Att.: Optical attenuator, PD: Photodiode, RFA: RF amplification, BPF: Band-pass filter. Optical paths are shown in black and electrical paths are shown in red.	52
Figure 6-15 Allan deviation of the OEO with HC-PBGF delay-line when all the components of the OEO-loop were shielded from ambient temperature variations.	53
Figure 6-16 The delay-line is placed in the thermal chamber. The other components of the OEO loop are shielded from ambient temperature variations. MZM: Mach-Zehnder modulator, EDFA: Erbium doped fibre amplifier, PC: polarization controller, DL: delay-line, Att.: Optical attenuator, PD: photodiode, RFA: RF amplification, BPF: band-pass filter. Optical paths are shown in black and electrical paths are shown in red.	53
Figure 6-17 (a) Frequency drift of the OEO with HC-PBGF delay-line and with SMF delay-line when the delay-lines were inside the thermal chamber and the other components of the OEO loop were shielded from ambient temperature variations and (b) variation of temperature inside the thermal chamber for the two delay-lines.54	
Figure 6-18 RF spectrum of the 10 GHz OEO output signal (a) with HC-PBGF delay-line and (b) with SMF delay-line (span=3MHz, RBW=27 kHz).	56
Figure 6-19 Phase noise spectra of the OEO with HC-PBGF delay-line and with SMF-delay-line.57	
Figure 7-1 Chromatic dispersion profile of the 860-m fibre. The insertion loss of the fibre (before splicing SMF pigtails) over the same wavelength range is also shown.	60
Figure 7-2 (a) Cross sectional SEM image of the 1090-m HC-PBGF used as the delay-line (the SEM image was provided by S. R. Sandoghchi) and (b) the 1090-m HC-PBGF spooled on a 16 cm diameter spool.....	61
Figure 7-3 Simulated and measured chromatic dispersion profile of the 1090-m fibre. The insertion loss of the fibre (before splicing SMF pigtails) over the same wavelength range is also shown.	62
Figure 7-4 Insertion loss spectrum of the 1090-m fibre (provided by Y. Chen)	62
Figure 7-5 The 10 GHz single loop OEO setup. MZM: Mach-Zehnder modulator, PC: Polarization controller, DL: Delay-line, Att.: Optical attenuator, PD: Photodiode, RFA: RF	

amplification, BPF: Band-pass filter. The components within the blue area ('the other components in the OEO loop') are shielded from ambient temperature variations and the delay-line is placed inside the thermal chamber. Optical paths are shown in black and electrical paths are shown in red.....	63
Figure 7-6 RF spectrum of the 10 GHz OEO output signal with 1090-m HC-PBGF delay-line at 1550 nm (span=1.5 MHz, RBW=15 kHz).	64
Figure 7-7 RF spectra showing the change of the 10 GHz OEO output signal when operational wavelength was changed from 1569.5 nm to 1570 nm (span=750 kHz, RBW=6.8 kHz)	65
Figure 7-8 Chromatic dispersion of the 1090-m HC-PBGF delay-line measured by the change of OEO output signal. Chromatic dispersion measured by the free-space Mach-Zehnder interferometric setup is also shown.....	65
Figure 7-9 (a) The change of temperature inside the thermal chamber and (b) the corresponding frequency drifts of the OEO at 1550 nm, 1609 nm and 1612 nm.	66
Figure 7-10 Measured TCD of the 1090-m HC-PBGF delay-line at different operational wavelengths from 1530 nm to 1615 nm. The predicted TCD variation is also shown.	67
Figure 7-11 Allan deviation of the OEO at 1610 when the 1090-m HC-PBGF delay-line was stabilized at 26°C inside the thermal chamber while the other components of the OEO loop were shielded from ambient temperature variations (blue-line). Grey-line shows the previously shown minimum Allan deviation of the 860-m HC-PBGF delay-line incorporated OEO at 1550 nm.....	68
Figure 7-12 Phase noise spectra of the OEO with 1090-m HC-PBGF delay-line and 700 m SMF delay-line at 1550 nm (without laser frequency modulation).	69
Figure 7-13 Phase noise spectra of the OEO with 1090-m HC-PBGF delay-line and 700 m SMF delay-line at 1612 nm (without laser frequency modulation).	70
Figure 7-14 Phase noise spectrum with modulation harmonic peaks due to laser frequency modulation	71
Figure 7-15 Phase noise spectra of the OEO with 1090-m HC-PBGF delay-line and 700-m SMF delay-line at 1550 nm (with laser frequency modulation).	71

Table of Figures

Figure 7-16 Phase noise spectra of the OEO with 1090-m HC-PBGF delay-line and 700-m SMF delay-line at 1612 nm (with laser frequency modulation).....	72
Figure 8-1 Schematic of the PM-depolarizer. PBS: Polarization beam splitter, OS: Offset splice. Losses of P and P' are intentionally increased at OSs during splicing to match the losses of Q and Q' respectively. ..	76
Figure 8-2 Schematic of the SMF-depolarizer. PBS: Polarization beam splitter, FRM: Faraday rotator mirror, OS: Offset splice. Losses of P and P' are intentionally increased at OSs during splicing to match the losses of Q and Q' respectively. ..	77
Figure 8-3 The range of DOP variation of the output signal that can be expected for fluctuations of the centre frequency of the input signals (f_0) and/or the induced time delays (τ_1 , τ_2). The DOP variation corresponding to an input-SOP of 45° is shown.	81
Figure 8-4 The variation of minimum required delay-line lengths in Stage 1 (L_1) of the proposed depolarizers (when L_2 is set to $2L_1$) to reach output signal DOP level below 5% when FWHM linewidth of the input signal is varied.	82
Figure 8-5 The variation of output signal DOP as a function of the coupling ratio of the coupler for different input-SOPs. To maintain output signal DOP below 5% for all input-SOPs, the coupling ratio must be between 47.5:52.5 and 47.5:52.5.....	83
Figure 8-6 The variation of output signal DOP as a function of the differential loss between fibre paths in Stage 1 when the coupling ratio of the coupler is 47.5:52.5. DOP variations for different input-SOPs are shown.....	84
Figure 8-7 The variation of output signal DOP as a function of the differential loss between fibre paths in Stage 2 when the coupling ratio of the coupler is 47.5:52.5. DOP variations for different input-SOPs are shown. The red-line also shows the DOP variation for any input-SOP when the coupling ratio of the coupler is 50:50.85	85
Figure 8-8 The variation of output signal PDL as a function of the differential loss between fibre paths in Stage 1. PDL variation does not depend on coupling ratio.	86
Figure 8-9 The variation of output signal PDL as a function the differential loss between fibre paths in Stage 2 when the coupling ratio is 50:50 and when the coupling ratio is 47.5:52.5.....	87
Figure 9-1 Experimentally measured coupling ratio variation of a PM coupler when the operational wavelength is varied. With this coupler, the operational wavelength	

range must be with is 1546 nm and 1561 nm to maintain output signal DOP below 5%.	89
Figure 9-2 Schematic of SMF-depolarizer with all the splice points shown by terminating the paths. PBS: Polarization Beam Splitter, FRM: Faraday Rotator Mirror, OS: offset splice.	90
Figure 9-3 The FWHM linewidth variation of the lasers when the bias current is varied. LD ₁ and LD ₂ operates at 1547 nm and LD ₃ operates at 1555 nm.	92
Figure 9-4 Schematic of the self-heterodyne linewidth measurement scheme. DL: Delay-line, AOM: Acousto-optic modulator, PC: Polarization controller, Att.: Optical attenuator, PD: Photodiode, ESA: Electrical spectrum analyser.	92
Figure 9-5 Schematic of the DOP measurement setup with polarization analyser (default setup). PC: Polarization controller.	93
Figure 9-6 Schematic of the manual DOP measurement setup used when the acquisition time of the polarization analyser was not sufficient (secondary setup). PC: Polarization controller, PD: Photodiode	94
Figure 9-7 Experimentally measured output signal DOP variation of the PM-depolarizer with 20 and 40 m PM delay-lines at 1555 nm. Simulated DOP variation is also shown.	95
Figure 9-8 Experimentally measured output signal DOP variation of the SMF-depolarizer with 10 and 20 m PM delay-lines at 1547 nm. Simulated DOP variation is also shown.	96
Figure 9-9 Experimentally measured output signal DOP variation of the SMF-depolarizer at 1547 nm with 200 and 400 m PM delay-lines. Simulated DOP variation is also shown.	97

Research Thesis: Declaration of Authorship

Print name:	UDARA SANDAMAL MUTUGALA
-------------	-------------------------

Title of thesis:	Optoelectronic Oscillators with Hollow-core Fibres
------------------	--

I declare that this thesis and the work presented in it are my own and has been generated by me as the result of my own original research.

I confirm that:

1. This work was done wholly or mainly while in candidature for a research degree at this University;
2. Where any part of this thesis has previously been submitted for a degree or any other qualification at this University or any other institution, this has been clearly stated;
3. Where I have consulted the published work of others, this is always clearly attributed;
4. Where I have quoted from the work of others, the source is always given. With the exception of such quotations, this thesis is entirely my own work;
5. I have acknowledged all main sources of help;
6. Where the thesis is based on work done by myself jointly with others, I have made clear exactly what was done by others and what I have contributed myself;
7. Parts of this work have been published as: [see *List of Publications*]

Signature:		Date:	18-06-2019
------------	--	-------	------------

List of Publications

Journal Papers

1. M. Merklein, B. Stiller, I. V. Kabakova, U. S. Mutugala, K. Vu, S. J. Madden, B. J. Eggleton, and R. Slavík, "Widely tunable, low phase noise microwave source based on a photonic chip," *Optics Letters*, vol. 41, no. 20, pp. 4633–4636, 2016.
2. U. S. Mutugala, J. Kim, T. D. Bradley, N. V. Wheeler, S. R. Sandoghchi, J. R. Hayes, E. Numkam Fokoua, F. Poletti, M. N. Petrovich, D. J. Richardson, and R. Slavík, "Optoelectronic oscillator incorporating hollow-core photonic bandgap fiber," *Optics Letters*, vol. 42, no. 13, pp. 2647–2650, 2017.
3. U. S. Mutugala, I. P. Giles, M. Ding, D. J. Richardson, and R. Slavík, "All-fiber passive alignment-free depolarizers capable of depolarizing narrow linewidth signals," *Journal of Lightwave Technology*, vol. 37, no. 3, pp. 704–714, 2018.
4. U. S. Mutugala, E. R. Numkam Fokoua, Y. Chen, T. Bradley, S. R. Sandoghchi, G. T. Jasion, R. Curtis, M. N. Petrovich, F. Poletti, D. J. Richardson, and R. Slavík, "Hollow-core fibres for temperature-insensitive fibre optics and its demonstration in an optoelectronic oscillator," *Scientific Reports*, vol. 8, p. 18015, 2018.

Conference Proceedings

1. M. Merklein, B. Stiller, I. Kabakova, U. Mutugala, K. Vu, S. Madden, B. Eggleton, and R. Slavík, "Opto-electronic oscillator employing photonic-chip based stimulated Brillouin scattering," in *Photonics and Fiber Technology 2016 (ACOFT, BGPP, NP)*, Sydney, Australia, 2016, p. NW3A.6.
2. M. Merklein, B. Stiller, I. Kabakova, U. Mutugala, K. Vu, S. Madden, B. J. Eggleton, and R. Slavík, "Photonic-chip based widely tunable microwave source using a Brillouin opto-electronic oscillator," in *Frontiers in Optics 2016*, Rochester, New York, USA, 2016, p. FTh4G.3.
3. U. S. Mutugala, J. Kim, T. D. Bradley, N. V. Wheeler, S. R. Sandoghchi, J. Hayes, E. Numkam-Fokoua, F. Poletti, M. N. Petrovich, D. J. Richardson and R. Slavík, "Optoelectronic oscillator with low temperature induced frequency drift," in *2016 IEEE Photonics Conference (IPC)*, Waikoloa, Hawaii, USA, 2017, pp. 270–271.

Acknowledgements

First of all, I would like to thank the Optoelectronics Research Centre for funding my studentship and giving me the opportunity to pursue a PhD degree. I would also like to thank Phoenix Photonics, UK and its CEO, Dr. Ian Giles for partly funding my studentship.

I am ever so grateful to my main-supervisor, Dr. Radan Slavík for his supervision and guidance throughout this journey. His patience allowed me to grow and his motivation always pushed me forward. I thank him for allowing me to work alongside him and sharing his knowledge and expertise with me. It was a privilege and I couldn't have thought of a better mentor than Radan.

My heartiest gratitude goes to my co-supervisor, Prof. David Richardson for the overall supervision and guidance he gave and for the valuable feedback provided whenever needed. He was a great strength to me during the time of the PhD.

I wish to express my heartfelt gratitude to Dr. Joonyoung Kim for his tremendous support and for sharing his knowledge which helped me immensely to understand various concepts. I thank him for always having time for me whenever I needed to talk and being one of the nicest people I know.

I would like to thank all my friends at the Optoelectronics Research Centre for all the good times that we had. I would like to especially thank Dr. Kyle Bottrill for being such a great friend to me and I cherish all the interesting and lengthy discussions we had on many topics over the years. Furthermore I thank Meng Ding for being a great friend and a colleague who never hesitated to help me.

I thank all the members of the Optoelectronics Research Centre including academic, research, technical and administrative staff who helped me in numerous ways.

I wish to thank my dearest parents for always being there for me and believing in me.

Last but not least, I would like to thank my beloved wife Shehara for the love and encouragement provided every step of the way.

Definitions and Abbreviations

AOM	Acousto-optic modulator
COEO	Coupled optoelectronic oscillator
cw	continuous wave
DFB	Distributed-feedback
DOP	Degree of polarization
EAM	Electro-absorption modulator
EDF	Erbium-doped fibre amplifier
EDFA	Erbium-doped fibre amplifier
FP	Fabry-Perot
FSR	Free spectral range
FWHM	Full width at half maximum
GPS	Global positioning system
HC-PBGF	Hollow-core photonic bandgap fibre
IF	Intermediate frequency
LO	Local oscillator
MZM	Mach-Zehnder intensity modulator
OEO	Optoelectronic oscillator
PBC	Polarization beam combiner
PBS	Polarization beam splitter
PDL	Polarization dependent loss
PM	Polarization maintaining
RBW	Resolution bandwidth
RF	Radio frequency
RIA	Radiation induced attenuation
SAW	Surface acoustic wave
SBS	Stimulated Brillouin scattering
SEM	Scanning electron microscope
SMF	Single mode fibre

Definitions and Abbreviations

SOA	Semiconductor optical amplifier
SOP	State of polarization
SSB	Single sideband
SUT	Signal under test
TCD	Thermal coefficient of delay
WGM	Whispering galley mode

Chapter 1 Introduction

Spectrally pure microwave signals with long-term stability are a fundamental component in many scientific and technological applications ranging from metrology to communications and from radar to radio astronomy [1], [2]. In conventional methods of microwave signal generation, mechanical energy storage elements such as quartz crystal resonators [3], microwave energy storage elements such as dielectric resonators [4], and acoustic energy storage elements such as surface acoustic wave (SAW) devices [5] are used [6]–[9]. However when generating microwave signals, lower frequency signals generated using quartz crystals and SAW devices are frequency multiplied [10]. This process also increases the noise associated with the low frequency signal by factor of $20\log N$ (where N is the multiplication factor) [10], degrading the spectral purity. On the other hand, high quality factor (q-factor) microwave energy storage elements capable of directly generating microwave signals can be susceptible to environmental perturbations and may need cryogenic cooling for optimum performance, imposing limitations on their usability [10].

In contrast to the above mentioned conventional microwave oscillators driven purely by electrical energy, optoelectronic oscillators (OEOs) generate microwave signals using an optical energy source and an optical energy storage element based, hybrid feedback loop which is part-optical and part-electrical [8]. With low-loss high q-factor optical energy storage elements, OEOs are capable of generating microwave signals with high-spectral purity [9]. Furthermore they can directly generate microwave signals >10 GHz without frequency multiplication. Yao and Maleki, the inventors of the OEO showed [7] that OEO phase noise (by which the spectral purity is characterized) is independent of the oscillating frequency and that phase noise can be decreased by increasing the delay induced by the optical energy storage element. Due to these desirable features, OEOs quickly caught the attention of the scientific community which further improved the OEO technology by giving rise to OEOs with various optical energy storage elements and various OEO architectures [10], and to date, OEOs are a heavily researched topic.

The inventors of the OEO, used optical fibre delay-lines as the optical energy storage element in the very first OEOs that were built [7]. Even though other optical energy storage elements such as fibre ring resonators [11] and microresonators [12] were also incorporated in OEOs later, optical fibres can be considered as the most widely used optical energy storage elements in OEOs since they can be integrated into OEO setups with minimum effort and more importantly, they are readily available in kilometre-scale lengths so that long lengths of optical fibres can be incorporated into OEOs to improve the spectral purity of the generated signals.

Chapter 1

Even though, the spectral purity of an OEO can be improved by increasing the length of the optical fibre delay-line, the delay induced by an optical fibre is susceptible to the temperature variations of the surrounding [13], [14]. Hence, when an optical fibre is incorporated in an OEO, the loop delay of the OEO and as a result, the frequency of the OEO-generated signal becomes susceptible to temperature variations of the surrounding, leading to frequency variations.

Ultimately, the long-term stability of the OEO gets degraded by these frequency variations.

In standard single-mode fibres (SMFs), 95% of temperature induced delay change is caused by the temperature induced group index (n_g) change in the guided mode while rest (5%) is caused by temperature induced fibre length changes [13], [14]. This suggests that by using an optical fibre with a core material that has a less temperature sensitive refractive index, a reduction in temperature induced delay changes in the fibre and hence an improvement in the long-term stability of the OEO can be expected.

A class of microstructured optical fibres known as hollow core photonic bandgap fibres (HC-PBGFs) can be identified as a possible candidate for such an application. These fibres consist of an air-filled hollow core which is surrounded by a micro-structured cladding region. In HC-PBGFs, more than 99% [15] of light can be guided through the air-filled hollow core. Since air has a negligible thermo-optic coefficient at constant volume (e.g., in a HC-PBGF spliced from both ends) [14], [16], the temperature induced delay changes in HC-PBGFs due to temperature induced group index change are greatly suppressed. In these fibres, the remaining temperature induced fibre elongations become the main cause of temperature induced delay changes [14].

Moreover it has been shown that the remaining temperature sensitivity of HC-PBGFs (due to fibre elongations) can be further reduced by a temperature induced group velocity change with opposite effect so that light propagates faster through the elongated fibre [16]. This property is dependent on the wavelength of light propagating through the HC-PBGF and it has been experimentally shown that zero and even negative temperature sensitivity characteristics can be achieved in HC-PBGF by operating at the correct wavelength [16].

The incorporation of HC-PBGFs in OEOs for improved temperature stability has been discussed in the literature before [17]–[19]. However the main limitation of these works is that only tens of metres of HC-PBGFs have been used in the performed experiments. In order to generate low phase noise signals using OEOs, long optical fibre delay-lines (more than hundreds of metres in general) have to be used and to the best of my knowledge, OEOs with hundreds of metres long HC-PBGF delay-lines have not been demonstrated.

My work presented in this thesis is focused on investigating the temperature stability improvement that can be obtained in OEOs by incorporating long-length HC-PBGFs (hundreds of metres long) as the optical energy storage elements. First, the temperature stability improvement that can be obtained in the OEO when limited by the temperature induced elongations of the HC-PBGF delay-line is investigated. Next, the temperature stability improvement that can be obtained by changing the operational wavelength of optical energy source of the OEO (by reaching zero and negative temperature sensitivity characteristics of the HC-PBGF) is investigated. The spectral purity of the HC-PBGF delay-line incorporated OEOs is also investigated by characterizing their phase noise.

Furthermore due to unintentional core asymmetries, HC-PBGF may inherit birefringent characteristics which can lead to polarization mode splitting [20]. In addition, due to coupling of light into spurious guided modes, HC-PBGFs may also have a polarization dependent loss (PDL) [21], [22]. Polarization mode coupling has also been observed in HC-PBGFs [21]. Due to these reasons a polarization dependent behaviour in HC-PBGF incorporated OEOs can be anticipated. In order to minimize the possible polarization dependent behaviour, development of a depolarizer capable of depolarizing light from optical energy sources typically-used in OEOs (e.g., semiconductor distributed-feedback (DFB) lasers) is also investigated as a part of this work. Rather than using an active and bulky polarization scrambler, the development of a compact, passive all-fibre depolarizer that can be used as an integral part of the OEO as well as a standalone device that can be used in other possible applications is investigated.

1.1 Thesis Outline

In order to clearly separate the work I did from the state-of-the-art, all the chapters that discuss background and literature are lined-up at the beginning of the thesis, before presenting the experimental work and results. Specifically, the experimental work and the results obtained by incorporating HC-PBGFs in OEOs are presented in Chapters 6 and 7. The background and literature related to this work is presented in Chapters 2, 3 and 4. The theoretical and experimental work done on passive all-fibre depolarizers and the outcomes of the work are presented in chapters 8 and 9. The related background and literature is given in chapter 5.

- **Chapter 2 – Optoelectronic Oscillator: Background** The functionality of OEOs and different OEO architectures with multi-loop structures, different optical energy storage elements, different modulators, etc. are discussed in this chapter. Applications of OEOs are also discussed here.

Chapter 1

- **Chapter 3 – Optoelectronic Oscillator: Stability Characterization** The short-term and long-term stability of signals, schemes that measure signal stability and the measurement schemes I used during experiments are discussed in this chapter. The temperature sensitivity of optical fibre delay-lines are also discussed here.
- **Chapter 4 – Hollow-core Photonic Bandgap Fibres** Microstructured optical fibres in terms of different guiding mechanisms are discussed in the first part of this chapter. Fabrication, properties, and applications of HC-PBGFs are discussed next. The temperature sensitivity of HC-PBGFs is discussed in detail in this chapter.
- **Chapter 5 – Passive Fibre-optic Depolarizers** Various types of depolarizer are discussed in terms of their domain of operation in the first part of this chapter. The second part of this chapter is dedicated to discuss passive fibre-optic depolarizers in particular.
- **Chapter 6 – Incorporating Hollow-core Photonic Bandgap Fibre into Optoelectronic Oscillator** The temperature stability improvement I obtained by incorporating an 860 m long HC-PBGF delay-line in an OEO, when the temperature stability is limited by the length changes of the HC-PBGF is discussed in this chapter.
- **Chapter 7 – Exploiting Zero-TCD Characteristics of Hollow-core Photonic Bandgap Fibres to Improve the Thermal Stability of Optoelectronic Oscillators** In this chapter I investigate the zero temperature sensitivity characteristics in HC-PBGFs by counteracting the effect of temperature induced fibre elongations by changing the operational wavelength of the light propagating through a 1090 m long HC-PBGF used as a delay-line in an OEO. .
- **Chapter – 8 Passive Fibre-optic Depolarizers for Narrow-linewidth Signal Depolarization: Configurations, Theoretical Analysis and Simulations** I propose two passive fibre-optic depolarizer configurations capable of depolarizing narrow-linewidth signals in few megahertz-scale. I theoretically analyse and simulate the performance of the proposed depolarizers in this chapter.
- **Chapter – 9 Passive Fibre-optic Depolarizers for Narrow-linewidth Signal Depolarization: Fabrication and Characterization** I discuss the fabrication of the proposed depolarizers with optimum performance and characterization of the fabricated depolarizers in this chapter.
- **Chapter 10 – Conclusions** The main findings of my work presented in this thesis and potential future work is discussed in this chapter.

Chapter 2 Optoelectronic Oscillator: Background

The first part of this chapter explains the generic architecture and the operation of the OEO. Next, various modified OEO configurations that have been introduced over the years with different filtering mechanisms, multi-loop architectures, different types of optical modulators and optical energy storage elements, etc. are discussed. In the last part of this chapter, applications of OEOs are discussed.

2.1 The Generic Architecture and Operation of an OEO

The very first OEOs demonstrated by Yao and Maleki [7], [23], [24] had an optical fibre delay-line based single feedback loop structure. OEOs of this architecture are commonly known as single-loop OEOs. The schematic diagram of a generic single-loop OEO is shown in Figure 2-1 and its main components are: an optical energy source (e.g., a laser), an optical modulator (e.g. a Mach-Zehnder intensity modulator, MZM), an optical fibre delay-line (as the optical energy storage element), a photodetector, an RF (radio frequency) amplifier, and an RF band-pass filter.

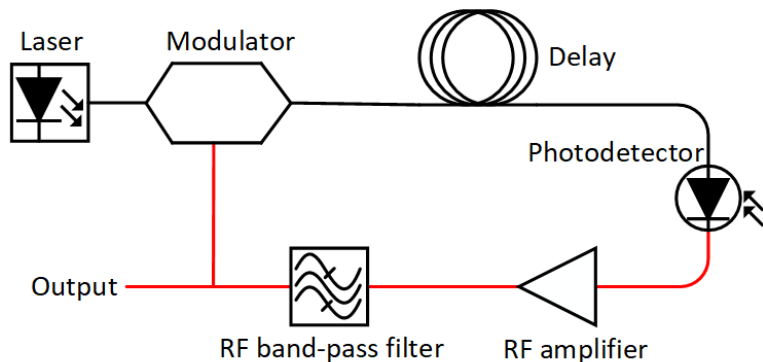


Figure 2-1 Simplified schematic of a generic single-loop OEO.

Optical paths are shown in black and electrical paths are shown in red.

In the setup, the light generated by the laser is launched into the optical modulator. The optical signal exiting the modulator is propagated through the optical fibre delay-line and detected by the photodetector. The electrical output signal of the photodetector is amplified by the RF amplifier and then filtered by the RF band-pass filter. The filtered signal is split into two; one part is fed back into the modulator as the modulation signal, closing the OEO loop and the other part serves as the OEO output signal. Due to this part-optical and part-electrical feedback loop structure, optical energy storage elements such as long lengths of optical fibres up to tens of kilometres (and other energy storage elements such as ring resonators, microresonators, etc. which will be discussed later) can be used in the OEO loop to generate microwave signals with high spectral

purity. Yao and Maleki showed that the phase noise of their single-loop OEOs decreases quadratically with the loop delay [7], [24]. Furthermore, phase noise levels as low as -163 dBc/Hz at 6 kHz offset frequency have been reported in a 10 GHz single-loop OEO with a 16 km long optical fibre delay-line [25].

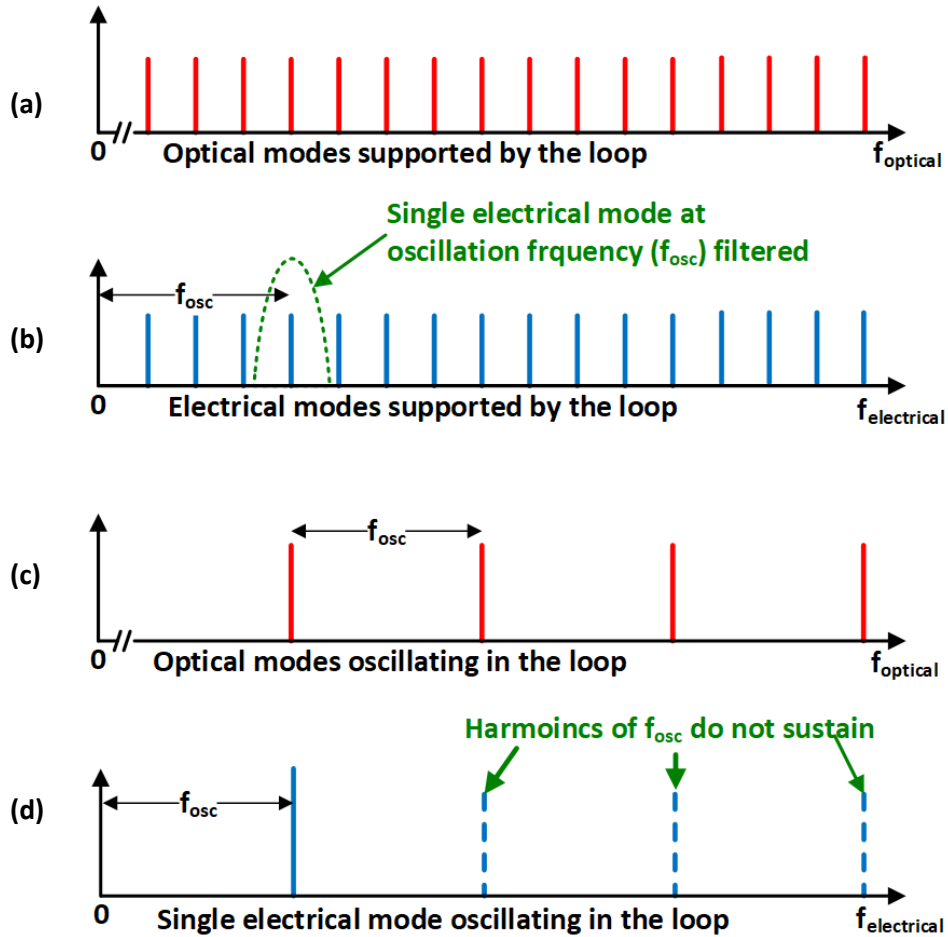


Figure 2-2 Obtaining single-mode oscillation in an OEO.

The oscillation in an OEO starts from noise and when the overall gain in the loop is higher than the losses, the circulating waves that add up in phase sustain in the loop, leading to multi-mode oscillation [7], [9], [10]. As shown in Figure 2-2a, multiple modes exist in the optical signal that propagates through the optical part of the OEO loop. The photodiode detects the beating between these optical modes and generates a multi-mode electrical signal (see Figure 2-2b) that propagates in the electrical part of the OEO loop. When this electrical signal is fed back into the modulator to modulate the optical signal, a multi-mode oscillation sustains in the OEO. The spacing between the oscillating modes is determined by the free spectral range (FSR) of the OEO loop [10], and FSR is determined by the delay induced by the OEO loop [9].

However when an RF band-pass filter is employed in the OEO loop, a single electrical mode at a desired microwave frequency (f_{osc}) can be selected to be fed back to the modulator while

suppressing the other modes (see Figure 2-2b) [9]. Now optical signal is modulated with the microwave frequency of the filtered mode and the spacing between the optical modes is equal to the filtered mode (as shown in Figure 2-2c). These optical modes beat on the photodetector to reproduce a strong electrical signal at the desired microwave frequency and thus sustaining a single-mode oscillation. It should be noted that the higher harmonics of f_{osc} produced by optical mode beating (shown in Figure 2-2d) are filtered out by the RF filter and hence not sustained [7].

The frequency of the generated microwave signal can be tuned using several methods. If the RF filter is tuneable, the centre-frequency of its pass-band can be changed to vary the OEO output signal [10]. If the RF filter is not tuneable, output signal frequency can be tuned within its pass-band by varying the OEO loop delay (e.g., by using a fibre stretcher [26] or variable optical delay-line), by changing the bias voltage of the modulator [26], or by varying the wavelength of the laser [10].

2.2 Obtaining Single-mode Oscillation without Narrow RF Band-Pass Filters

Even though the spectral purity of an OEO generated signal can be improved by increasing the OEO loop delay by employing longer optical fibres, increasing the loop delay decreases the FSR of the loop and in turn the OEO mode spacing [9]. For example if the OEO loop length is 2 km, the mode spacing becomes 100 kHz. Hence to maintain a single-mode oscillation, the pass-band of the RF filter used in the OEO must also be narrow enough to filter a single mode out of the closely packed modes. However high frequency (>10 GHz) RF band-pass filters with sufficiently narrow pass-bands can be difficult to obtain, costly, and they may also suffer excess insertion loss and limited tunability [27].

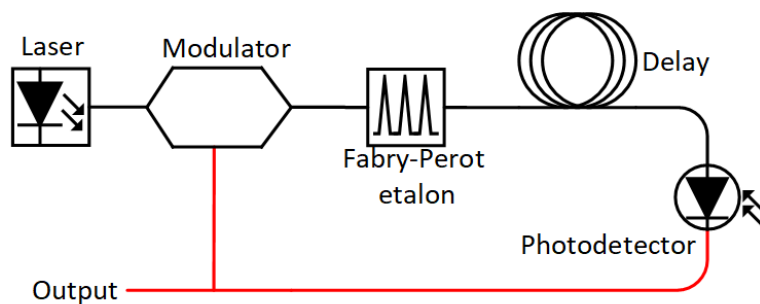


Figure 2-3 Simplified schematic of a single-loop OEO with a Fabry-Perot etalon.

Optical paths are shown in black and electrical paths are shown in red. Note: amplifying components are not shown.

Instead of strictly using RF filters, filtering can also be done in the optical domain to relax the narrow-bandwidth requirements of the RF filter. For example, as shown in Figure 2-3, a Fabry-Perot (FP) etalon can be used to filter optical OEO modes separated by the FSR of the FP etalon, allowing widely spaced optical modes to beat on the photodetector (note: FSR of the FP etalon is larger than the natural mode spacing of the OEO) [28]. Beating of widely spaced optical modes produces an electrical signal with widely spaced modes and one of the modes can be filtered for single-mode oscillation using a common RF band-pass filter. Single-mode oscillation is also possible without any electrical filtering, for example, a 10 GHz OEO signal can be obtained by using an FP etalon with a 10 GHz FSR to produce a single 10 GHz mode in the electrical domain [28].

Another technique of obtaining single-mode oscillation is to pump the OEO loop with a second laser to induce stimulated Brillouin scattering (SBS) [29], [30]. The SBS process which has a narrow gain bandwidth can be used to selectively amplify a single optical mode which can then be beaten with the optical frequency of primary laser (carrier frequency) of the OEO. The beating can be detected by a photodetector and fed back into the modulator for single-mode oscillation without the need of an RF filter [29]. The same concept has been implemented in ref. [30] with SBS filtering and amplification being done in chip-scale using a chalcogenide waveguide. Furthermore, by changing the optical frequency of the primary laser of the OEO relative to the SBS pump laser, a tunability of up to 40 GHz has been demonstrated in this OEO with <100 dBc/Hz phase noise levels at 100 kHz offset frequency.

2.3 Multi-loop OEO Architectures

Multi-loop architectures are another approach of obtaining low phase noise, single-mode oscillation in OEOs without the need of an RF band-pass filter with a very narrow bandwidth. Over the years, various OEO configurations that can be considered as multi-loop OEOs have been demonstrated. A simplified schematic diagram of a dual-loop OEO [27] is shown in Figure 2-4. In this setup, the optical signal at the output of the modulator is split and propagated through two optical fibre delay-lines with dissimilar lengths. Optical signals at the output of the delay-lines are detected by two photodetectors separately. The signals from the photodetectors are combined in the electrical domain. In this OEO, the mode spacing of the electrical signal is determined by the shorter loop and the spectral purity is determined by the longer loop [27]. This allows a common RF band-pass filter to be utilized for the selection of a single mode. Phase noise level of -140 dBc/Hz at 10 kHz offset frequency has been obtained in a 10 GHz OEO of this type using a 2 km long optical fibre in the longer loop (and few meters in the shorter loop) [27]. Phase noise level of -128 dBc/Hz at 10 kHz offset frequency has been reported in similar triple-loop OEO configuration

with 4.4, 3 and 1.2 km long optical fibres delay-lines [31]. The microwave signal generated by this particular OEO can be tuned between 6 and 12 GHz using the tuneable RF band-pass filter. Furthermore it should be noted that even though single mode oscillation can be obtained using an RF band-pass filter, spurious modes with a mode spacing equivalent to the FSR of the OEO loop can still exist within the pass-band of the RF filter and these spurious modes can also be suppressed by implementing multi-loops in the OEO [31].

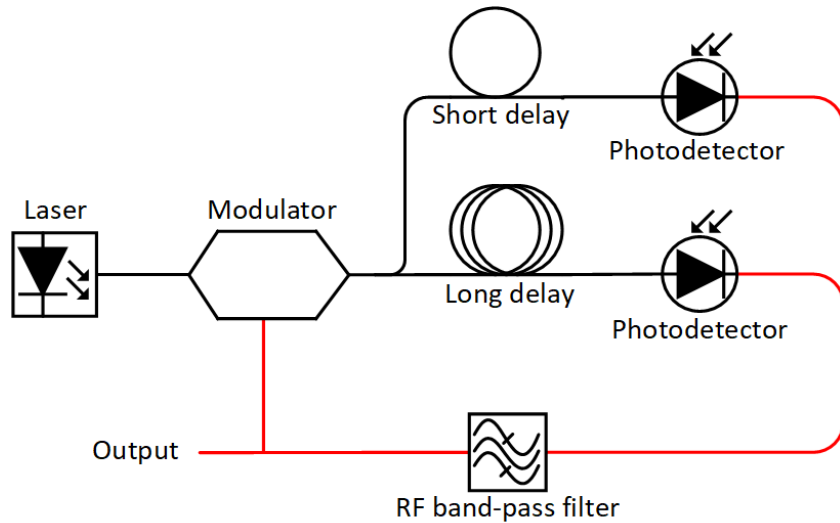


Figure 2-4 Simplified schematic of a dual-loop OEO.

Optical paths are shown in black and electrical paths are shown in red. Note: amplifying components are not shown.

In a slightly different multi-loop configuration [32], the signals from two loops have been combined in the optical domain. In this technique, a polarization beam splitter and a polarization beam combiner have been used to split the optical signal into the two delay-lines and to re-combine the optical signals exiting two delay-lines respectively. The ability to detect optical signals using a single photodetector is the advantage of this setup and a phase noise level of -109 dBc/Hz at 10 kHz offset frequency has been reported in the 12 GHz OEO generated microwave signal.

Two OEOs with dissimilar lengths of optical fibre delay-lines operating in an injection-locking setup have been demonstrated [33] and this can also be considered as a multi-loop OEO configuration. In this setup, the OEO with 6 km optical fibre delay-line acts as the master and oscillates in multi-mode with closely packed modes of high spectral purity. The slave OEO with ~50 m optical fibre length has widely spaced modes and oscillates in single-mode. The multi-mode electrical signal from the master OEO is injected into the slave OEO and the single oscillating mode of the slave OEO is locked with one of the modes of the master OEO. Now the slave oscillates in single mode with the spectral purity of the master OEO. A simplified schematic

diagram of this configuration is shown in Figure 2-5. A 10 GHz microwave signal with a phase noise level of -150 dBc/Hz at 10 kHz offset has been generated using this configuration [33].

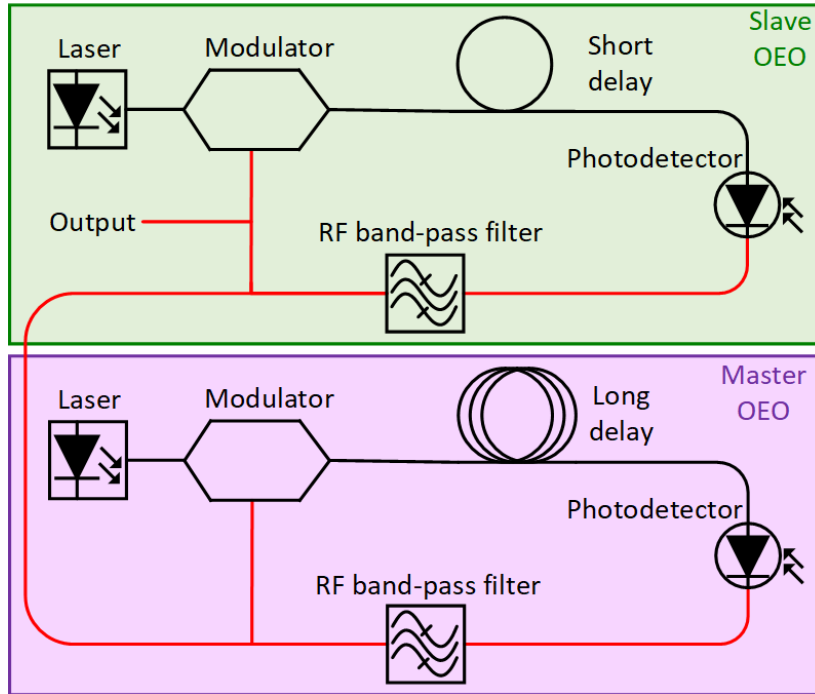


Figure 2-5 Simplified schematic of an injection locked dual OEO.

Optical paths are shown in black and electrical paths are shown in red. Note: amplifying components are not shown.

The coupled-OEO (COEO) [34]–[36], in which one loop is fully optical, is another OEO configuration that can be considered as a multi-loop setup. A simplified schematic of the COEO in ref. [34] is shown in Figure 2-6. In this COEO, a ring laser with a semiconductor optical amplifier (SOA) gain medium and a 23 MHz mode spacing (corresponding to a loop length of 8.6 m) operates as the optical energy source. The optical signal of the ring laser is coupled out to a second loop (the OEO loop) to be propagated through a 100 m long optical fibre delay-line and detected by a photodetector. The photodetector output signal is filtered, amplified, and fed back into the RF modulation port of the SOA. Even though the natural mode spacing of the OEO loop is much narrower, by using a common RF band-pass filter with a bandwidth less than the laser mode spacing, a single mode can be selected for oscillation. This process mode locks the laser and the laser mode spacing is determined by the oscillation frequency of the OEO [34]. In references [35] and [36], Erbium doped fibre amplifiers (EDFAs) have been used as the optical gain medium and optical fibre delay-lines have been incorporated into the optical loop (laser loop). Phase noise levels of -140 dBc/Hz at 10 kHz offset frequency in the 9.2 GHz COEO in ref. [35] and -150 dBc/Hz at 10-100 kHz offset frequency range in the 9.4 GHz COEO in ref. [36] have been reported.

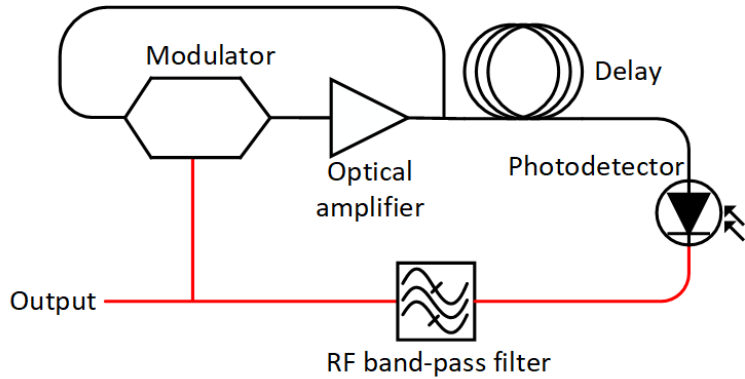


Figure 2-6 Simplified schematic of a coupled-OEO.

Optical paths are shown in black and electrical paths are shown in red. Note: electrical amplifying components are not shown.

2.4 Types of Modulators in OEOs

MZM type intensity modulators have been used in the very first OEOs [7], [23] demonstrated by Yao and Maleki and also in the 10 GHz multi-loop OEO in which a phase noise level of -140 dBc/Hz at 10 kHz offset frequency was obtained [27]. Electro-absorption modulators (EAMs) are another type of intensity modulators that have been used in OEOs [37], [38] and a phase noise level of -143 dBc/Hz at 10 kHz offset frequency has been reported in the 10 GHz EAM based OEO in ref. [38]. When it comes to the optical modulators used in OEOs, it can be seen that intensity modulators are a popular choice mainly because the beating between optical modes generated by intensity modulation can be detected directly by the photodetectors.

Even though photodetectors are not capable of directly detecting the beat signal of a phase modulated signal, they can be used in OEOs when optical modes are selectively amplified to be beaten with the carrier frequency; for example, in SBS based OEOs [29], [30]. Phase modulator based OEOs can also be realized by asymmetrically filtering a section of the phase modulated signal using an optical band-pass filter [39]. The advantage of phase modulators is that they do not require DC bias control [1].

Polarization modulators have reportedly been used in OEOs as well [40], [41]. In these OEOs, polarization modulation is converted into an intensity modulation by propagating the optical signal through polarization sensitive devices such as polarizers and polarization beam splitters (PBSs). Some advantages of polarization modulators are high-speed modulation (>40 GHz) and low insertion loss [1]. The reported phase noise level of polarization modulator based tuneable OEO (5.8 to 11.8 GHz) in ref. [41] was better than -104 dBc/Hz at 10 kHz offset frequency.

Rather than using separate modulators, the optical energy source of the OEO can be also be directly modulated. One example is the COEO in ref. [34] in which the SOA is directly modulated by feeding back the electrical signal. In another OEO configuration [42], a slave laser is injection locked with a master laser to amplify an optical side band. The beating between the carrier frequency of the slave laser and the amplified sideband is detected by a photodetector after propagating through an optical fibre. The detected electrical signal is fed back to directly modulate the slave laser after amplifying and filtering. Phase noise level of this 20 GHz OEO was reported to be \sim 120 dBc/Hz at 10 kHz offset frequency.

2.5 Optical Energy Storage Elements in OEOs Other Than Optical Fibres

Since optical fibres are readily available in long lengths and can be easily integrated into optical systems, they can be considered as the popular choice of optical energy storage element in OEO setups. However there are other types of optical energy storage elements that can be used in OEOs. One example is the high q-factor micro-resonators known as whispering gallery mode (WGM) resonators. WGMs can be spherical [43], disk [44], toroidal [45], etc. in shape. These can be used in OEOs not only as the energy storage element, but also as the filter and modulator [12], [46]. This makes miniaturization of OEOs more feasible. A simplified schematic of a WGM resonator based OEO is shown in Figure 2-7. A phase noise level of <100 dBc/Hz at 10 kHz offset frequency has been reported in a 9.8 GHz WGM resonator based OEO in ref. [46].

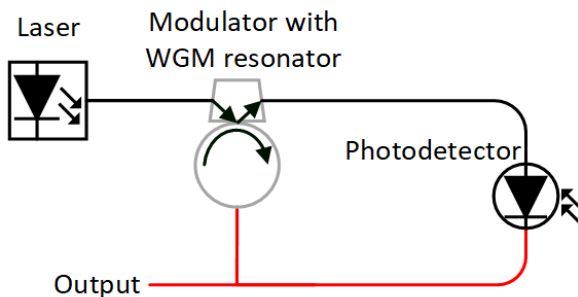


Figure 2-7 Simplified schematic of a Whispering gallery mode (WGM) resonator based OEO. Optical paths are shown in black and electrical paths are shown in red.
Note: amplifying components are not shown.

The use of fibre ring resonators in OEOs as the energy storage element has also been demonstrated. A ring resonator fabricated with a short length of optical fibre (tens of metres) is capable of providing a q-factor equivalent to that provided by a much longer optical fibre delay-line (thousands of metres) [11]. However since the FSR of the ring resonator is determined by the physical length of the fibre ring, the mode spacing of a tens of metres long fibre ring resonator based OEO can be several megahertz [11] so that single-mode oscillation can be achieved using a

common RF band-pass filter. A phase noise level of -128 dBc/Hz at 10 kHz offset frequency has been reported in a 10 GHz OEO, with a 100 m fibre ring resonator [11].

2.6 Applications of OEOs

Various OEO related applications have been proposed and demonstrated [1], [47]. Since OEOs can be injection-locked with external signals, they can be used for reference signal distribution and clock recovery applications. In reference signal distribution, the OEO is injection locked with an external reference signal to be amplified and re-distributed optically and electrically [47]. In clock recovery applications, the OEO is first tuned to a frequency close to the nominal frequency of the clock of the incoming signal. Then, when the incoming signal is injected into the OEO, it gets locked to the clock frequency and the recovered clock synchronized with the incoming signal can be obtained in both electrical and optical domains [47]–[50]. Furthermore since OEOs provide stable optical RF signals, they can be used for signal up/down conversion applications [47]; for example, in radio over fibre links [51], [52].

Injection locking of OEOs can also be used for frequency multiplication applications. This is done by injecting a subharmonic electrical signal of the OEO's nominal frequency into the OEO loop or modulating the optical energy source of the OEO by a subharmonic of the OEO's nominal frequency, and this process is known as subharmonic injection locking [47], [53]. In addition, it has been demonstrated that OEOs can be used for selective amplification of low power signals. In this application, the OEO is oscillated intentionally in multi-mode. The loop gain is kept just below the threshold so that when a low power microwave signal is injected into the OEO loop, a single-mode oscillation can be detected [1], [54], [55].

OEO configuration can also be used to generate frequency combs. Frequency combs can be generated by phase modulator based OEOs. In ref. [39], a section of the phase modulated signal is asymmetrically filtered, detected, and fed back into the phase modulator after heavily amplifying (up to 29 dBm in the report) to obtain a deeply modulated optical signal (i.e., a frequency comb). In a slightly different configuration, a phase modulator inside a FP resonator [56] has been used in the OEO to generate a frequency comb. In this configuration (see Figure 2-8), phase modulated optical side bands travel back and forth in the FP resonator giving rise to more side bands and hence generating a frequency comb. Similar to the previous case, a section of the comb is filtered, detected and fed back into the modulator. In both these comb generators [39], [56], comb mode spacing is determined by the RF band-pass filter in the loop. However in the latter case, the modulator should be driven with a frequency that is an integer multiple of the FSR of the FP resonator [56]. Furthermore, OEOs can be used to generate high-repetition rate optical pulses in

Chapter 2

time domain. In fact, comb generating OEOs can be used for this [47]. In addition EAM based OEOs have also been used to generate optical pulses with 10 GHz repetition rate [37].

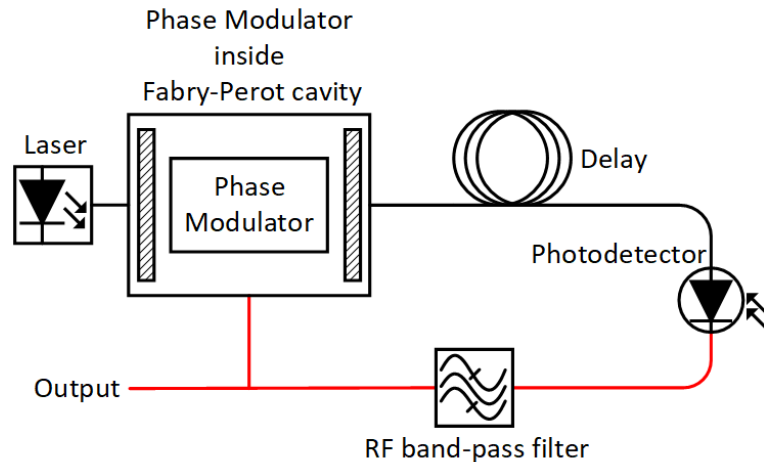


Figure 2-8 Simplified schematic of OEO based frequency comb generator [56].

Optical paths are shown in black and electrical paths are shown in red. Note: amplifying components are not shown.

Chapter 3 Optoelectronic Oscillator: Stability Characterization

Generation of spectrally pure microwave signals with low phase noise levels has always been the key strength of OEOs. Phase noise characterizes the short-term stability of a signal and various measurement schemes have been proposed to measure the phase noise of microwave signals. These schemes, together with the phase noise measurement scheme that was used in the experiments are discussed in the first part of this chapter.

In addition to the short term stability, the long-term stability is another key parameter of a signal that needs to be characterized and the measurement scheme used in the experiments to measure the long-term frequency stability of microwave signals is explained next. When it comes to the long-term stability of OEOs, it can be identified that the long-term stability of optical fibre delay-line based OEO can be degraded due to the temperature sensitivity of the optical fibre delay-line. The rest of the chapter is dedicated to discuss temperature sensitivity of optical fibres and the methods that have been implemented to improve the long-term stability of OEOs.

3.1 Short-term Stability

As mentioned, the short-term stability, or in other words, the spectral purity of a signal can be characterized by its phase noise. Phase noise is a frequency-domain representation (i.e., a spectrum) of phase fluctuations of the signal under test (SUT) [57]. Since it is a measure of short term stability, in general, phase noise is used to characterize phase fluctuations that occur in time scales <1 s (corresponding to phase fluctuations with >1 Hz frequency). Both heterodyne, and homodyne phase noise measurement schemes have been demonstrated.

3.1.1 Heterodyne Techniques

In heterodyne schemes, phase noise of the SUT is measured by comparing it with an external reference signal. The low-noise reference signal operating at the frequency of the SUT and the SUT are fed into the LO and RF ports of a mixer. The reference signal and SUT are kept at quadrature using a phase-locked loop. When the two signals have same frequency and are at quadrature, mixer functions as a phase detector, providing a base-band voltage fluctuation corresponding to the phase fluctuations between the two signals through the IF port [58], [59].

Chapter 3

However obtaining a high frequency (e.g., at 10 GHz), low-noise reference signal at the exact frequency of the SUT can be challenging. Another possible issue of this technique is the microwave leakage from reference source, forcing the oscillator under test to operate with a lower phase noise level leading to an inaccurate measurement [58]. The effect of microwave leakage is minimized in a modified heterodyne scheme where the reference signal and the SUT are at slightly different frequencies (e.g., at 10 and 9.95 GHz) [58]. The frequency difference can be chosen so that the leakage effect is minimized. In this scheme, the beating signal obtained by mixing the reference signal and the SUT (e.g., at 50 MHz) needs to be down-converted to base-band by mixing with a low-frequency, low-noise reference signal at the beat frequency before measuring phase noise. Even though this scheme gives some level of freedom when selecting the high-frequency reference signal, obtaining the reference signals (both high-frequency and low-frequency) can still be challenging [58].

3.1.2 Homodyne Techniques

In homodyne phase noise measurement schemes, phase noise of the SUT can be measured without the need of an external reference signal. In this technique, the SUT is split into two parts and one part is delayed with respect to the other by propagating through a delay-line. The two decorrelated components are then fed into a mixer with a 90° phase difference and the mixer converts phase fluctuations into a base-band voltage fluctuation. In this technique, phase noise measurement sensitivity at different offset frequencies depends on the induced delay; longer delays are required to measure the phase noise at offset frequencies closer to the carrier (this will be discussed further in the next section) [58]–[60].

This method was first demonstrated using electrical delay-lines [59]. The issue of using electrical cables as delay-lines is that their attenuation can be high at high frequencies [58]. For example, the attenuation of a LL142 type electrical coaxial cable can be ~ 0.8 dB/m at 10 GHz [61]. To induce a $1\ \mu\text{s}$ delay, about 250 m long cable is required (assuming 83% velocity of propagation [61] compared to velocity of light in vacuum). The attenuation of a 250 m electrical cable would be ~ 200 dB, which is too high to be used in practical applications.

However a modified homodyne phase noise measurement scheme has been demonstrated in which the delay is induced using optical fibres. This is known as the ‘photonic-delay’ phase noise measurement scheme [58]. Since optical fibres have much lower attenuation (~ 0.2 dB/km at 1550 nm), longer delays can be induced using this scheme (e.g., $1\ \mu\text{s}$ delay can be induced by a ~ 204 m optical fibre (SMF 28e+[62]) with just 0.04 dB attenuation) to accurately measure close-to-carrier phase noise levels.

Another optical fibre delay-line based phase noise measurement scheme known as the ‘dual photonic-delay cross-correlation’ technique has been demonstrated in ref. [60]. In this technique the SUT is split and sent through two separate photonic-delay phase noise measurement setups. The outputs of the two setups are fed into the two channels of a dual channel electrical spectrum analyser to measure the cross spectrum of the two channels. By averaging out the cross spectrum, the uncorrelated noise in the measurement setup can be suppressed to measure lower phase noise levels than the single channel photonic-delay technique [60].

Since close-to-carrier phase noise levels can be accurately measured by employing longer optical delay-lines which are readily available, I used the photonic-delay measurement scheme to measure phase noise characteristics in my experiments and details of this scheme is discussed in detail below. I did not implement the dual photonic-delay cross correlation scheme due to the unavailability of a dual channel electrical spectrum analyser. However the noise floor measurements showed that the sensitivity of the implemented photonic-delay scheme is sufficient to accurately measure the phase noise of the signals generated during the experiments.

3.1.3 Photonic-delay Phase Noise Measurement Scheme

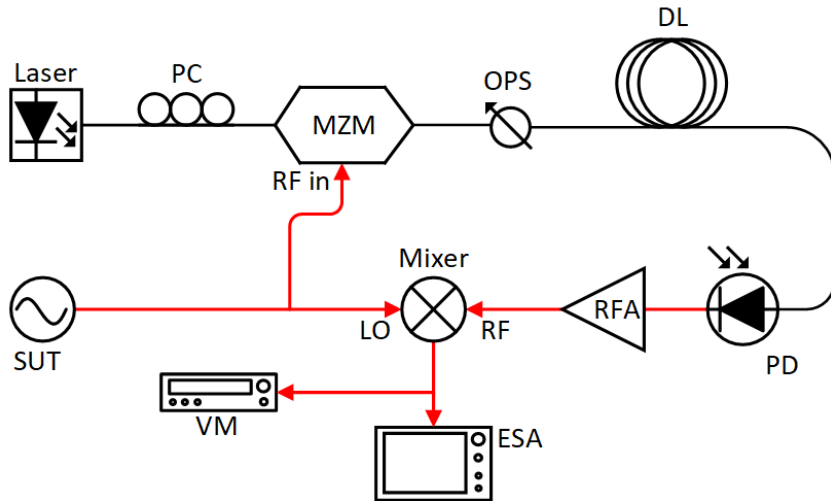


Figure 3-1 Schematic of the photonic-delay phase noise measurement scheme. PC: polarization controller, MZM: Mach-Zehnder modulator, OPS: Optical phase shifter, DL: Delay-line, PD: Photodiode, RFA: RF amplification, ESA: Electrical spectrum analyser, VM: Volt meter, SUT: Signal under test.

Optical paths are shown in black and electrical paths are shown in red.

Schematic diagram of the photonic-delay phase noise measurement scheme that I built is shown in Figure 3-1. The SUT is split into two parts by an electrical power splitter and the first part is fed into the LO port of a mixer. The second part is transferred into the optical domain using an MZM. Light from a continuous wave (cw) laser is fed into the optical input port of the MZM and the

MZM is biased to the quadrature point by applying a DC voltage through the bias port. The second part of the SUT is fed into the RF port of the MZM to modulate the laser light, transferring the signal into the optical domain. The modulated light is sent through an optical fibre delay-line to be delayed with respect to the first part and then detected by a photodiode. The photodiode transfers the optical signal back into the electrical domain and the electrical output signal of the photodiode is amplified and fed into the RF port of the mixer.

The mixer output is split into two and first part is fed into an electrical spectrum analyser to record base-band voltage fluctuations. The DC level of the mixer output needs to be maintained at 0 V in order to ensure that the signals arriving at the LO and RF ports of the mixer are at quadrature [59], [63], [64]. Hence the DC component of the mixer output is monitored by feeding the second part of the mixer output to a voltmeter and the optical phase shifter placed between the MZM and the optical fibre delay-line is adjusted as necessary to maintain the DC level at 0 V.

The relationship between the mixer output voltage (V_{out}) and the phase noise spectrum (S_ϕ) of the SUT in photonic-delay phase noise measurement scheme can be given by [60], [63],

$$V_{out}^2(f) = K_\phi^2 |H_\phi(jf)|^2 S_\phi, \quad 3-1$$

where K_ϕ is the mixer voltage gain coefficient. $|H_\phi(jf)|^2$ is the transfer function of the delay-line and can be written as [58], [60],

$$|H_\phi(jf)|^2 = 4 \sin^2(\pi f \tau), \quad 3-2$$

where f is the offset frequency and τ is the time delay induced by the delay-line. The standard measure of phase noise, the single sideband (SSB) phase noise $L(f)$ can be written as [59], [60],

$$L(f) = \frac{S_\phi}{2}, \quad 3-3$$

and $L(f)$ can be written in terms of V_{out} according to [60],

$$L(f) = \frac{V_{out}^2(f)}{2K_\phi^2 |H_\phi(jf)|^2}. \quad 3-4$$

3.1.3.1 Delay-line Transfer Function

The delay-line transfer function, $|H_\phi(jf)|^2$, plotted as a function of f for three different delay-line lengths (100 m, 1 km and 5 km corresponding to delays of around 0.5 μ s, 5 μ s and 25 μ s respectively) is shown in Figure 3-2. It can be seen that phase noise measurement sensitivity varies with the delay-line length. Furthermore, null sensitivity points (points with zero sensitivity)

occur when $f=N/\tau$, where N is an integer [58], [60]. For example, when the delay-line length is 5 km, the sensitivity maximizes around 10 kHz and the first null-sensitivity point occur at 40 kHz limiting the measurement range. The measurement range can be increased by using a shorter delay-line. For example, the first null point occurs at 400 kHz when the delay-line length is 1 km. However it can be seen that a shorter delay-line has lower sensitivity at lower offset frequencies compared to a longer delay-line. For instance, at 10 kHz offset frequency, the sensitivity of 1 km delay-line is more than two orders of magnitude higher than the sensitivity of 100 m delay-line. Hence the best strategy for obtaining higher accuracy measurements using this scheme is to measure phase noise with different delay-line lengths and then stich them together.

Furthermore, it can be clearly seen that due to this transfer function characteristics, the electrical delay-line based homodyne phase noise measurement schemes [59] (due to the higher attenuation of the longer cables), are not suitable to accurately measure phase noise at lower offset frequencies.

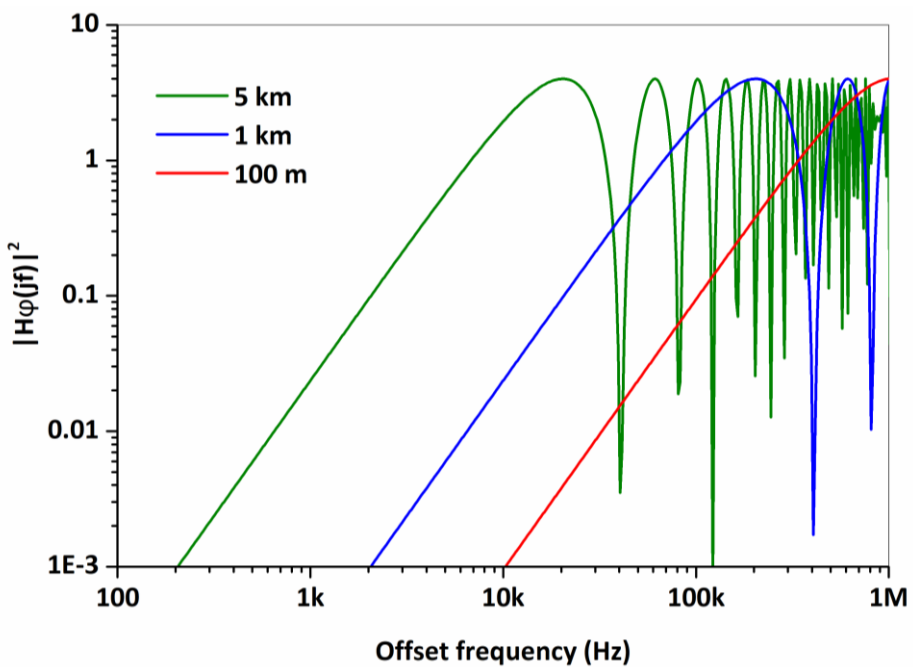


Figure 3-2 Delay-line transfer function for three different delay-line lengths (100m, 1 km and 5 km)

3.1.3.2 Measurement of Mixer Voltage Gain Coefficient (K_{ϕ})

In order to calculate phase noise from mixer output voltage using equation 3-4, mixer voltage gain coefficient, K_{ϕ} must be known. This quantity depends on the particular mixer as well as the power levels at RF and LO ports of the mixer and needs to be determined experimentally. K_{ϕ} (which is measured in V/rad [60]) was calculated by applying two signals with slightly different frequencies close to the frequency of the SUT (10 GHz and 10.0001 GHz) and measuring the zero-crossing

Chapter 3

slope of the beat signal (at 100 kHz) [63]. The signals were generated from two signal generators that were phase-locked and the signal power levels were set to the power levels expected at the RF and LO ports of the mixers during the phase noise measurement.

3.1.3.3 Noise Floor Estimation

The noise floor of the photonic-delay phase noise measurement scheme can be estimated by connecting the SUT to the phase noise measurement setup and measuring the mixer output signal without a delay-line in the phase noise measurement setup. Then, when a delay-line (e.g., 1 km) is used in the phase noise measurement setup, the noise floor can be estimated by using equation 3-2 and equation 3-4, substituting the mixer output signal measured without a delay-line as V_{out} and substituting the delay induced by the delay-line (e.g., the delay induced by 1 km delay-line) as τ [58].

3.1.3.4 Phase Noise Measurement and Processing

When recording base-band voltage fluctuations of the mixer output using the spectrum analyser, measurements were recorded at different frequency ranges (DC-500 Hz, DC-1 kHz,..., DC-1 MHz, DC-10 MHz) and then stitched together after dividing by the respective resolution bandwidth (RBW). The stitched spectrum was then corrected according to equation 3-4 to generate the SSB phase noise spectrum. The stitching of measurements obtained at different frequency ranges is necessary to generate an accurate phase noise spectrum in a logarithmic offset frequency scale. The MATLAB code for processing phase noise measurement data was provided by J. Kim.

3.2 Long-term Stability

In addition to the short-term signal fluctuations measured by the phase noise, the nominal frequency of signal may vary over longer time scales as well. In general, signal variations occurring over time scales of >1 s are characterized under long-term stability. The Long-term stability of a signal can be characterized by measuring its frequency variations/drifts relative to a stable reference signal in time domain.

3.2.1 Long-term Frequency Stability Measurement Setup

I built the setup shown in Figure 3-3 to measure the long-term frequency variations of signals in my experiments. In this setup, the reference signal and SUT are fed into a mixer. The mixer output signal corresponding the difference between the SUT and the reference signal is fed into a frequency counter (FXM50, Menlo Systems GmbH, Germany) to record the frequency difference between the two signals at 1 s intervals. The frequency counter is locked to a 10 MHz reference

signal (from RefGen 10491, TimeTech GmbH, Germany) which in turn is synchronized a to Global positioning System (GPS) signal.

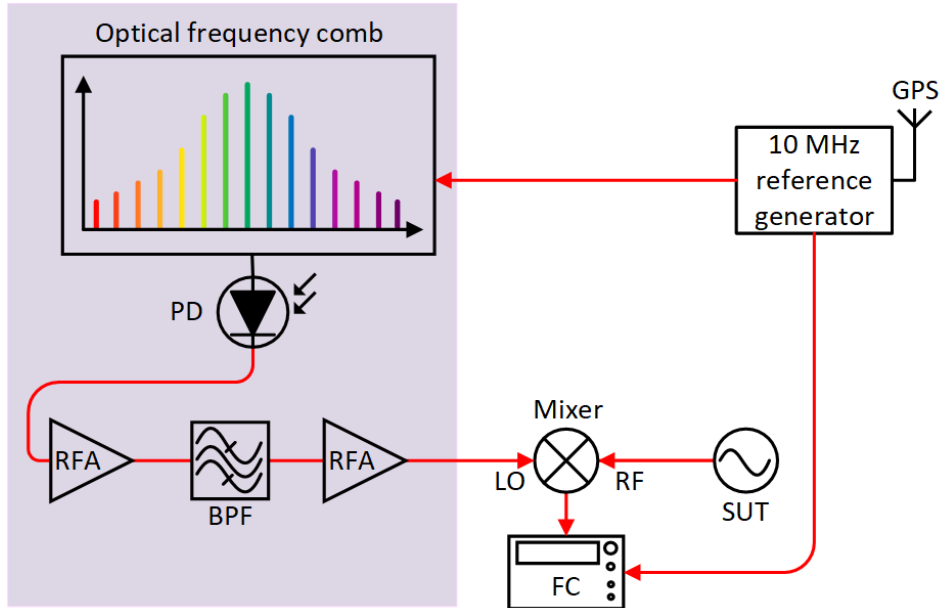


Figure 3-3 Reference signal generation and frequency variation measurement setup.

PD: Photodiode, RFA: RF amplification, BPF: Band-pass filter, FC: Frequency counter, SUT: Signal under test.

Optical paths are shown in black and electrical paths are shown in red.

3.2.1.1 Reference Signal Generation

The reference signal for the SUT to be compared with is derived from an optical frequency comb generator (FC1500, Menlo Systems GmbH, Germany) and the reference signal generating setup is shown inside the shaded area in Figure 3-3. The nominal repetition rate, f_{rep} (i.e., the mode spacing between comb tones) of the optical frequency comb is 250 MHz and the repetition rate can be locked to an external reference signal. When the optical signal of the optical frequency comb is detected by a photodiode, an electrical comb signal with 250 MHz mode spacing can be obtained. By using an RF band-pass filter with the appropriate pass-band, a single RF tone can be isolated to be used as a stabilized reference signal.

For my experiments, I set the repetition rate of the optical frequency comb to 248.75 MHz and the repetition rate was locked to a 10 MHz GPS-synchronized reference signal (RefGen 10491, TimeTech GmbH, Germany the same reference signal the frequency counter was locked into). The 40th tone of the electrical signal at the output of the photodiode was filtered using a RF band-pass filter at 9.95 GHz with 50 MHz bandwidth, isolating a stabilized reference signal at 9.95 GHz (= 248.75 MHz × 40).

3.2.2 Allan Deviation

Allan deviation, σ_y , is a statistical tool used to characterize the long-term stability of a signal. Allan deviation can be computed from the frequency variations of a signal measured in time domain.

The square of σ_y , Allan variance (σ_y^2) is calculated according to [65],

$$\sigma_y^2(\tau) = \frac{1}{2(M-1)} \sum_{i=1}^{m-1} [y_{i+1} - y_i]^2, \quad 3-5$$

where y_i is the i^{th} fractional frequency measurement. M is the number of fractional frequency measurements and τ is the sampling time over which y_i was measured. The fractional frequency y_i is given by [65],

$$y_i = \frac{f_i - f_0}{f_0}, \quad 3-6$$

where f_i is the mean frequency of the signal during the i^{th} sampling interval and f_0 is the nominal frequency of the signal.

Both standard deviation and Allan deviation are measures of the deviation of a set of data from the nominal value. The standard deviation uses the mean of the whole data set for the calculation. However due to the various types of associated noise, the mean of a signal may not stay stationary and may vary with the number of samples. In these cases, the standard deviation will also vary depending on the number of samples (i.e. not being convergent). This makes standard deviation unsuitable for frequency stability measurements [65]. In contrast, Allan deviation considers the deviation between adjacent data points, giving convergent results for most types of noise [65]. It should be noted that in addition to the standard Allan deviation shown above, different versions of the Allan deviation such as overlapping Allan deviation and modified Allan deviation providing improved confidence intervals and better distinguishability between noise types have also been introduced [65]. In my work, I used the standard Allan deviation. The MATLAB code for processing Allan deviation was provided by J. Kim.

3.3 Long-term Stability of Optical Fibre Delay-line Based OEOs

Incorporation of optical fibres as the energy storage elements can be considered as the popular method of generating low phase noise microwave signals using OEOs because the phase noise levels can be lowered by incorporating longer optical fibres which are readily available. In fact, phase noise as low as -163 dBc/Hz at 6 kHz offset frequency in a 10 GHz OEO has been obtained by using a 16 km long optical fibre delay-line in an OEO [25].

However the incorporation of optical fibre delay-lines in OEOs can be problematic because the delay induced by an optical fibre is susceptible to the variations of the ambient temperature [13], [14]. Hence when an optical fibre delay-line is incorporated, the loop delay of the OEO and the FSR of the OEO loop (which is inversely proportional to the loop delay) also become susceptible to ambient temperature variations. As a result, the OEO output signal frequency which is a multiple of the FSR of the OEO loop also gets affected by ambient temperature variations. These ambient temperature variations in general occur at time scales >1 s and hence affect the long term stability of the OEO signal.

3.3.1 Active Long-term Stabilization of OEOs

Thermal stabilization of OEO components is one way of minimizing temperature induced frequency variations and improving the long-term stability. A reduction of temperature induced frequency drifts from $-8.3\text{ppm}/^\circ\text{C}$ to $-0.1\text{ ppm}/^\circ\text{C}$ has reportedly been achieved in a 10 GHz OEO by stabilizing the temperature of the optical fibre delay-line and the RF band-pass filter in the OEO above the ambient temperature, by using resistive heating elements and temperature controllers [66]. Furthermore it has been reported that the 16 km long optical fibre delay-line in the previously mentioned low phase noise OEO [25] was also thermally stabilized to reduce frequency drifts.

Locking the OEO to a stabilized reference signal has also been used as a method improving the long term stability of OEOs. A tuneable OEO (2 to 4 GHz) locked to a reference signal generated from an optical frequency comb has been reported [67]. The long term stability of the OEO in terms of the overlapping Allan deviation is reported to be of 1.2×10^{-15} at 1 s sampling time. In order to improve the stability, optical frequency comb, the OEO and optical phase detectors used in this setup have been placed in actively temperature controlled containers.

In ref. [68], an OEO with 3 GHz output signal has been locked to microwave reference signal synthesized from a maser. In this case, the long-term stability of 2.79×10^{-12} at 1 s sampling time (in terms of overlapping Allan deviation) has been reported. The optical delay-line, the optical modulator and the band pass filters in this setup have been thermally stabilized by placing in thermal enclosure boxes.

However these active stabilization methods require additional components and/or external reference signals; hence increase the size, complexity, and decrease the portability of the OEO. On the other hand, implementation of a passive stabilization method can be more attractive in many applications. Using an optical fibre delay-line with low temperature sensitivity can be seen as one of the most convenient ways of passively improving the temperature stability in an OEO.

The possibility of doing this can be identified by understanding the factors affecting the temperature induced delay changes in optical fibres.

3.3.2 Temperature Sensitivity of Optical Fibres

The temperature induced delay change in an optical fibre arises due to two main effects: the temperature induced group index (n_g) change in the guided mode and the temperature induced length change of the fibre [13]. The parameter thermal coefficient of delay (TCD), by which the temperature induced delay change is characterized is given by [13], [14],

$$TCD = \frac{1}{L} \frac{d\tau}{dT} = \frac{n_g}{Lc} \frac{dL}{dT} + \frac{1}{c} \frac{dn_g}{dT}, \quad 3-7$$

where τ is the induced delay, T is the temperature, L is the length of the fibre, and c is the speed of light in vacuum. The first term in the right-hand-side of equation 3-7 represents the effect of the length change and the second term in the right-hand-side represents the effect of group index change [14].

Approximating n_g with the refractive index of fused silica, $n=1.44$, using the thermal coefficient of expansion, $dL/dT=4.1\times10^{-7}$ m/K and the thermal coefficient of refractive index (thermo-optic coefficient), $dn/dT=1.1\times10^{-5}$ K⁻¹ (near 1550 nm) of fused silica [69], it can be calculated that for an unjacketed silica-glass based solid-core fibre (such as standard single mode fibre, SMF), the contribution to the TCD from group index change is 37 ps/km/K while the contribution to TCD from fibre length change is 2 ps/km/K [14]. The calculated total TCD of 39 ps/km/K agrees with the experimentally measured TCD values of SMFs [14], [70].

The application of special fibre coatings to counterbalance the effects of the index changes and length elongations is one way of reducing the thermally induced delay changes in optical fibres. Such specially coated SMFs with reduced TCD are commercially available. For example, the Strong Tether Fiber Optic Cable (STFOC) from Linden photonics, USA uses a liquid crystal polymer (LCP) coating and has a measured TCD of 5.6 ps/km/K [70]. In addition, the Phase Stabilized Optical Fiber from Furukawa Electric, Japan uses a silicone resin coating, followed by a LCP coating and the measured TCD is 3.7 ps/km/K [70].

However evaluation of equation 3-7 for a silica-glass based solid-core fibre showed that the effect of group index change on TCD is around 20 times higher than the effect of fibre elongations (37 ps/km/K vs. 2 ps/km/K). This suggests an alternative way of reducing TCD of optical fibres. That is, by changing material through which light is guided in the fibre (in other words, by using a core

material with a refractive index less sensitive to temperature variations), a considerable reduction in TCD can be achieved.

HC-PBGFs, in which more than 99% [15] of light can be guided through the air-filled hollow core can be identified as a suitable candidate for this application. Since air has a negligible thermo-optic coefficient at constant volume (e.g., in a HC-PBGF spliced from both ends) [14], [16], the temperature induced group index change and therefore the TCD can be expected to be significantly lower in HC-PBGFs compared to solid-core SMFs. Further details about HC-PBGFs including their temperature sensitivity are discussed in the next chapter.

Chapter 4 Hollow-core Photonic Bandgap Fibres

The possibility of using HC-PBGFs as optical energy storage elements in OEOs to minimize temperature induced frequency drifts and improve the long-term stability was identified in the previous chapter. The properties of HC-PBGFs are discussed further in this chapter. HC-PBGFs are a class of microstructured fibres and as the name suggests, the transverse structure of a microstructured fibre is more complex than that of a standard SMF with a solid core and a solid cladding. Various types of microstructured fibres with different transverse structures and light guiding mechanisms have been introduced over the years. The first part of this chapter provides an overview of different light guiding mechanisms of microstructured fibres. The rest of this chapter is dedicated to discuss HC-PBGFs. In particular, the temperature sensitivity of HC-PBGFs is discussed in detail together with other properties and applications of HC-PBGFs. The basics of HC-PBGF fabrication are also discussed.

4.1 Guiding Mechanisms in Microstructured Optical Fibres

4.1.1 Index-guiding Fibres

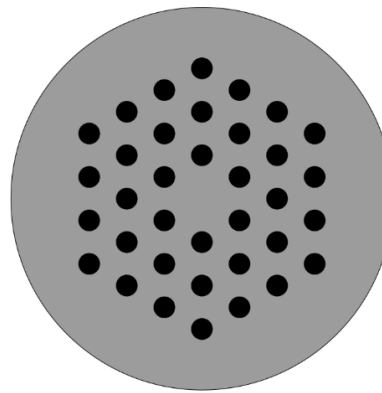


Figure 4-1 Representative cross-sectional sketch of an index-guiding fibre. Solid core region is surrounded by an air-holed micro structure.

This is similar to the light guiding mechanism of conventional step-index fibres where the high refractive index core is surrounded by a lower refractive index cladding and light is confined in the core via total internal reflection. Equivalently, in index-guiding microstructured fibres, a solid core region can be surrounded by a cladding region with air holes (see Figure 4-1). Due to the air-holed microstructure, the average refractive index of the cladding region is lower than that of the core region so that light is confined in the core [71], [72]. It has been shown that the air-hole

arrangement of the cladding does not need to be periodic for this guiding mechanism to work [73].

4.1.2 Photonic-bandgap-guiding Fibres

In photonic-bandgap-guiding mechanism, the periodic microstructure that surrounds the core region acts as a photonic-bandgap and light with wavelengths that lie within the bandgap is not allowed to pass through the cladding and hence get confined in the core [71]. In other words, light with wavelengths within the bandgap are coherently reflected back to the core by the periodic cladding microstructure [71]. Bragg fibres [74] can be considered as the first photonic bandgap-guiding fibres that were proposed. Bragg fibres have a 1-dimensional structure where the core is surrounded by a cladding with concentric high and low refractive index layers (see Figure 4-2a). The more common 2-dimensional structured HC-PBGFs have an air-filled core surrounded a by triangularly arranged air-hole structure [22] (see Figure 4-2b).

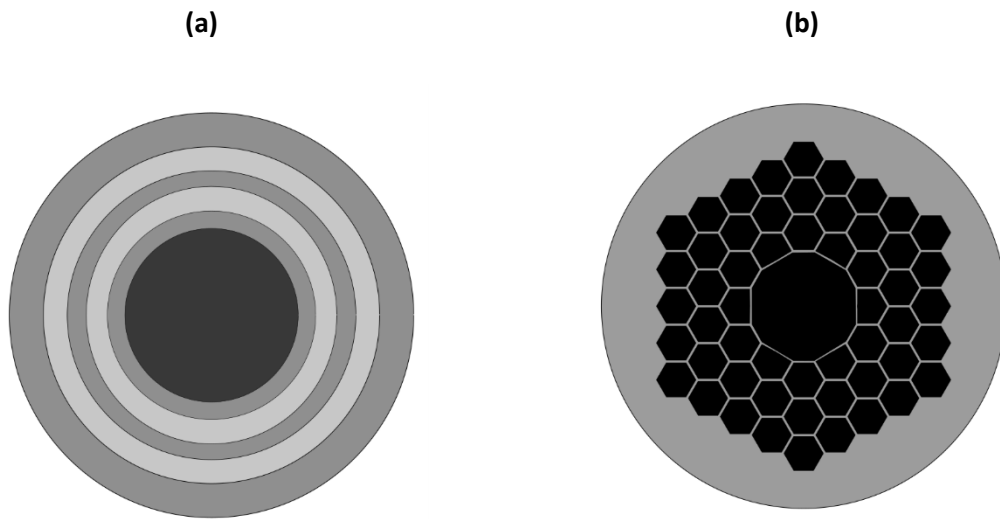


Figure 4-2 Representative cross-sectional sketches of bandgap-guiding fibres. (a) 1-D case: core is surrounded by concentric high and low refractive index layers (Bragg fibre), (b) 2-D case: hollow-core is surrounded by a 2-dimensional periodic air-holed structure.

4.1.3 Anti-resonant-guiding Fibres

In anti-resonant guiding mechanism, the micro-structured cladding layers act as Fabry-Perot (FP) like resonators. Light with wavelengths within the resonant band of FP-resonators is transmitted through the cladding and light with other wavelengths gets confined into the core due to antiresonant reflections [75]. Kagomé-latticed fibres (see Figure 4-3a) are one category of fibres that guide light according to this mechanism [76]. However it has also been shown that wave

guiding and spectral properties of an antiresonant guiding fibre is mainly determined by the thickness of the first cladding layer surrounding the core [75], [76]. Following this, anti-resonant guiding fibres with more simplified cladding structures have also been demonstrated, e.g., nested anti-resonant fibre (see Figure 4-3) [77].

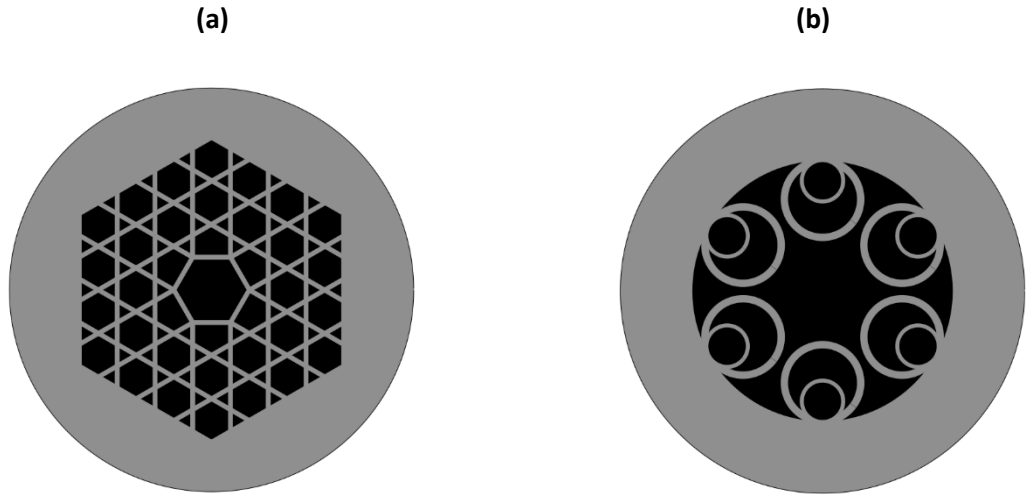


Figure 4-3 Representative cross-sectional sketches of anti-resonant guiding fibres. (a) Kagomé latticed fibre, (b) nested anti-resonant fibre with simplified cladding structure.

4.2 Hollow-core Photonic Bandgap Fibres

4.2.1 Basics of HC-PBGF Fabrication

HC-PBGFs are fabricated by the so called stack-and-draw process [15], [22]. First, silica glass capillaries of meter-scale lengths and millimetre-scale diameters are stacked together and packed tightly inside a jacketing tube. The hollow core is formed by removing capillaries from the centre of the stack. This stack is then drawn into millimetre-scale diameter preform under high temperature and high pressure to merge capillaries and form the microstructured cladding. This preform, after placing in a jacketing tube, is drawn again to fabricate HC-PBGFs with hundred-micrometre-scale outer diameter. The operational wavelength of the fibre can be tuned by varying the periodicity of the cladding [22].

A common way of categorizing HC-PBGFs is by the number of capillaries removed to form the core. For example, if 19 capillaries are removed, the fibre can be called a 19-cell (or simply 19c) core structured fibre. The number of removed capillaries can be 3, 7, 19 or even 37 [22].

HC-PBGF fabrication process is yet to be perfected and currently the record for the longest length of a HC-PBGF is at 11 km (the fibre had a 19-cell core structure) [78]. In addition, even though it

has been theoretically predicted that propagation loss in HC-PBGFs can be of the order 0.1-0.15 dB/km [22], [79], the lowest propagation loss reported in a HC-PBGF is 1.2 dB/km (in a 19-cell core structure fibre) [79]. Confinement losses of HC-PBGFs can be decreased by increasing the number of layers (rings) of the microstructure cladding [22]. However the propagation loss of HC-PBGFs are ultimately limited by the scattering due to the surface roughness at air-glass surfaces [22], [79]. Increasing the core size is one way of reducing propagation losses but at the cost of higher order mode propagation [22].

4.2.2 Properties and Applications of HC-PBGFs

Since more than 99% of light can be guided in the air-core [15], HC-PBGFs exhibit interesting characteristics which are desirable for many applications [22]. For example, nonlinearities that impose limitations of high power delivery in solid core fibres [80] are much suppressed in hollow-core fibres: can be >1000 times lower than that of silica-core fibres [81]. This makes HC-PBGFs a suitable candidate for high power delivery applications. Applications such as high-power coherent beam combining can benefit from cw beam delivery in HC-PBGFs [80]. High-power pulses can potentially be delivered through HC-PBGFs in applications such as precision machining applications [82], multi photon microscopy, and skin treatments in medicine [22].

Speed of light in silica-glass is 31% slower than the speed of light in a vacuum [15]. This introduces an inherent latency to data transmission in silica-core fibres. However since almost all the light is guided in the air-filled core, a significant latency reduction can be expected in data transmission with HC-PBGFs [15]. Light propagation in a 19-cell HC-PBGF at 99.7% of speed of light in vacuum has been demonstrated [15]. Furthermore, >15 μ s latency reduction in data transmission compared to silica-core fibre (SMF) has been successfully demonstrated by transmitting data through a 11 km long 19-cell HC-PBGF [78].

In addition to low-latency data transmission, HC-PBGFs have shown more desirable characteristics for telecommunications by demonstrating a low-loss (3.5 dB/km), 160 nm (at 3 dB bandwidth) [15] wide transmission window in a 19-cell structured fibre, which is wider than the combined width of the current L and C telecommunication bands [22]. Furthermore, long distance data transmission up to 74.8 km with 19-cell core-structured fibres (in an optical transmission loop experiment) [83] and 73.7 Tb/s high-capacity mode-division multiplexed data transmission in a 37-cell core-structured, 310 m long fibre [84] have been demonstrated.

Interesting demonstration of particle levitation and guidance through a HC-PBGF has been done where polystyrene spheres of \sim 5 μ m diameter are guided a distance of 15 cm, at a speed of 1

cm/s, in a 20 μm core-diameter HC-PBGF, using 80 mW laser operating at 514.5 nm [85]. This can be used to transport atoms between chambers in atomic physics applications [86], trapping and manipulating bacteria and viruses in biological applications [87], in micro-machining applications [88], etc.

Ionizing radiation can create defects in fused-silica regions of optical fibres. Light transmitted through optical fibres gets attenuated due to these defects and this process is known as radiation induced attenuation (RIA) [89]. The air-core guidance structure, suggests that HC-PBGFs can be better in terms of radiation hardness (tolerance to RIA) compared to standard solid-core fibres. In fact, two orders of magnitude lower RIA in a 201 m long 19-cell HC-PBGF compared to standard fibre (SMF28e+) has been experimentally shown by exposing the fibres to radiation levels above 940 kGy [90].

HC-PBGFs can also be used for sensing applications [22], [91]. Gas sensing can be done by filling the hollow core of the fibre with gas to fabricate gas cells. Sensing can be done by launching light through the HC-PBGF cell and then detecting. The interaction length can be increased by increasing the fibre length to potentially increase the sensitivity [91]. HC-PBGF based acetylene [92], ammonia [93], carbon dioxide [94], etc. have been demonstrated. Another adaptation is to use HC-PBGFs to fabricate all-fibre gas cells by trapping gas in the hollow-core to be used as frequency references, e.g., in laser stabilization applications [95]. In addition, liquid sensing [96], strain sensing in a Fabry-Perot-type setup (by splicing HC-PBGF between two SMFs) [97], and acoustic pressure sensing by employing a HC-PBGF in one arm of a Michelson interferometric setup [98] have also been reported.

When it comes to polarization properties of HC-PBGFs, it has been shown that HC-PBGFs can become birefringent due to core asymmetries [20], [99], [100] and that highly birefringent HC-PBGFs can be fabricated by intentionally distorting the core symmetry [99], [100]. Birefringence (differential group index between the two polarization modes) as high as 0.025 (corresponding to a beat length of 62 μm) at 1550 nm have been experimentally demonstrated in HC-PBGFs [100] and high-birefringent fibres have various applications in communications, sensing, etc. However it has also been shown that spurious guided modes known as surface modes physically localized at the core surround interface of HC-PBGFs [22] are highly sensitive to structural distortions [101] and that interactions between surface modes and core modes can lead to PDL in HC-PBGFs [21], [22]. Furthermore strong polarization mode coupling has also been observed in HC-PBGFs and it has been suggested that the mode overlapping that occur at structural defects of HC-PBGFs is the reason for this polarization mode coupling [21].

4.2.2.1 Temperature Sensitivity of HC-PBGFs

As mentioned before, since more than 99% [15] of light can be guided through the air-filled core and since air has a negligible thermo-optic coefficient at constant volume [14], [16], temperature induced delay change in HC-PBGFs due to temperature induced group index change is greatly reduced. Hence the TCD of a HC-PBGF would be mainly determined by the temperature induced fibre elongations. Using the first term of the right-hand-side of equation 3-7 and assuming a group index of 1.003 [15], the TCD due to fibre elongations in a HC-PBGF can be calculated to be around 1.4 ps/km/K [14]. However it should be noted that due to the residual light propagation in glass, TCD can still be slightly affected by the refractive index changes of glass (e.g., ~ 0.1 ps/km/K if 0.3% of light is propagated in glass) [14]. Furthermore the jacket and the coating can also change the TCD (by >1 ps/km/K) [16]. Nonetheless experimentally measured TCD values of 2 ps/km/K [14] in HC-PBGFs (which is even lower than the TCDs of speciality coated fibres), already prove the superior thermal insensitive properties of HC-PBGFs.

Furthermore it has been suggested in the literature that fibre elongation limited TCD of a HC-PBGF can be further reduced and even reach zero and negative TCD values [16]–[18]. Ref. [16] provides a good physical interpretation of how these TCD characteristics can be achieved. The increase of temperature changes the HC-PBGF microstructure and red-shifts the centre-wavelength of the photonic bandgap. Consequently, the power guided in glass gets modified and causes group index to decrease near the long-wavelength edge of the bandgap (and causes group index to increase near the short-wavelength edge of the bandgap). The decrease of group index makes light travel faster near the long-wavelength edge of the bandgap when temperature is increased. Hence the effect of the thermal elongations of fibre gets counterbalanced by the increase of the light propagation speed. Therefore by tuning operational wavelength of light properly, zero and even negative TCD characteristics can be achieved in the fibre [16].

Ref. [16] further states that the TCD characteristics depend on the chromatic dispersion (which is the first derivative of the group delay) of the HC-PBGF, and with an approximated analysis, suggests that zero-TCD can be obtained when the chromatic dispersion is around 79 ps/nm/km. Since the chromatic dispersion of HC-PBGFs typically varies from large negative values to large positive values across the bandgap, in theory, zero-TCD characteristics can be obtained in any HC-PBGF by operating at the right wavelength [16]. However it should be noted that to be used in a practical application, the insertion loss of a HC-PBGF at zero-TCD wavelength needs at an acceptable level as well. Ref. [16] also provides experimental results of zero and negative TCD characteristics measured on a coated 7-cell HC-PBGF. Zero-TCD characteristics of the fibre were obtained at 1531 nm. The chromatic dispersion of the fibre was 83 ps/nm/km at this wavelength.

Even though the exact zero-TCD wavelength of a real fibre also depend on parameters such as fibre jacket and coating [16], it can be seen that the wavelength corresponding to the chromatic dispersion of 79 ps/nm/km can be used to get a good estimation of the zero-TCD wavelength of the HC-PBGF.

Due to these ultra-low temperature sensitive characteristics, it can be clearly seen that a significant temperature stability improvement can be achieved using HC-PBGFs, not only in OEOs, but also in various other applications. For example, they can potentially be used in precise timing and synchronization applications, such as, in synchrotrons [102], linear particle accelerators, phase arrayed antennae, telescope arrays [14], synchronization of robots in manufacturing plants, and 5G networks [16], [103]. Reduction of thermal sensitivity in a fibre-optic gyroscope by using HC-PBGFs has also been demonstrated [104] and in addition, HC-PBGFs can potentially be used in applications such as delay-line based laser stabilization systems as well [16], [105].

Chapter 5 Passive Fibre-optic Depolarizers

The performance of many optical systems ranging from space-based instrumentation and spectrometers [106]–[108] to imaging systems [109], and various fibre-optic systems [110]–[116] suffers from performance limitations due to polarization sensitivity. In such cases, depolarizers can be introduced to the respective systems to suppress the polarization bias.

In the previous chapter, it was mentioned that HC-PBGFs can inherit undesired polarization properties such as PDL and polarization mode coupling. It can be anticipated that such properties may affect the performance of HC-PBGF delay-line incorporated OEOs. Employing a depolarizer in the OEO can be foreseen as a possible method of mitigating this issue. Hence I decided to develop a depolarizer that can potentially be employed not only as a part of a HC-PBGF delay-line incorporated OEO but also as a stand-alone device that can be used in other possible applications.

Various depolarizers that differ in terms of the domain of operation, active or passiveness, the structure, the linewidth of the input signal that can be depolarized, etc. can be found in the literature. In the first part of this chapter, various types of depolarizers are discussed by categorizing them in terms of their domain of operation. In the second part of the chapter, passive fibre-optic depolarizers that are more appropriate to be employed in fibre-optic systems are further discussed.

5.1 Depolarizers in Terms of the Domain of Operation

Depolarizers are a family of optical devices capable of decreasing the degree of polarization (DOP) of input signals. They are capable of varying the state of polarization (SOP) of input signals so that when averaged, the effective DOP of the input signal is reduced. Depending on the domain of operation (averaging), depolarizers reported in the literature can be categorized into three groups: spatial, temporal, and spectral [117].

Depolarizers operating in the spectral domain vary the SOP of different spectral components of the input signal [118]. The spectral domain depolarizer proposed by Lyot [119], known as the Lyot depolarizer consists of two cascaded birefringent crystal plates with 1:2 thickness ratio and their birefringent axes (fast and slow) are rotated by 45° with respect to each other. The plates induce a differential delay between the orthogonal components of the input signal (along slow and fast axes) propagating through them and the signal gets effectively depolarized when the differential delay is larger than the coherence time (τ_c) of the signal [120].

Chapter 5

Since the coherence time of an optical signal is inversely proportional to its linewidth (linewidth in general is measured by the Full width at half maximum, FWHM), crystal plate based Lyot depolarizers, due to limited thickness of crystal plates (and hence limited differential delay) are only capable of depolarizing broadband input signals ($FWHM > 10s$ of nanometres). However the same concept can be implemented by using birefringent fibres [121] to depolarize narrower linewidth signals and these depolarizers are known as fibre-Lyot depolarizers. In addition, the concept of achieving depolarization by decorrelating orthogonal components of an input signal has also been implemented in optical fibre based Mach-Zehnder type [122], [123] and Michelson type [124], [125] interferometric setups, varying the technique of inducing differential delays in order to improve the narrow-linewidth signal depolarization capabilities.

Depolarizers operating in spatial domain achieve depolarization by varying the SOP across the beam cross-section of the output signal. The Cornu depolarizer is a cuboid formed by optically contacting two 45° quartz wedges. The wedges introduce a retardation that varies periodically across the beam cross-section of input signal. The purpose of the double-wedged structure is to keep the input and output beams collinear [126]. The more compact quartz-silica depolarizer also has a double wedged structure. However the two wedges are made of two different materials (quartz and silica). Furthermore the wedge angles are much smaller (around 2° [126]) and as a result the period of SOP variation is larger [126]. Liquid crystal based spatial depolarizers have also been demonstrated [127], [128]. These depolarizers can be regarded as clusters of half-wave plates with optical axes aligned in different directions to introduce a non-uniform retardance across the beam cross-section [128]. These spatial domain depolarizers are capable of depolarizing input signals irrespective of the signal linewidth.

Temporal domain depolarizers, also known as polarization scramblers, rapidly vary the SOP of the input signals in time domain to minimize the DOP (on average). Billings proposed one such depolarizer consisting of rotating quarter-wave and half-wave plates [129]. Other methods of obtaining a similar operation include launching input signals through cascaded acousto-optic TE-TM converters [130] and cascaded electro-optic modulators [131] which are being modulated by electrical signals and cascaded electrically controlled fibre squeezers [132]. In addition, signals can also be launched through birefringent fibre wound on a piezo-electric cylinder to obtain a temporal SOP variation [133]. The performance of these active depolarizers are independent of the input signal linewidth.

Optical fibre based loop structured depolarizers (also known as ring depolarizers) [134]–[137] can also be considered as operating in temporal domain. In these depolarizers, depolarization is obtained by recombining the input signal with delayed versions of itself by launching a portion of

the input signal through an optical fibre loop. This recombination must be incoherent and to do so the delay induced by the fibre loop must be greater than the coherence time of the input signal [134]. Hence the performance of the looped-depolarizers are subjected to the linewidth of the input signal.

5.2 Passive Fibre-optic Depolarizers for Fibre-optic Systems

When it comes to the incorporation of depolarizers into fibre-optic systems in particular, it is clear that the integration of a free-space optics based spatial-domain depolarizer [126]–[128] or crystal plate based Lyot depolarizer [119] is practically challenging. On the other hand, even though some temporal domain depolarizers can be fibre-coupled [130]–[133] to be integrated with fibre-optic systems, they are active devices (except looped depolarizers) that require additional electrical drivers for operation, and hence can be undesirable in terms of complexity, size, cost etc., for some applications.

Alternatively, passive fibre-optic depolarizers can offer more feasible means of delivering depolarized light into optical fibre based systems. However the performance of these depolarizers depends on the decorrelation of the components of input signal, and hence on the linewidth of the input signal. For applications such as fibre amplifiers [110], fibre-optic gyroscopes [111], distributed impact sensors [112], and surface plasmon resonance sensors [113] where relatively broad-linewidth sources (in the scale of nanometres) are used, depolarization can be done by using a fibre-Lyot depolarizer. However applications such as polarization insensitive measurement systems [114], high-resolution distributed strain and temperature sensing [115] and four-wave mixing systems [116] in which narrow linewidth sources (<10 MHz) are preferred, depolarization is more challenging because narrow linewidth signal depolarization requires longer differential delays to be induced for depolarization.

Passive fibre-optic depolarizers reported over the years vary in their ability to depolarize broad and narrow linewidth signals and depending on the architecture, they can be categorized into linear and loop structured depolarizers. Furthermore cascading of individual depolarizing units can be seen as a common method of achieving depolarization irrespective of input signal SOP.

Loop structured depolarizers based on both fibre couplers and polarization beam splitters (PBSs) have been proposed. As mentioned before, in these depolarizers, the loop delay needs to be larger than the coherence time of the input signal. Furthermore in coupler-based depolarizers, SOP through the loop must be maintained. This can be done by using polarization-maintaining (PM) fibre based loops [134] or SMF based loops with polarization controllers [135], or by bending/twisting the SMF loop [137]. Depolarization of an input signal with 10 m coherence

length (corresponding to 10s of megahertz linewidth) using a 12 m SMF loop has been demonstrated [137]. However the need to manually control the polarization in coupler based loop depolarizers with SMFs can be undesirable for some applications. Coupler based depolarizers with PM fibre loops do not need manual control of polarization in the loop however can be costly when it comes to narrow linewidth signal depolarization (e.g., depolarization of input signals with few megahertz linewidths require 100s of metres of PM fibres). The reported PBS based loop depolarizer uses SMF loops and does not need manual polarization control through the loops [136]. Narrow linewidth signal depolarization (less than 1 MHz linewidth) has been demonstrated with this depolarizer using 2 km long SMF loops. However the reported depolarizer had a relatively high insertion loss (9 dB) and a relatively high residual DOP (<10%).

Fibre-Lyot depolarizers, Mach-Zehnder structured depolarizers, and Michelson structured depolarizers can be categorized under linear depolarizers. Similar to the original crystal plate based Lyot depolarizer, a fibre-Lyot depolarizer consists of two birefringent fibres (e.g., PM fibres) with 1:2 length ratio, joint with a 45° relative rotation between their birefringent axes (see Figure 5-1). This configuration of two depolarizing stages allows an input-SOP independent depolarization and the 1:2 length ratio avoids decorrelated input signal components in the first fibre section being recorrelated in second fibre section [118]. By using a fibre-Lyot depolarizer with 1 km and 2 km PM fibre sections, an input signal with ~2 GHz linewidth can be depolarized. Hence it can be seen that even though this simple fibre-Lyot depolarizer configuration can easily be fabricated with low insertion loss, it is not suitable for narrow linewidth signal (10s of megahertz or lower) depolarization due to impractical fibre length requirements.

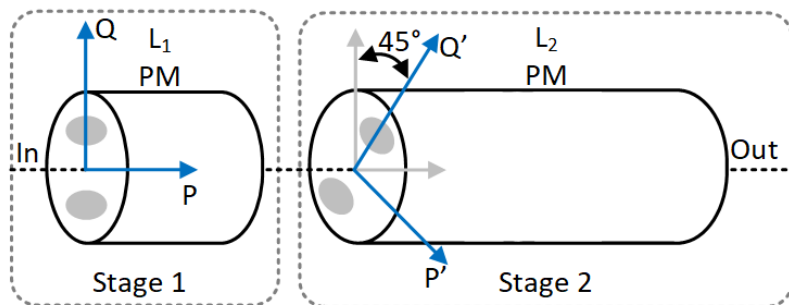


Figure 5-1. Schematic of a fibre-Lyot depolarizer [121] with two jointed PM fibre sections with 1:2 length ratio. Birefringent axes of the two fibres are rotated by 45° with respect to each other.

Rather than inducing differential delays by launching the components of input signal along the slow and the fast axis of the same fibre, the input signal can be split and launched through two fibre paths with dissimilar lengths to induce some orders of magnitude larger differential delay in order to depolarize narrow linewidth signals. In a Mach-Zehnder structured linear depolarizer, the

input signal is split by a PBS into two orthogonal components and one component is delayed with respect to the other by launching through an optical fibre delay-line. The two components are then recombined with orthogonal SOPs using a second PBS [122]. An input-SOP independent depolarizer can be constructed by cascading two such depolarizing sections (with 1:2 differential delay ratio) through a fibre coupler [123] (this configuration will be referred to as the Mach-Zehnder depolarizer in the text). The reported input-SOP independent Mach-Zehnder depolarizer (shown in Figure 5-2) uses SMF delay-lines with polarization rotators (to align polarization) to induce delays and has only been used to depolarize an input signal with 1 m coherence length (which corresponds to 100s of megahertz signal linewidth). This configuration not only has a relatively low insertion loss (1.5 dB in the reported one) but can also be used to depolarize narrow linewidth signals (10s of megahertz and lower). However since SMFs are not capable of retaining SOP of a signal over a long length, for stable operation and post-fabrication alignment-free narrow linewidth depolarization, PM fibre delay-lines must be used to induce delays and the rest of the components (fibre coupler and PBSs) must also be PM-type. An Input-SOP independent all-PM depolarizer based on Mach-Zehnder depolarizer configuration has not been reported so far to the best of my knowledge.

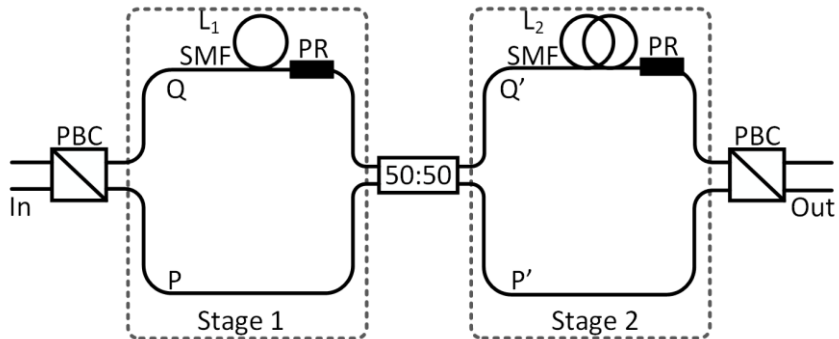


Figure 5-2. Schematic of an input-SOP independent Mach-Zehnder depolarizer with SMF delay-lines [123]. Two depolarizing stages are cascaded through a 50:50 coupler. PBS: Polarization Beam Splitter, PR: Polarization Rotator.

Michelson structured linear depolarizer allows SMFs to be used to induce differential delays in a reflection based configuration [124], [125]. In this configuration, the input signal is split by a PBS and launched through two dissimilar lengths SMFs connected to Faraday rotator mirrors (FRMs). The input signal components get reflected from FRMs and propagate back through SMFs accumulating a differential delay and exit the PBS. Based on this concept, an Input-SOP dependent single stage depolarizer [124] and an input-SOP independent depolarizer [125] (which will be referred to as the Michelson depolarizer in the text) with two depolarizing stages cascaded through a half-wave plate (shown in Figure 5-3) have been reported. The reported Michelson depolarizer with 2.5 km and 5 km SMF delay-lines has reportedly depolarized a narrow linewidth

input signal of 0.7 MHz linewidth. However the insertion loss of the device was relatively high (15.5 dB).

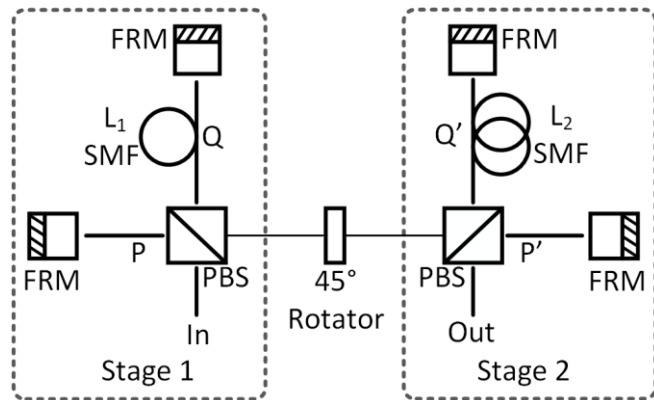


Figure 5-3 Schematic of an input-SOP independent Michelson depolarizer with SMF delay-lines [125]. Two depolarizing stages are cascaded through a wave-plate. PBS: Polarization Beam Splitter, PR: Polarization Rotator, FRM: Faraday rotator mirror.

Chapter 6 Incorporating Hollow-core Photonic Bandgap Fibre into Optoelectronic Oscillator

6.1 Background

Chapters 2 to 4 provided the background of OEO technology and HC-PBGF technology and showed that HC-PBGF delay-lines can be used in OEOs to suppress temperature induced frequency drifts and to improve the long-term stability. In fact, the possibility of using HC-PBGFs in OEOs to improve the thermal stability has been discussed in the literature before [17]–[19]. However the reported experimental demonstrations have been done using only tens of meters of HC-PBGFs. Furthermore the insertion losses of the HC-PBGFs in ref. [17] and ref. [19] were as high as 2 dB/m. It should be noted that tens of meters long delay-lines are not enough to generate OEO signals that can compete with signals generated by commercial microwave signal generators in terms of spectral purity (>100s of metres long delay-lines are used in OEOs general). To the best of my knowledge, long-term stability of an OEO that uses a long-length HC-PBGF (>100s of metres) as the delay-line has not been characterized before. In addition, even though ref. [19] reports on a phase noise measurement of -58 dBc/Hz at 10 kHz offset frequency in a 10 GHz OEO (measured phase noise spectrum is not shown), phase noise properties of an OEO with a long-length (>100s of metres) HC-PBGF delay-line have not been measured in detail so far, to the best of my knowledge.

In order to investigate the stability of OEOs that use long-length HC-PBGF delay-lines as the optical energy storage element, I built an OEO incorporating a >850 m long HC-PBGF and characterized its stability (both long-term and short-term). The experimental results are presented in this chapter. The temperature induced long-term frequency variations of the OEO are measured and compared with the frequency variations when an SMF delay-line with similar delay is used in the OEO. The phase noise properties of the OEO are also measured and compared with the phase noise properties when an SMF delay-line is used.

6.2 Experimental Setup and Subsystems

For this investigation, I built a 10 GHz single-loop OEO. Even though a majority of the OEO loop delay is induced by the optical fibre delay-line, a considerable amount of delay is also induced by the rest of the components (both optical and electrical components such as modulators, phase shifters, EDFA, RF amplifiers, etc.), patch-codes and cables in the loop (these components which

are shown inside the shaded area in Figure 6-8 will be referred to as ‘the other components in the OEO loop’ in the text). The delay induced by the other components in the OEO loop was calculated to be around 250 ns in the OEO used in the following experiments. In order to identify the absolute stability improvement that can be obtained by using HC-PBGF delay-lines in an OEO, the temperature sensitivity of the delay-line has to be measured while minimizing the frequency drifts caused by the other components in the OEO loop. The details of the experimental setup and the related subsystems that were built to make this measurement are explained below.

6.2.1 Delay-lines

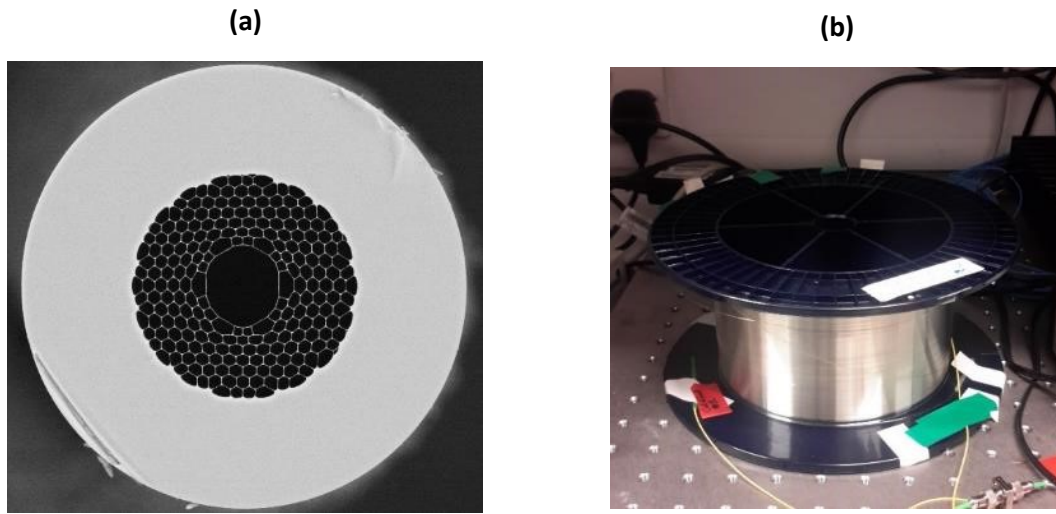


Figure 6-1 (a) Cross-sectional SEM image of the 860 m long 19-cell HC-PBGF used as the delay-line (the SEM image was provided by S. R. Sandoghchi) and (b) the 860 m long 19-cell HC-PBGF spooled on a 16 cm diameter spool.

An 860 m long HC-PBGF with a 19-cell core design was used as the delay-line. The HC-PBGF had a 29.5 μm core diameter and an 85.9 μm microstructure diameter (the fibre was provided by the Advanced fibre technologies & applications group, Optoelectronics research centre, University of Southampton). A cross-sectional scanning electron microscope (SEM) image of the fibre is shown in Figure 6-1a. The minimum loss of the HC-PBGF was slightly higher than 8 dB/km (at 1525 nm) and a measured insertion loss spectrum of the fibre is shown in Figure 6-2. The HC-PBGF was spooled on a standard 16 cm diameter spool (as shown in Figure 6-1b) and the two ends of the fibre were spliced with SMF pigtails with FC-APC connectors (splicing was done by T. D. Bradley). After splicing the pigtails, the total loss of the 860 m long HC-PBGF delay-line was 15 dB (at 1550 nm) and a PDL of ~ 0.75 dB was present. Mode field mismatch between SMF and HC-PBGF, and the distortion of the HC-PBGF microstructure due to heat can be identified as the main causes for the increase of insertion loss after the splicing of SMF pigtails [138], [139]. It should be noted that

improving the splicing between solid-core fibres and hollow-core fibres is a current topic of research in the scientific community and splicing methods that can reduce splice losses down to ~ 0.5 dB have been proposed [139].

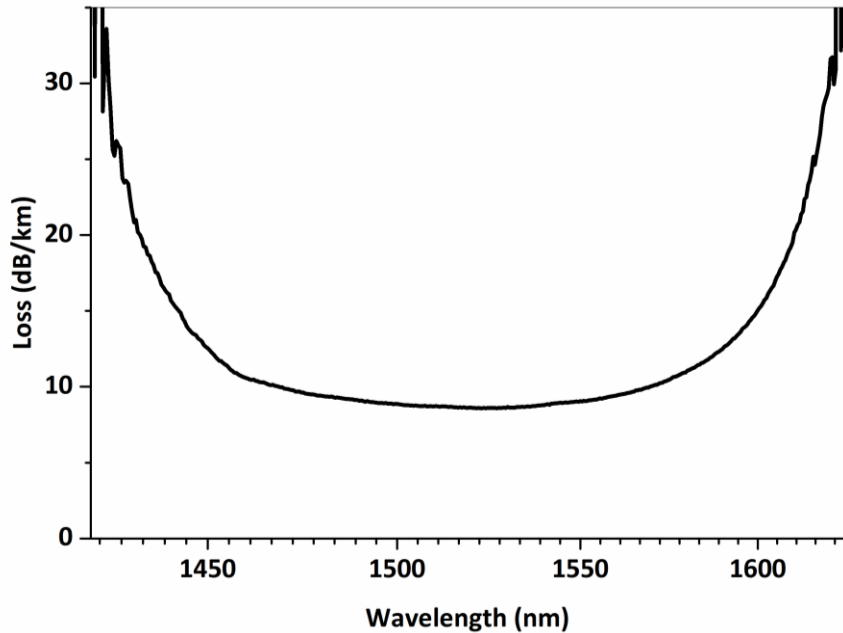


Figure 6-2 Insertion loss spectrum of the 860 m long HC-PBGF before splicing with SMF pigtales (provided by T. D. Bradley).

In order to compare the performance of the OEO with HC-PBGF, the experiments were repeated with an SMF delay-line in the OEO. The 860 m long HC-PBGF induced a delay of $2.88 \mu\text{s}$ ($n_g=1.003$ [15]). In order to obtain a delay of $2.88 \mu\text{s}$, 588 m long SMF is required (considering an n_g of 1.468). However the closest length of SMF available in the laboratory was 500 m (Corning SMF-28+, n_g was 1.468 [62]). The 500 m SMF induced a slightly shorter delay of $2.45 \mu\text{s}$ and was also spooled on a standard 16 diameter spool. I used this fibre as the SMF delay-line in the experiments.

6.2.2 Custom EDFA

Due to the insertion loss of the HC-PBGF delay-line, it was necessary to employ an EDFA in the OEO loop to make the OEO oscillate. However, as mentioned, minimizing the ambient temperature induced loop delay changes caused by the other components in the OEO loop is important in these experiments. For most components in the OEO loop, this can be done by placing the components inside a polystyrene insulation box. However placing a commercial EDFA inside an insulation box with the other components is not practical due to its size, electrical parts of the EDFA that may generate heat and mechanical parts of the EDFA such as cooling fans that may introduce vibrations.

Chapter 6

Hence a simple custom EDFA was built. By using a simulation software (GainMasterTM) from Fibercore, UK, it could be calculated that a saturation output power of 19 dB can be obtained by using 10 m of M5/980/125 Erbium doped fibre (EDF). Using 10 m of this fibre and using a pump laser operating at 980 nm, an EDFA was built and the schematic diagram is shown in Figure 6-3. The components of the EDFA inside the shaded area (a photo of these components are shown in Figure 6-4) can be insulated conveniently.

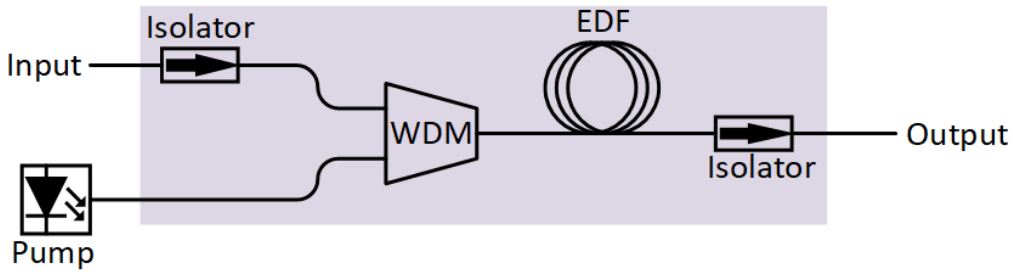


Figure 6-3 Schematic of the custom EDFA. WDM: Wavelength division multiplexer, EDF: Erbium doped fibre.

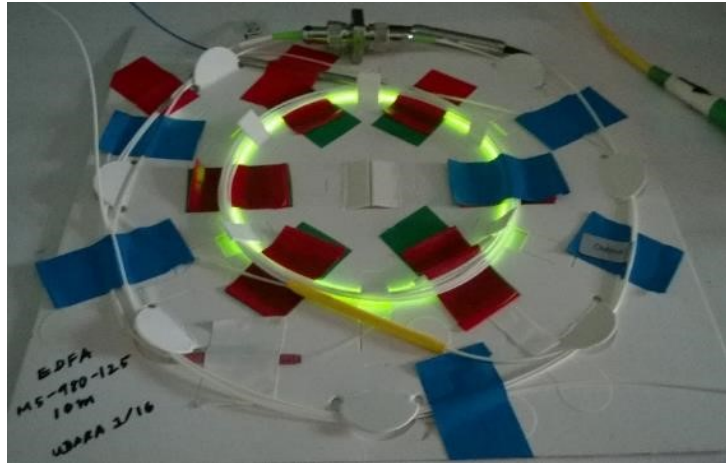


Figure 6-4 The section of the custom EDFA that can be thermally insulated.

6.2.3 Bias-point Locking of the Modulator

The OEO output signal frequency depends on the bias voltage applied to the MZM [47]. However the bias point of an MZM can drift due to temperature variations, photorefractive effect, etc. [140]. Hence it is necessary to minimize the frequency drifts caused by bias point drifts of the modulator. This can be done by implementing a feedback control to maintain a constant optical power at the modulator output [141].

The feedback control scheme incorporated into the OEO is shown inside the shaded area in Figure 6-5. In this scheme, the optical output power of the modulator is detected by a tap photodiode. Photodiode output is amplified by a custom built transimpedance amplifier. Due to the slow

response of the transimpedance amplifier, high-frequency components are cut off. The amplifier output is then fed into a locking unit (LB 1005 Servo Controller, Newport, USA) through a low-pass filter. Locking unit output is connected to the bias-port of the modulator to close the feedback control loop. After adjusting the locking unit to maximize the power of the OEO output signal (i.e. by biasing to the quadrature point) the feedback control scheme can be locked to maintain a constant optical power at the modulator output.

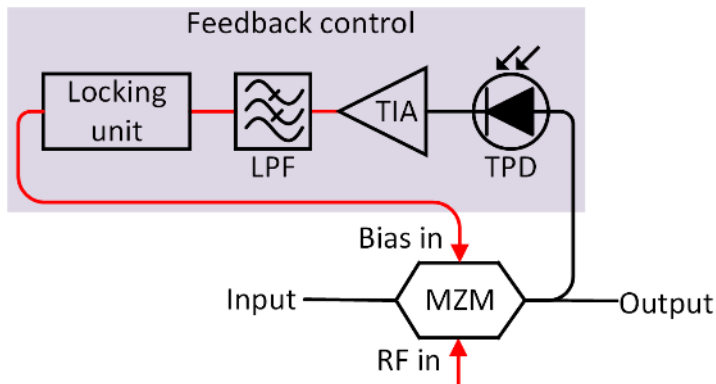


Figure 6-5 Schematic of the feedback control. TPD: Tap photodiode, TIA: Transimpedance amplifier, LPF: Low-pass filter, MZM, Mach-Zehnder modulator. Optical paths are shown in black and electrical paths are shown in red.

6.2.4 Thermal Chamber

The frequency drifts of the OEO due to temperature induced delay changes in the delay-line can be measured by changing the temperature of the delay-line between two levels and measuring the resulting frequency variation. This has to be done by placing the delay-line inside a thermal chamber and actively controlling its temperature.

6.2.4.1 Thermal Chamber with Single Heating Element

Initially I built an Arduino UNO microcontroller board [142] based temperature control system to control the temperature inside a polystyrene box. Temperature inside the box was obtained by measuring the voltage drop across a $10\text{ k}\Omega$ thermistor. An incandescent bulb was used as the heating element. Real-time temperature measurements were read by the microcontroller and the temperature inside the box was kept at pre-defined temperature levels for pre-defined time intervals by controlling the heating element via a relay circuit. In addition, real-time temperature readings were sent to the computer by the microcontroller and the temperature readings were recorded using a terminal program. Figure 6-6 shows the temperature variation inside the polystyrene box when the control system was set to vary the temperature between 30°C and 40°C with a 20 minutes settling time.

However this setup had some limitations. The system was capable of only heating (not cooling) and since there was only one heating element, the spool may not be heated from all sides evenly. Hence this setup was not used in the final experiments.

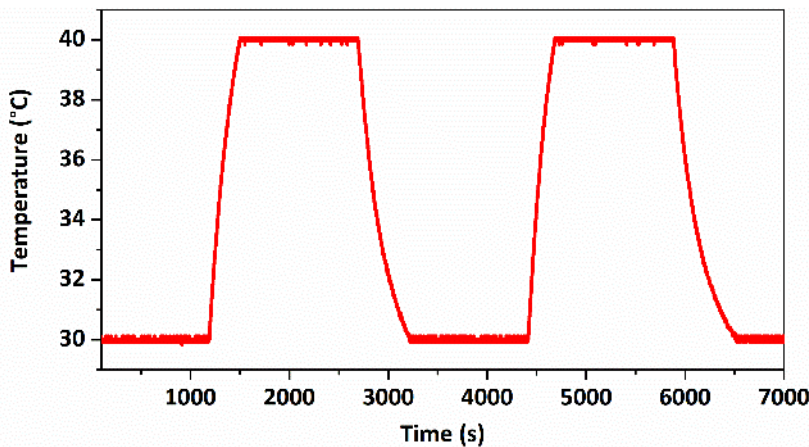


Figure 6-6 Temperature variation inside a polystyrene box when the Arduino UNO microcontroller board based temperature control system was set to vary temperature between 30°C and 40°C with a 20 minutes settling time.

6.2.4.2 Thermal Chamber with 10 Peltier Modules



Figure 6-7 (a) Outside look and (b) inside look of the thermal chamber with 10 Peltier modules.

I built a second temperature controller to overcome the limitations of the previously explained thermal chamber. For this, an octagonal shaped chamber was built from aluminium sheets with octagonal aluminium sheets for the top and the bottom. Nylon rods were attached to the bottom sheet as legs and the top sheet (the lid) is removable. In this thermal chamber, a Peltier module (37.9 W) is attached to every side of the chamber (10 modules all together). A heat sink is attached to every side of the chamber (as shown in Figure 6-7) so that the Peltier module is

sandwiched between the aluminium sheet and the heat sink. To drive the Peltier modules, they are assembled as follows: the 10 modules are divided into two sets of 5. The 5 Peltier modules in each set are connected in parallel. Then the two sets (each containing 5 Peltier modules) are connected in series.

This Peltier assembly is then driven as one unit using a temperature controller unit (PR-59 LairdTech, UK). Up to 3 thermistors can be connected to the temperature controller. Temperature controller can be connected to the computer and temperature control and temperature logging can be done by the software provided. This setup is capable of both heating and cooling the delay-lines and the heating/cooling can be done evenly from all sides. Hence I used this thermal chamber and the control system in the performed experiments. Two photos showing the outside and the inside look of the thermal chamber are shown in Figure 6-7. Even though the temperature controlling was done differently, I built this thermal chamber by following a thermal chamber designed by D. Gozzard and G. Marra and I thank them for providing the technical details. Furthermore R. Curtis (summer vacation student) added external insulation material to the thermal chamber.

6.2.5 The OEO Setup

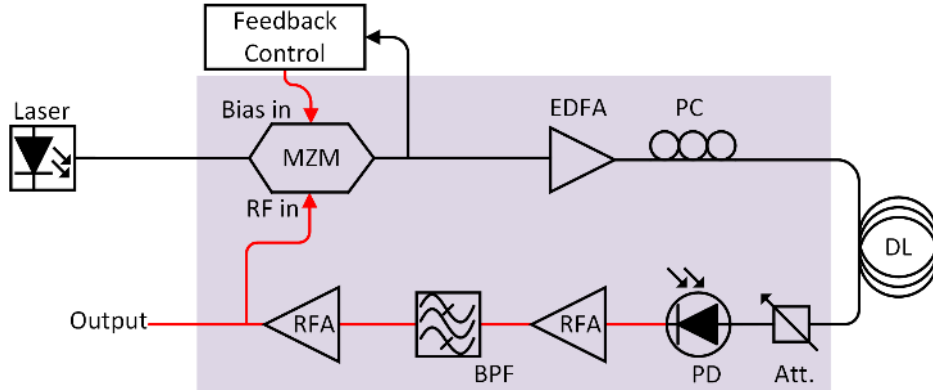


Figure 6-8 The 10 GHz single loop OEO setup. MZM: Mach-Zehnder modulator, EDFA: Erbium doped fibre amplifier, PC: Polarization controller, DL: Delay-line, Att.: Optical attenuator, PD: Photodiode, RFA: RF amplification, BPF: Band-pass filter. The components within the shaded area ('the other components in the OEO loop') can also induce frequency drifts due to temperature variations.

Optical paths are shown in black and electrical paths are shown in red.

The 10 GHz single loop OEO setup I built for this experiment is shown in Figure 6-8. The cw laser (from NP photonics Inc., USA with 18 dBm output power) operates at 1550 nm and the laser output is launched into a LiNbO₃ MZM. The modulator output is amplified by the custom built EDFA (detailed in section 6.2.2). EDFA output is launched into the delay-line and due to the slight

PDL of the HC-PBGF, a polarization controller had to be used between the EDFA and the delay-line. A photodiode at the output of the delay-line converts the optical signal into an electrical signal. In order to maintain the same optical power level at the photodiode when the two delay-lines are used, an optical attenuator is used before the photodiode (3 dBm optical power was maintained at the photodiode during phase noise measurements). The electrical signal of photodiode is amplified by a low-noise RF amplifier (with 17 dB gain) and filtered by a 10 GHz band-pass filter (with a 3 dB bandwidth of 8 MHz). The filtered electrical signal is re-amplified by a high power RF amplifier (with a 37 dB gain). The re-amplified signal is split into two; one part is fed back into the RF port of the OEO and the other part is used as the OEO output. The feedback control (detailed in 6.2.3) is used to keep the bias point of the MZM at quadrature.

6.3 Frequency Drift Measurements

After implementing the experimental setup (and the sub systems), I carried out a series of long-term frequency stability measurements. Some measurements were performed under ambient temperature variations to understand the general performance and the limitations of the OEO. The final experiment was done by placing the delay-lines in the thermal chamber. The frequency drifts were measured using the setup explained in section 3.2.1 with a 9.95 GHz reference signal.

6.3.1 Frequency Drift Due to All the Components of the OEO Loop

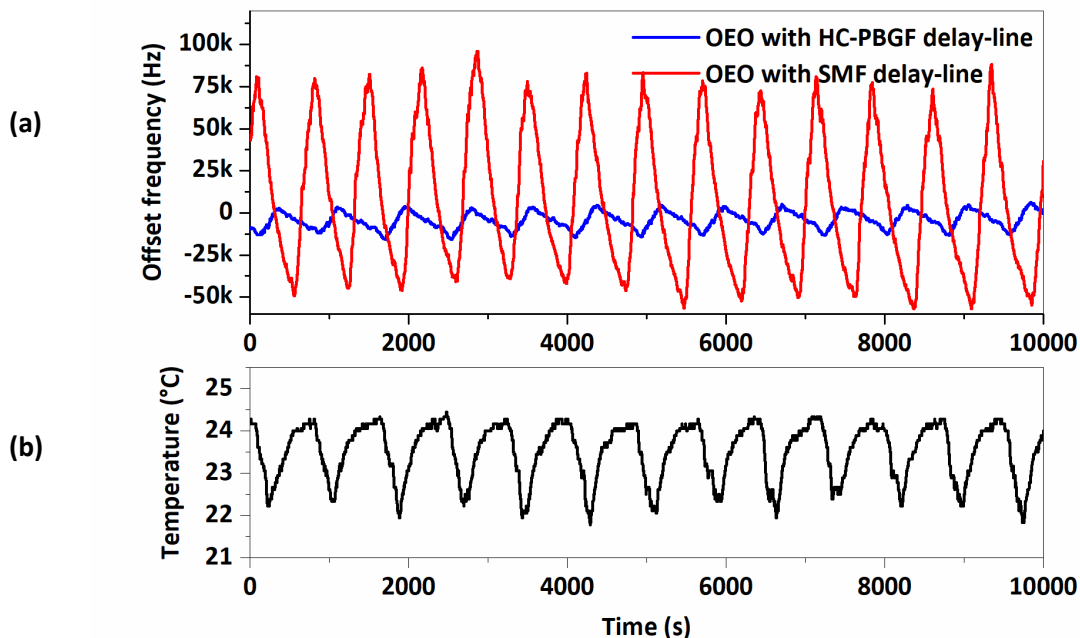


Figure 6-9 (a) Frequency drift of the OEO with HC-PBGF delay-line and with SMF delay-line when the entire OEO setup was exposed to ambient temperature variations and (b) ambient temperature variation in the laboratory.

In the first experiment, the entire OEO setup (shown in Figure 6-8) was exposed to ambient temperature variations. In this case frequency drifts are caused by temperature induced delay changes in all the components of the OEO loop (delay-line plus the other components in the OEO loop). As shown in Figure 6-9b, due to the switching on and off of the air-conditioning unit, a periodic temperature variation of $\sim 2^\circ\text{C}$ was present in the laboratory (temperature was measured by using a $10\text{ k}\Omega$ thermistor connected to an Arduino UNO microcontroller board). The frequency drifts of the OEO with the HC-PBGF delay-line and with the SMF delay-line under this ambient temperature change are shown in Figure 6-9a. On average, the frequency drift was 120 kHz with the SMF delay-line and 18 kHz with the HC-PBGF. The frequency drift of the OEO with the HC-PBGF delay-line is 6.7 times lower than that with the SMF delay-line. This preliminary result suggests that a significant improvement of stability can be obtained by using HC-PBGF delay-lines when the entire OEO setup is affected by ambient temperature variations. The Allan deviations corresponding to these frequency drifts are shown in Figure 6-10 and a clear overall improvement in long-term frequency stability can be seen when HC-PBGF delay-line is used. The hump between 100 s and 1000 s sampling times corresponds to switching on and off of the laboratory air-conditioner unit.

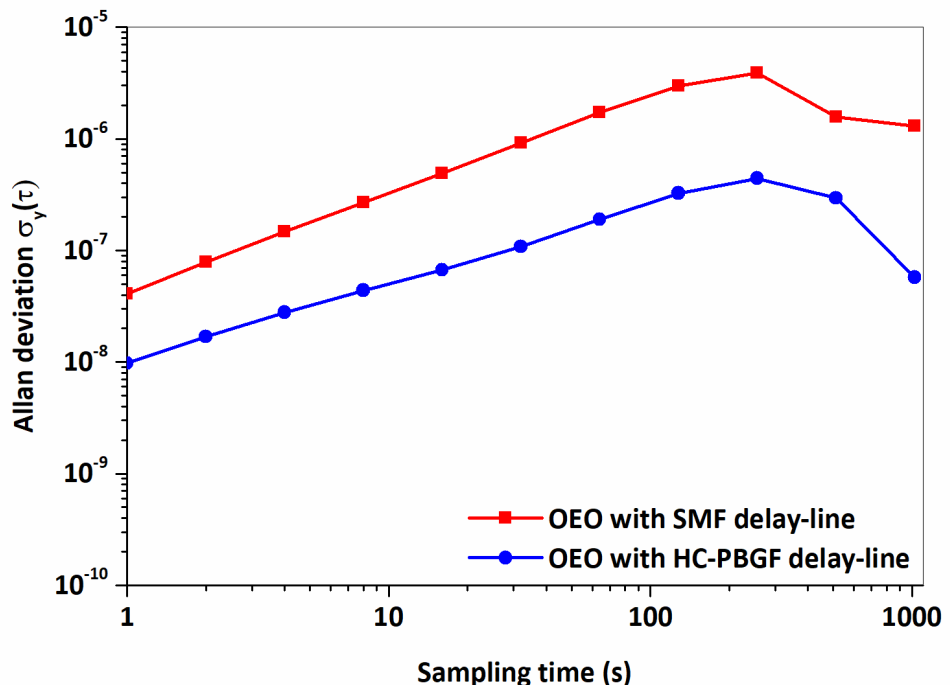


Figure 6-10 Allan deviations of the OEO with HC-PBGF delay-line and with SMF delay-line when the entire OEO setup was exposed to ambient temperature variations.

6.3.2 Frequency Drift Due to the Components in the OEO Loop Other Than the Delay-line

As shown in Figure 6-11, in this experiment, all the OEO components except the delay-lines were exposed to ambient temperature variations. The delay-lines were placed inside an insulation box to shield from ambient temperature variations so that frequency drifts due to delay changes in delay-lines are minimum (the averaged temperature variation inside an insulation box is shown in Figure 6-12b). The frequency variations in this case are mainly caused by temperature induced delay changes in the other components in the OEO loop.

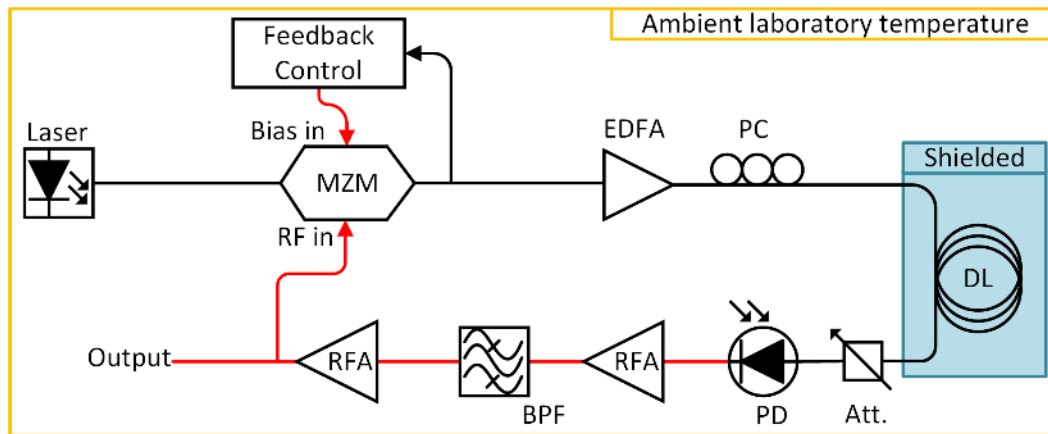


Figure 6-11 All the components of the OEO except the delay-line are exposed to ambient temperature variations. MZM: Mach-Zehnder modulator, EDFA: Erbium doped fibre amplifier, PC: Polarization controller, DL: Delay-line, Att.: Optical attenuator, PD: Photodiode, RFA: RF amplification, BPF: Band-pass filter. Optical paths are shown in black and electrical paths are shown in red.

The frequency drifts of the OEO with the SMF delay-line and with the HC-PBGF delay-line are shown in Figure 6-12a. The average frequency drifts of the OEO with SMF delay-line and with HC-PBGF delay-line were 6.5 kHz and 6 kHz respectively. Since the effect of the delay-lines are minimized (so that the frequency drifts are mainly caused by the other components in the OEO loop) the frequency drifts are similar. The slightly higher drift of ~ 0.5 kHz is in the case of SMF delay-line can be due to the slight temperature variations ($<0.1^\circ\text{C}$) inside the insulation box caused by the ambient temperature fluctuations. According to Figure 6-12b, the temperature variation inside the insulation box, measured by using a $10\text{ k}\Omega$ thermistor connected to an Arduino UNO microcontroller board looks constant. However due to the limited resolution (10-bit) of the analogue-to-digital converter (ADC) of the microcontroller, temperature variations of $<0.1^\circ\text{C}$ cannot be expected to be accurately measured using the Arduino UNO microcontroller board.

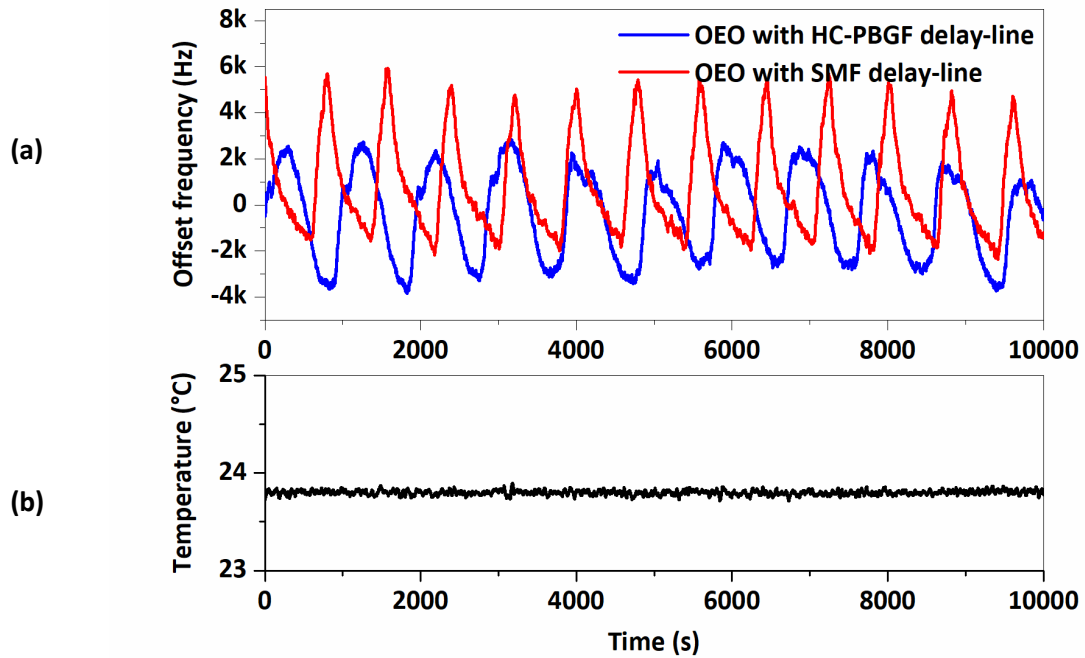


Figure 6-12 (a) Frequency drift of the OEO with HC-PBGF delay-line and with SMF delay-line when all the components of the OEO except the delay-line were exposed to ambient temperature variations and (b) averaged temperature variation inside the insulation box the delay-lines were placed in.

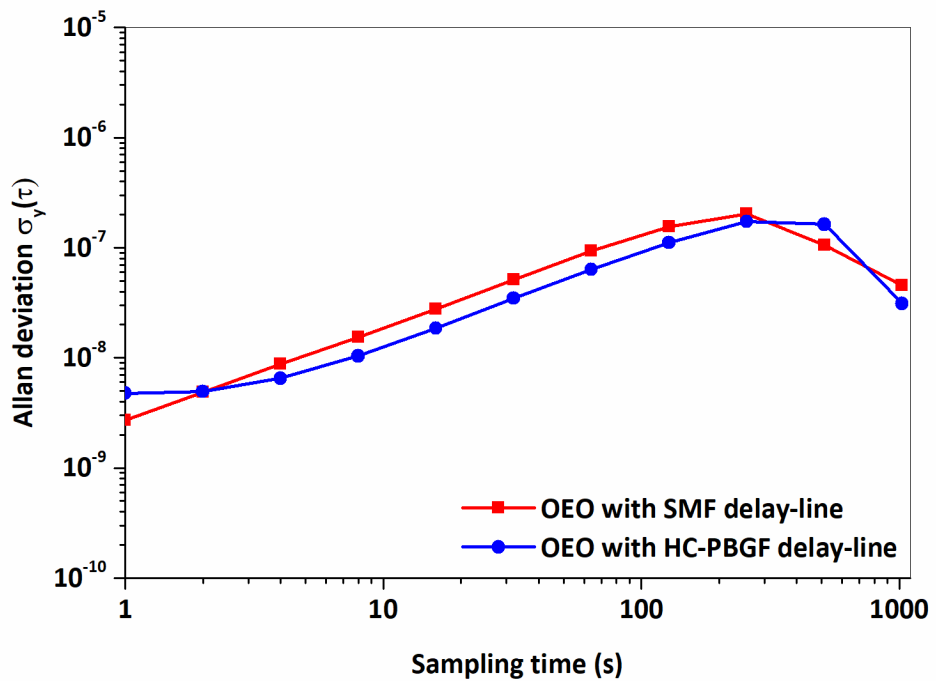


Figure 6-13 Allan deviations of the OEO with HC-PBGF delay-line and with SMF delay-line when all the components of the OEO except the delay-line were exposed to ambient temperature variations.

The Allan deviations corresponding to these frequency drifts are shown in Figure 6-13 and they closely follow each other indicating that once the effect of the delay-lines are excluded, the long-term frequency stability is governed by the same factors (i.e. the other components in the OEO loop). Humps (between 100 and 1000 sampling times) corresponding to the switching on and off of the air-conditioner unit can also be seen in the Allan deviations.

6.3.3 Minimum Frequency Drift of the OEO

In this experiment, all the components of the OEO loop were shielded from ambient temperature variations (as shown in Figure 6-14) to identify the best long-term frequency stability that can be achieved in the free running OEO with the HC-PBGF delay-line. The corresponding Allan deviation shown in Figure 6-15 is lower than the previous cases when the OEO was not fully shielded from ambient temperature variations. This level of stability (with Allan deviations of 1.3×10^{-9} at 1 s sampling time and 2.45×10^{-8} at 1000 s sampling time) is the best that could be obtained in this OEO setup with this HC-PBGF delay-line without any active temperature stabilization methods.

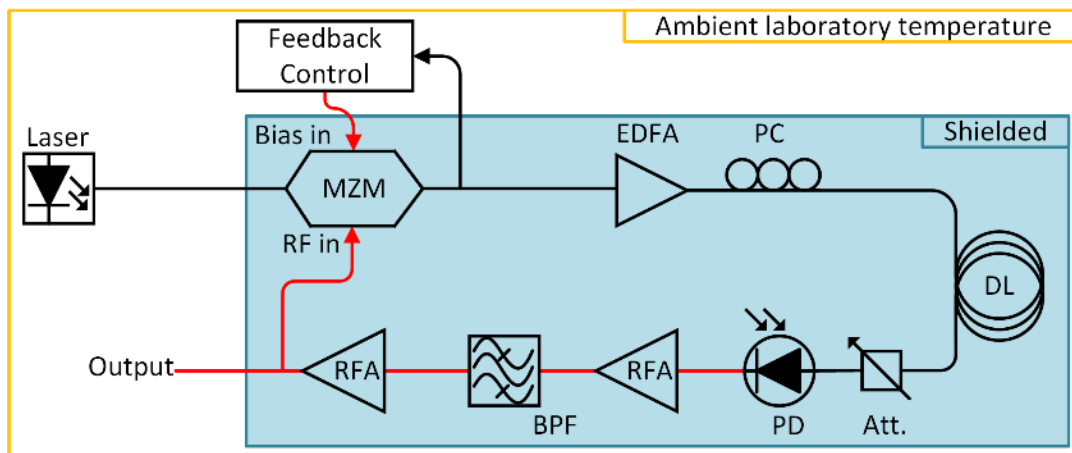


Figure 6-14 All the components of the OEO loop are shielded from ambient temperature variations. MZM: Mach-Zehnder modulator, EDFA: Erbium doped fibre amplifier, PC: Polarization controller, DL: Delay-line, Att.: Optical attenuator, PD: Photodiode, RFA: RF amplification, BPF: Band-pass filter.
Optical paths are shown in black and electrical paths are shown in red.

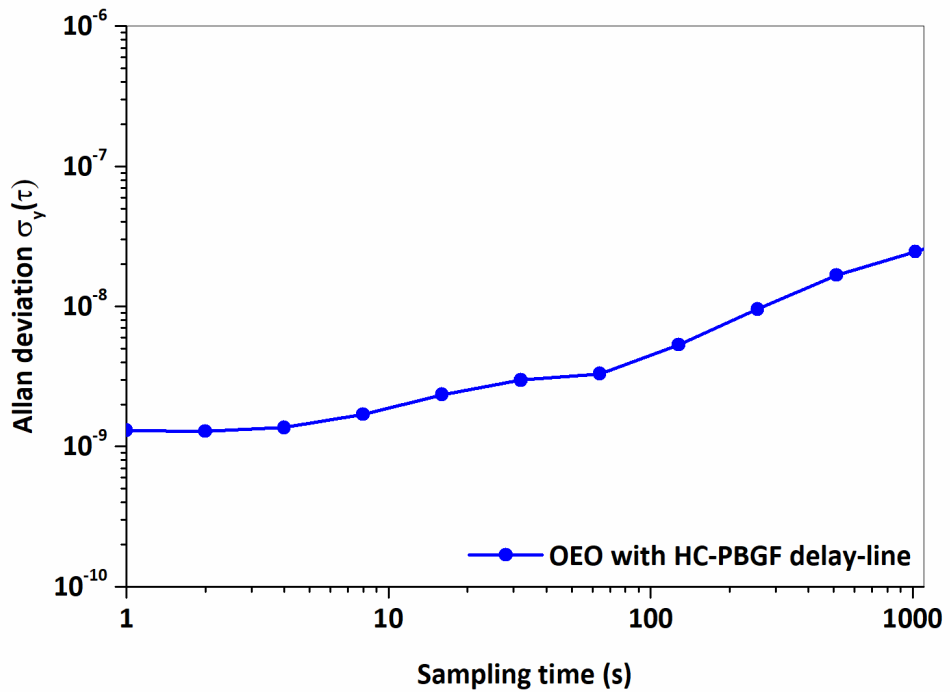


Figure 6-15 Allan deviation of the OEO with HC-PBGF delay-line when all the components of the OEO-loop were shielded from ambient temperature variations.

6.3.4 Absolute Long-term Frequency Stability Improvement with the HC-PBGF Delay-line

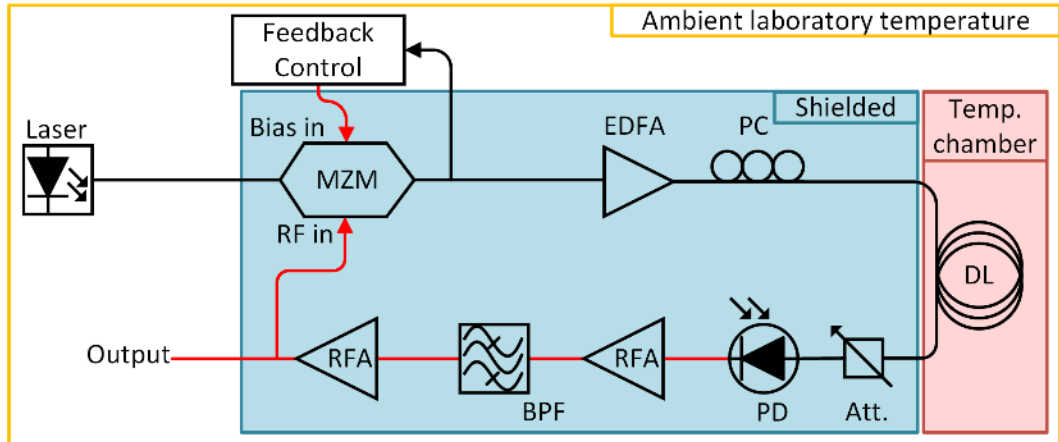


Figure 6-16 The delay-line is placed in the thermal chamber. The other components of the OEO loop are shielded from ambient temperature variations. MZM: Mach-Zehnder modulator, EDFA: Erbium doped fibre amplifier, PC: polarization controller, DL: delay-line, Att.: Optical attenuator, PD: photodiode, RFA: RF amplification, BPF: band-pass filter.

Optical paths are shown in black and electrical paths are shown in red.

In order to identify the absolute long-term frequency stability improvement (in terms of temperature induced frequency drifts) that can be achieved by using the HC-PBGFs as delay-lines in the OEO, the frequency variations induced by the delay-line have to be measured by changing

its temperature by a precisely known value while minimizing the frequency variations induced by the other components in the OEO loop. To do so, the delay-line was placed inside the thermal chamber (detailed in section 6.2.4.2, note: the top and the bottom Peltier modules were not operated in this experiment). The other components in the OEO loop were shielded from ambient temperature variations (see Figure 6-16).

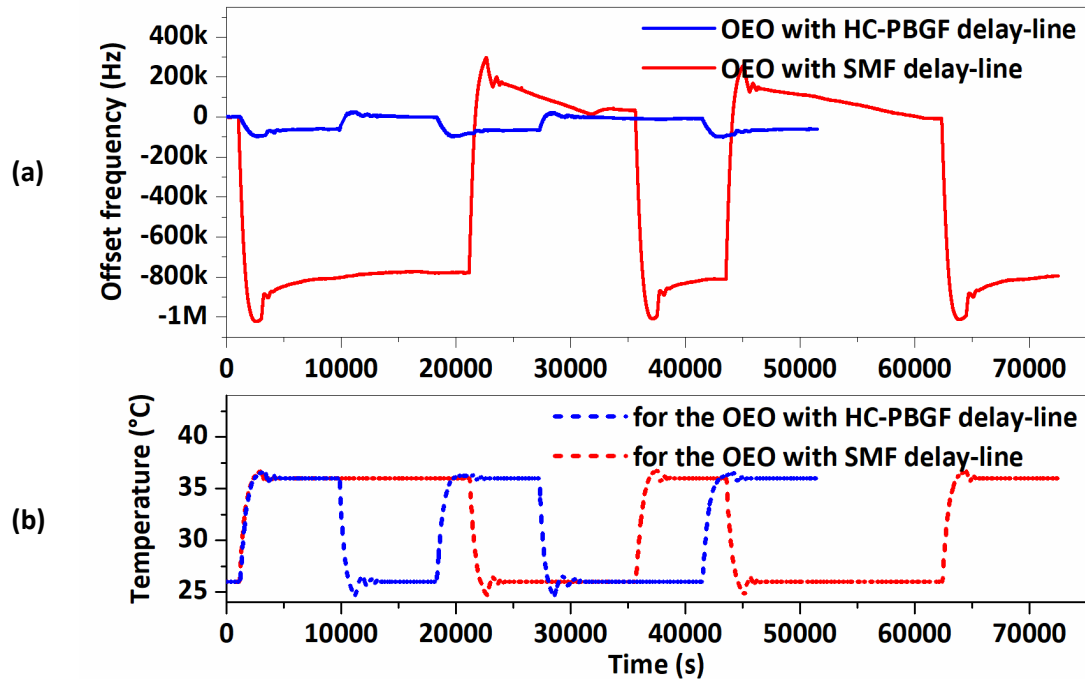


Figure 6-17 (a) Frequency drift of the OEO with HC-PBGF delay-line and with SMF delay-line when the delay-lines were inside the thermal chamber and the other components of the OEO loop were shielded from ambient temperature variations and (b) variation of temperature inside the thermal chamber for the two delay-lines.

The temperature inside the thermal chamber was varied between 26°C and 36°C while giving time for the delay-line to settle at the two temperature levels (as shown in Figure 6-17b). The frequency variations of the OEO for the 10°C temperature change in the delay-lines are shown in Figure 6-17a. The frequency change of the OEO with SMF delay-line was 810 kHz and the frequency change with the HC-PBGF delay-line was 60 kHz. As mentioned, the two delay-lines induced slightly different delays (2.88 μ s by HC-PBGF delay-line and 2.45 μ s by SMF delay-line). Hence to compare the frequency drift results and to identify the absolute stability improvement that can be obtained by replacing a standard SMF delay-line in an OEO with a HC-PBGF delay-line, I calculated the frequency drift per unit delay for the two delay-lines according to (note that frequency drift per unit length of the delay-line cannot be used for comparison because delay per unit length is not the same for the two delay-lines),

$$\text{frequency drift per unit delay} = \frac{\text{frequency drift}}{\text{total delay induced by the delay line}}. \quad 6-1$$

The frequency drift per unit delay was 331 GHz/s for the SMF delay-line and 21 GHz/s for the HC-PBGF delay-line. According to these results, the OEO is 15.8 times less temperature sensitive with the HC-PBGF delay-line, or in other words, by replacing an SMF delay-line with a HC-PBGF delay-line of similar delay, 15.8 times frequency stability improvement, in terms of temperature induced frequency drifts can be obtained (provided that the frequency drifts due to the other components in the OEO is negligible).

6.4 TCD Calculations

Using the measured frequency drifts, the TCD of the delay-lines fibres can be calculated. If the OEO loop delay at a temperature level T_1 is τ_1 , with FSR_1 as the corresponding FSR, and OEO loop delay at the a temperature level T_2 is τ_2 , with FSR_2 as the corresponding FSR, the OEO loop delay change, $\Delta\tau$ can be written as,

$$\Delta\tau = \tau_2 - \tau_1 = \frac{1}{FSR_2} - \frac{1}{FSR_1} = \frac{FSR_1 - FSR_2}{FSR_1 FSR_2}. \quad 6-2$$

Substituting $\Delta FSR = FSR_1 - FSR_2$ and $FSR \approx FSR_1 \approx FSR_2$, $\Delta\tau$ can be written as,

$$\Delta\tau \approx \frac{\Delta FSR}{FSR^2}. \quad 6-3$$

The OEO output signal frequency f_{osc} can be written in terms of FSR as,

$$f_{osc} = n FSR, \quad 6-4$$

and the OEO frequency drift f_{drift} can be written as,

$$f_{drift} = n \Delta FSR, \quad 6-5$$

where n is the mode number of the oscillating mode of the OEO. Temperature induced FSR and f_{osc} change in a ring resonator based OEO has been depicted in ref. [143]. Using equation 6-4 and equation 6-5, equation 6-3 can be re-written in terms of f_{osc} and f_{drift} according to,

$$\Delta\tau = \frac{f_{drift}}{f_{osc} FSR}. \quad 6-6$$

The TCD, i.e. the change of delay per unit length per unit temperature can be written as,

$$TCD = \frac{1}{\Delta TL} \left[\frac{f_{drift}}{f_{osc} FSR} \right], \quad 6-7$$

where ΔT is the temperature change and L is the length of the delay-line fibre.

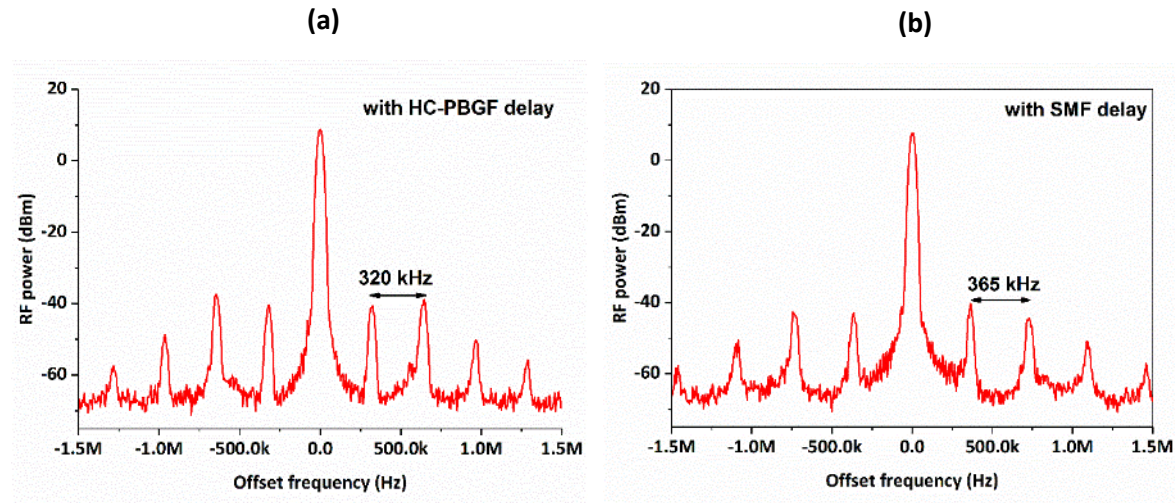


Figure 6-18 RF spectrum of the 10 GHz OEO output signal (a) with HC-PBGF delay-line and (b) with SMF delay-line (span=3MHz, RBW=27 kHz).

FSR of the OEO was obtained by measuring the frequency spacing between the spurious modes which were visible in the RF spectra of the OEO output signal (as shown in Figure 6-18). The measured FSRs of the OEO with the SMF delay-line and with the HC-PBGF delay-line were 365 kHz and 320 kHz respectively. Substituting the measured frequency drifts, FSR values and f_{osc} ($=10$ GHz) into equation 6-7, TCDs of the delay-line fibres were calculated to be 2.2 ps/km/K for the HC-PBGF delay-line and 44.4 ps/km/K for the SMF delay-line. The calculated TCD of the HC-PBGF delay-line used in the experiments is 10% higher than the previously reported 2 ps/km/K in ref. [14]. The calculated TCD of the SMF delay-line is also around 10% higher than the 40 ps/km/K in previous reports [13], [70]. It is possible that the slightly higher TCDs of the delay-lines used in the experiments are caused by the thermal expansion of the spools the fibres were spooled on and/or the effects of the fibre coatings.

6.5 Phase Noise Measurements

In order to check how HC-PBGF delay-line affects the short term stability of the OEO, phase noise characteristics of the OEO was measured when the HC-PBGF delay-line was incorporated. For comparison, phase noise characteristics of the OEO with the SMF delay-line was also measured. Photonic-delay scheme (explained in section 3.1.3) was used to measure phase noise. As mentioned before, since the measurement sensitivity varies with the delay-line length in the photonic-delay phase noise measurement scheme, two phase noise spectra were obtained for each measurement using two delay-lines (1 km and a 5.2 km) in the phase noise measurement setup. The two spectra were stitched together at 30 kHz offset frequency to get the final phase

noise spectrum. The results are shown in Figure 6-19. The noise floor, measured by bypassing the delay-line in the phase noise measurement setup [58] is also shown.

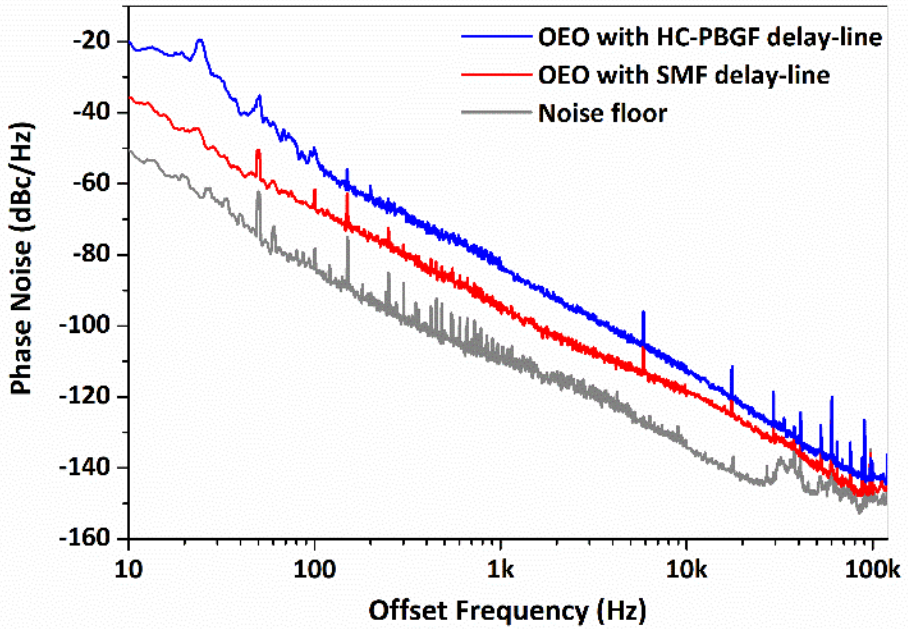


Figure 6-19 Phase noise spectra of the OEO with HC-PBGF delay-line and with SMF-delay-line.

It can be seen that as a whole, the phase noise of the OEO with the HC-PBGF delay-line is higher than that with the SMF delay-line. Between offset frequencies of 100 Hz and 2 kHz, the phase noise of the OEO with HC-PBGF is ~ 10 dB higher. Between 10 kHz and 100 kHz offset frequencies, the phase noise is < 3 dB higher. The increased phase noise in the OEO with HC-PBGF delay-line can be associated mainly with the intensity noise caused by multipath interference. Since HC-PBGFs are not purely single mode, the propagating light can get coupled into higher-order modes of the HC-PBGF and if this light gets coupled back into the fundamental mode (at the output or in the fibre), multipath interference can occur [144]. Furthermore multipath interference can occur due to reflections that occur at splice points between HC-PBGF and SMF (like in a Fabry-Perot cavity) [144]. Multipath interference can be reduced by improving light launch/exit conditions into/out of the fibre, e.g., by optimizing alignment [144] and making angle-cleaved splices between HC-PBGFs and SMFs [145]. However the effect of any residual multipath interference increases the intensity noise exiting the HC-PBGF [144]. This intensity noise gets converted into phase noise at the photodetectors and RF amplifiers in the OEO loop [146], degrading the spectral purity of the signal.

6.6 Conclusions

In this chapter I showed that long length (more than 850 m long) HC-PBGFs can be used in an OEO to achieve improved thermal stability. I built a 10 GHz single-loop OEO and using two different delay-lines in the OEO (one HC-PBGF and one SMF), measured the frequency drifts under different temperature conditions. When the whole OEO setup was exposed to ambient temperature fluctuations, the OEO with the HC-PBGF delay-line, showed 6.7 time reduction in frequency drifts compared to the OEO with the SMF delay-line.

By precisely varying the temperature of the delay-lines by a known value (10°C) and measuring the corresponding frequency variations of the OEO while minimizing the frequency variations caused by the other components of the OEO, it could be identified that a 15.8 times reduction in temperature induced frequency drifts can be achieved by replacing a standard SMF delay-line with a HC-PBGF delay-line of similar delay. This improvement can be attributed to the negligible temperature induced refractive index change in the air-core at constant volume [14], [16] of the HC-PBGF. The temperature induced delay change in the HC-PBGF delay-line in this case was mainly caused by the temperature induced fibre elongations.

TCD of the HC-PBGF and SMF delay-lines were calculated from the measured frequency drifts. The calculated TCD values showed $\sim 10\%$ increase compared to the previous reports [13], [14], [70] and this can be caused by the thermal expansion of the spools the fibres were spooled on and/or the effects of fibre coatings. Due to increased intensity noise caused by multipath interference, phase noise of the OEO with HC-PBGF delay-line was higher than that with the SMF delay-line.

Parts of the work presented in this chapter have been published [147], [148].

Chapter 7 Exploiting Zero-TCD Characteristics of Hollow-core Photonic Bandgap Fibres to Improve the Thermal Stability of Optoelectronic Oscillators

7.1 Introduction

In the previous chapter, I showed that a significant improvement (more than 15 times) in temperature stability can be achieved in an OEO by using HC-PBGF delay-lines. In that case, the (remaining) temperature sensitivity of the HC-PBGF was governed by the temperature induced elongations.

However as explained in Chapter 4, it has been suggested in literature [16]–[18] that temperature sensitivity of HC-PBGFs can be further reduced and even reach negative TCD values by making light propagate faster in the thermally elongated fibre [16]. Proof-of-concept measurements of zero and negative TCD values measured in a 2.8 m long HC-PBGF have also been reported [16]. However, many real-world applications that can be benefitted from fibres with near-zero or negative TCD characteristics (such as OEOs, fibre-optic gyroscopes, etc.) require long fibre lengths (>100 s of metres) and to the best of my knowledge, zero and negative TCD characteristics have not been demonstrated in long-length (>100 s of metres) HC-PBGFs.

In this chapter, near-zero and negative TCD characteristics of a long-length HC-PBGF, incorporated in a real-world application is investigated. The experiments are performed using a long-length (>1 km) HC-PBGF delay-line incorporated OEO. The measured TCD characteristics of the HC-PBGF delay-line at different operational wavelengths are presented. Phase noise characteristics of the OEO at two different operational wavelengths (when the TCD of the HC-PBGF is positive and negative) are also presented and compared with phase noise characteristics when an SMF delay-line is used in the OEO.

7.2 Determination of the suitability of the Fibre

It has been suggested in ref. [16] that the wavelength corresponding to 79 ps/nm/km in the chromatic dispersion profile of a HC-PBGF can be approximated to be the wavelength at which the HC-PBGF exhibits zero-TCD characteristics. Even though the exact zero-TCD wavelength can be slightly different, the experimental results presented in ref. [16] show that this approximation can be used to identify the wavelength region where zero-TCD wavelength lies. This means by

analysing the chromatic dispersion profile, the suitability of a HC-PBGF to be operated with zero-TCD in a practical application i.e., whether insertion loss of the fibre is acceptable at that wavelength, can be estimated in advance.

Hence the chromatic dispersion profiles of two HC-PBGFs that had suitable lengths to be used in an OEO were measured first. Chromatic dispersion profiles were obtained using the free-space Mach-Zehnder interferometric method described in ref. [16], using short sample lengths of the fibres (~ 3.5 m). In this method, the fibre sample is placed in one arm of the interferometer and by using a supercontinuum as the source, interference pattern is obtained. Using the peaks and troughs of the pattern, the spectral phase can be obtained. The derivative of spectral phase gives the delay through the fibre and derivative of the delay gives the chromatic dispersion. The experiments and data processing to obtain chromatic dispersion profiles were done by R. Slavík.

7.2.1 The 860-m Fibre

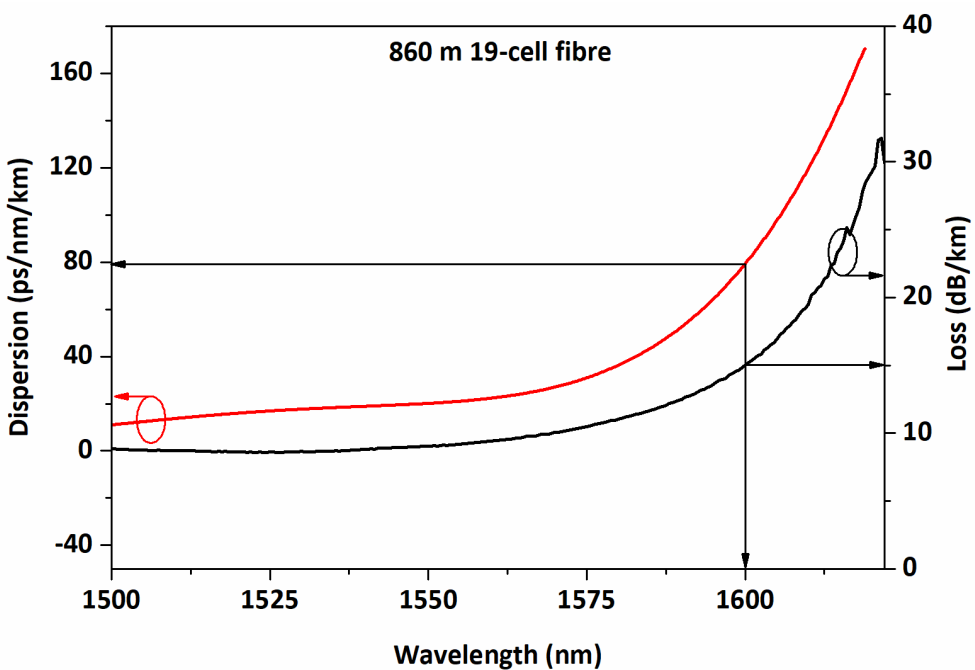


Figure 7-1 Chromatic dispersion profile of the 860-m fibre. The insertion loss of the fibre (before splicing SMF pigtails) over the same wavelength range is also shown.

This was the same 860 m long HC-PBGF which demonstrated a TCD of 2.2 ps/km/K at 1550 nm in the experiments in the previous chapter and its chromatic dispersion profile is shown in Figure 7-1 (this fibre will be referred to as the 860-m fibre in the text). It can be seen that the zero-TCD point corresponding to 79 ps/nm/km for this fibre is at 1600 nm. The insertion loss spectrum of the fibre before splicing SMF pigtails (also shown in Figure 7-1, provided by T. D. Bradley) shows that the insertion loss of this fibre at 1600 nm is 15 dB/km. With SMF pigtails, the insertion loss of the fibre at 1600 nm would increase to around 20 dB.

7.2.2 The 1090-m Fibre

The second HC-PBGF was a 1090 m long HC-PBGF with a 19-cell core design. The fibre core diameter was 31 μm and the micro-structure diameter was 91 μm . A cross sectional SEM image of the fibre is shown in Figure 7-2a (this fibre will be referred to as the 1090-m fibre in the text). This fibre was also provided by the Advanced fibre technologies & applications group, Optoelectronics research centre, University of Southampton.

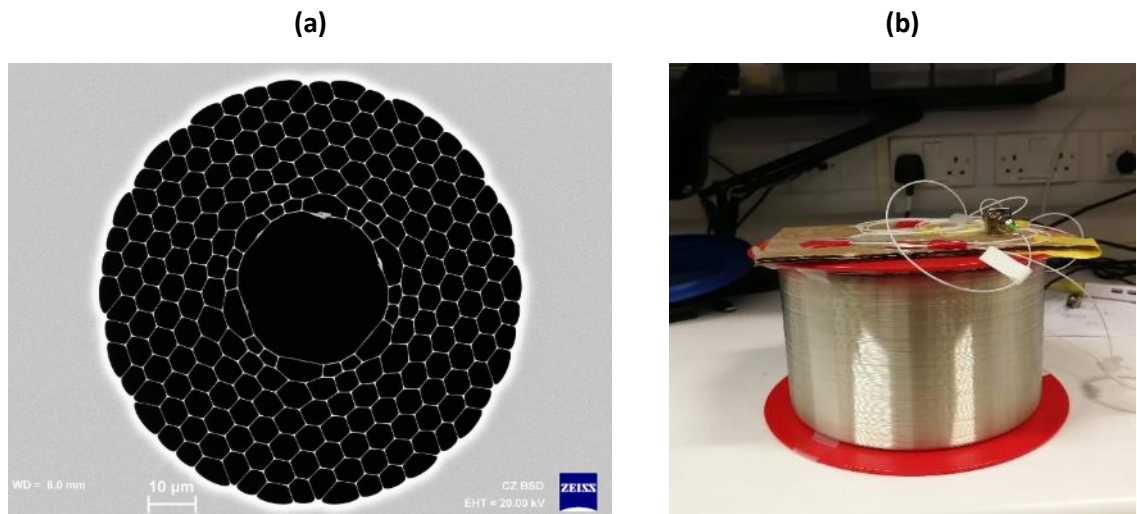


Figure 7-2 (a) Cross sectional SEM image of the 1090-m HC-PBGF used as the delay-line (the SEM image was provided by S. R. Sandoghchi) and (b) the 1090-m HC-PBGF spooled on a 16 cm diameter spool.

Figure 7-3 shows the chromatic dispersion and the insertion loss profiles of the fibre (the full insertion loss profile, provided by Y. Chen, is shown in Figure 7-4). The simulated chromatic dispersion profile of the fibre was provided by E. Numkam Fokoua and is shown by the grey-line (this simulated chromatic dispersion profile had been obtained by constructing the fibre profile using a cross-sectional SEM image of the fibre and then performing finite element calculations). According to The simulated chromatic dispersion profile, 79 ps/nm/km corresponding to zero-TCD occurs at 1603 nm where the insertion loss is 7.8 dB/km. The measured chromatic dispersion profile of the fibre is shown by the red-line in Figure 7-3. The measured profile suggests that 79 ps/nm/km occurs at 1607 nm where the insertion loss is 8.6 dB/km. When compared to the 860-m fibre, it can be seen that the zero-TCD operation of the 1090-m fibre can be expected to occur at a slightly longer wavelength. However the insertion loss of 1090-m fibre is significantly lower near the expected zero-TCD wavelength. Furthermore, since it is possible to further reduce the splice losses between HC-PBGF and SMF pigtailed than those incurred in the case of the 860-m fibre (which was around 4 dB per splice) and the fibre is also 27% longer, it was decided to use this fibre as the delay-line in the OEO to investigated the near-zero TCD characteristics of HC-PBGFs. The splicing of SMF pigtailed to the fibre was done by T. D Bradley and splice losses were <1 dB per

splice (significantly better than the 860-m fibre) and the insertion loss at 1607 nm was <11 dB. The PDL of the fibre was ~ 0.3 dB and as shown in Figure 7-2b, the fibre was spooled on a 16 cm diameter spool.

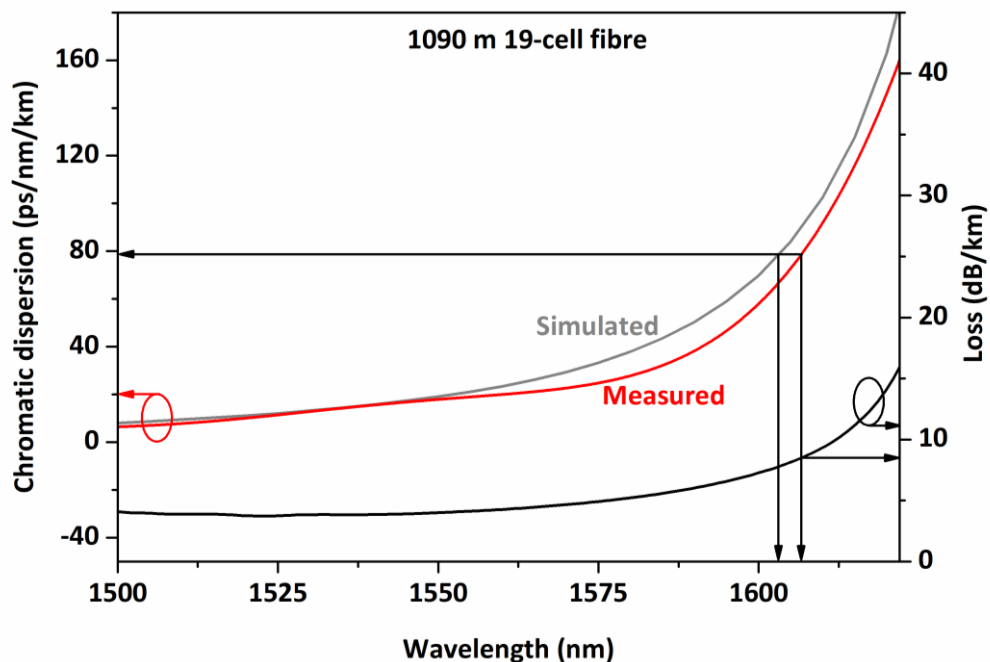


Figure 7-3 Simulated and measured chromatic dispersion profile of the 1090-m fibre. The insertion loss of the fibre (before splicing SMF pigtails) over the same wavelength range is also shown.

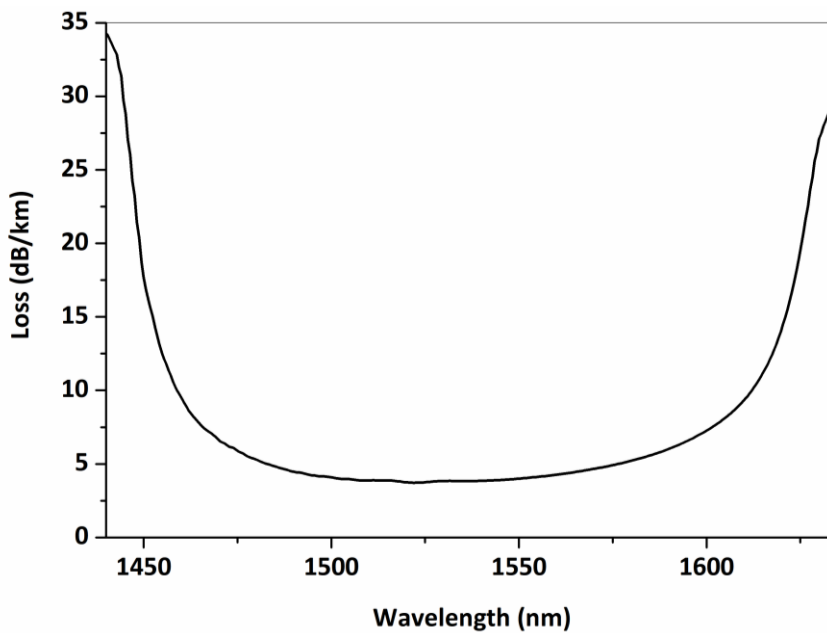


Figure 7-4 Insertion loss spectrum of the 1090-m fibre (provided by Y. Chen)

7.3 The OEO Setup

For this experiment, I built a 10 GHz single-loop OEO with a wavelength tuneable cw laser (from Agilent Technologies Inc., USA) as the light source (see Figure 7-5). The wavelength of the laser is tuneable between 1520 and 1630 nm and the laser output is launched into LiNbO_3 MZM. MZM output is launched into the delay-line (1090-m fibre) and due to the slight PDL of the HC-PBGF delay-line, a polarization controller is used before the delay-line. A photodiode connected to the output of the delay-line converts the optical signal into an electrical signal. Since the insertion loss of the delay-line is wavelength dependent, an optical attenuator is used between the delay-line and the photodiode to maintain a constant optical power at the photodiode (-6 dBm optical power was maintained at the photodiode during phase noise measurements). The electrical signal at the photodiode output is amplified by an ultra-low noise amplifier (with 14 dB gain) and a low noise amplifier (with 17 dB gain). The amplified signal is filtered by a 10 GHz band-pass filter with a 3 dB bandwidth of 8 MHz. The filtered signal is re-amplified by a low-noise amplifier (with 17 dB gain) and a high-power amplifier (with 37 dB gain). The re-amplified electrical signal is split into two; one part is fed back to the MZM to close the OEO loop and the other part serves as the output. The feedback control (explained in section 6.2.3) is used to maintain the bias point of the MZM at quadrature. Not using an EDFA and using more RF amplification are the main differences of this OEO setup compared to the one implemented in the previous chapter.

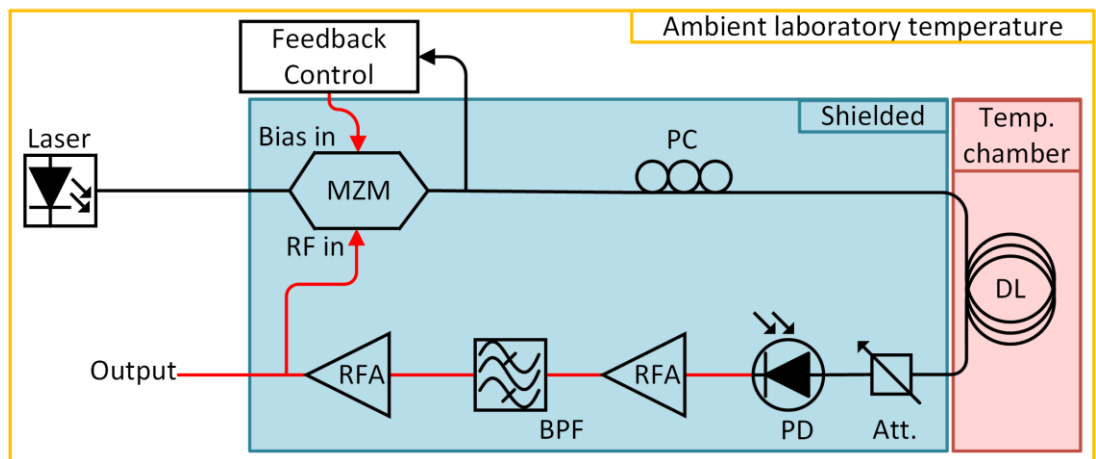


Figure 7-5 The 10 GHz single loop OEO setup. MZM: Mach-Zehnder modulator, PC: Polarization controller, DL: Delay-line, Att.: Optical attenuator, PD: Photodiode, RFA: RF amplification, BPF: Band-pass filter. The components within the blue area ('the other components in the OEO loop') are shielded from ambient temperature variations and the delay-line is placed inside the thermal chamber. Optical paths are shown in black and electrical paths are shown in red.

7.4 Chromatic Dispersion Measurement from the OEO

Interestingly, it can be seen that the OEO setup itself offers a method of measuring the chromatic dispersion of the fibre used as the delay-line (to the best my knowledge, this method of measuring chromatic dispersion using an OEO setup has not been demonstrated before). When the operating wavelength of the laser in the OEO is varied, the delay through the delay-line fibre also changes due to chromatic dispersion. This delay change changes the OEO loop delay and in turn the FSR of the OEO loop. When the delay change due to the other components of the OEO loop is minimum, by measuring the OEO output signal frequency drift and following the calculation in section 6.4, the delay change in the delay-line fibre can be calculated according to,

$$\Delta\tau = \tau_2 - \tau_1 = \frac{1}{FSR_2} - \frac{1}{FSR_1} \approx \frac{\Delta FSR}{FSR^2} = \frac{f_{drift}}{f_{osc} FSR}, \quad 7-1$$

where τ_1 and τ_2 are OEO loop delays at two different wavelengths, FSR_1 and FSR_2 are FSRs of the OEO at the two different wavelengths, f_{osc} is the OEO output signal frequency and f_{drift} is the change of OEO output signal frequency due to wavelength change. The FSR of the OEO was measured to be 260 kHz with the 1090-m HC-PBGF delay-line (see Figure 7-6). The chromatic dispersion, which is the change of delay per unit wavelength per unit length can be obtained by,

$$\text{Chromatic dispersion} = \frac{\Delta\tau}{\Delta\lambda L} = \frac{1}{\Delta\lambda L} \left[\frac{f_{drift}}{f_{osc} FSR} \right], \quad 7-2$$

where $\Delta\lambda$ is the change of operational wavelength of the laser and L is the length of fibre.

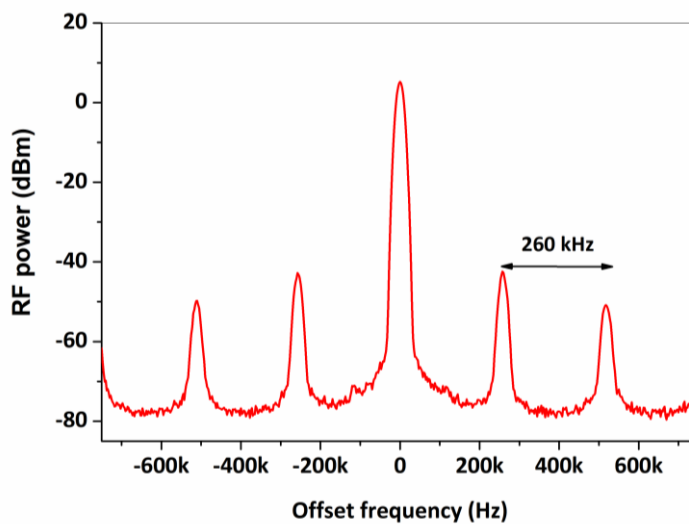


Figure 7-6 RF spectrum of the 10 GHz OEO output signal with 1090-m HC-PBGF delay-line at 1550 nm (span=1.5 MHz, RBW=15 kHz).

By slightly varying the operational wavelength (by less than 1 nm) of the OEO at discrete wavelengths between 1520 nm and 1616 nm, frequency changes of the OEO output signal were

measured. For example, when the wavelength was changed from 1569.5 nm to 1570 nm, the OEO output signal changed by 34 kHz (see Figure 7-7). Then by using equation 7-2, chromatic dispersion values were obtained. These results are shown in Figure 7-8 together with the chromatic dispersion measured with the free-space Mach-Zehnder interferometric method.

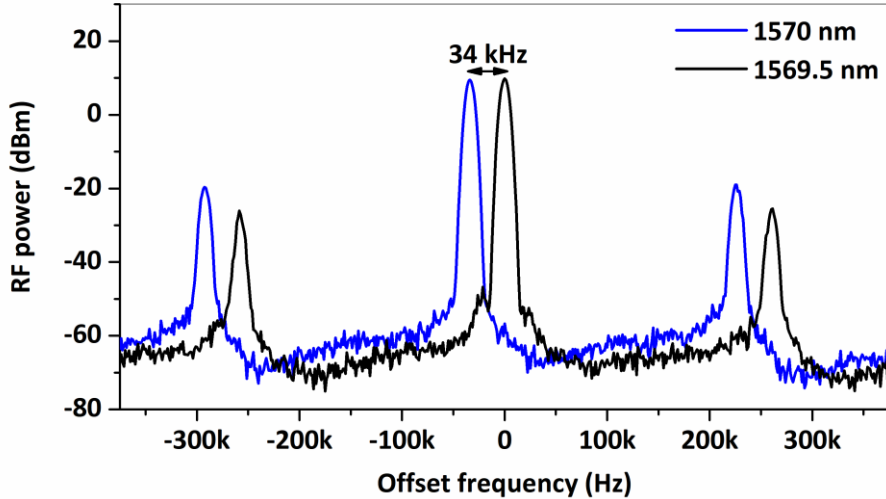


Figure 7-7 RF spectra showing the change of the 10 GHz OEO output signal when operational wavelength was changed from 1569.5 nm to 1570 nm (span=750 kHz, RBW=6.8 kHz)

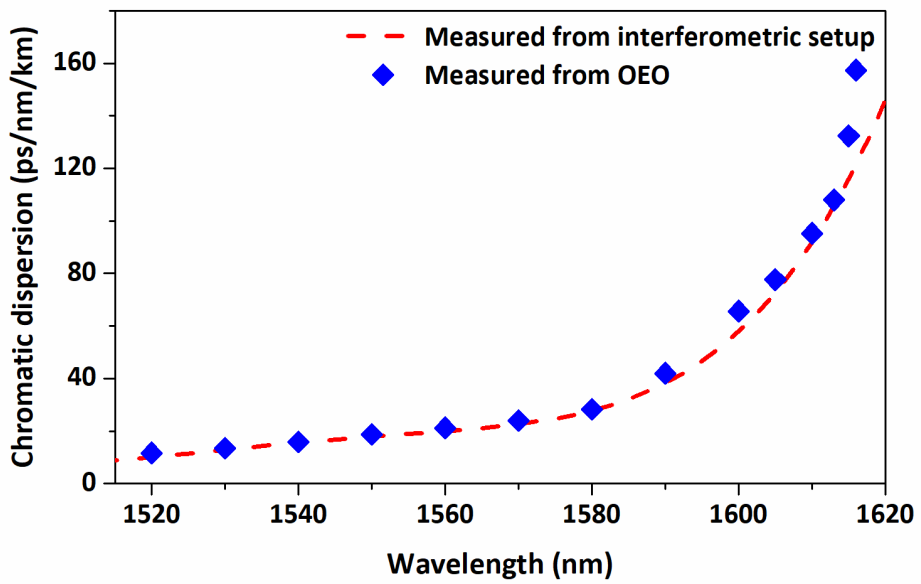


Figure 7-8 Chromatic dispersion of the 1090-m HC-PBGF delay-line measured by the change of OEO output signal. Chromatic dispersion measured by the free-space Mach-Zehnder interferometric setup is also shown.

The chromatic dispersion of the whole length of a fibre can differ from the chromatic dispersion measured on a short sample of the fibre due to structural variations along the fibre. However in

in this case, a good overlap of the two measured chromatic dispersion profiles (of the ~ 3.5 m sample and the whole length) can be seen. This suggests that the fibre has a good structural uniformity along the entire length.

7.5 Frequency Drift Measurements and TCD

As shown in Figure 7-5, the delay-line was placed inside the thermal chamber and the other components of the OEO loop were shielded from ambient temperature variations. The temperature inside the thermal chamber was varied from 55°C to 20°C (see Figure 7-9a) and the corresponding frequency drifts of the OEO were measured at different operational wavelengths between 1530 nm and 1615 nm. Frequency drifts were measured using the setup explained in section 3.2.1. In this case the mode spacing of the optical frequency comb was 249.3 MHz and hence the reference signal for frequency drift measurements was at 9.972 GHz ($= 40 \times 249.3$ MHz).

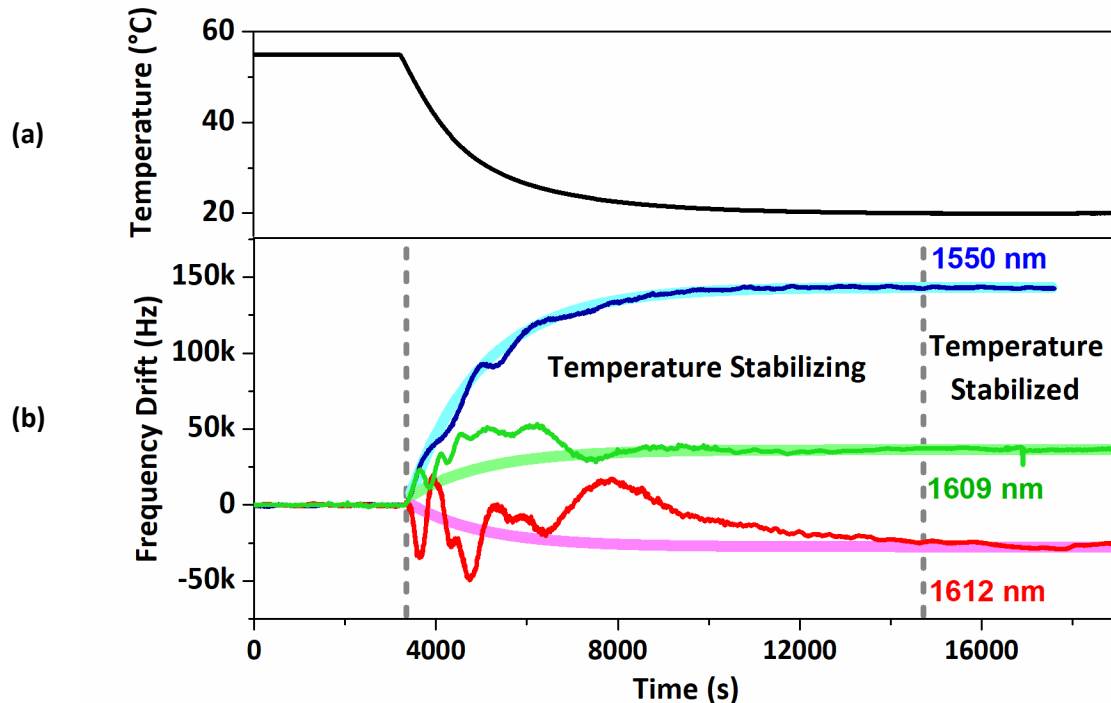


Figure 7-9 (a) The change of temperature inside the thermal chamber and (b) the corresponding frequency drifts of the OEO at 1550 nm, 1609 nm and 1612 nm.

As shown in Figure 7-9b, the frequency drift depends on the operational wavelength of the OEO and can be either positive or negative (i.e. the delay through the HC-PBGF can either decrease or increase with the temperature depending on the operational wavelength). The TCD values calculated using equation 6-7 for measured frequency drifts at different wavelengths are plotted in Figure 7-10 together with the predicted TCD variation of the fibre. The predicted TCD variation was provided by E. Numkam Fokoua and was obtained by evaluating the expressions given in ref.

[16], considering the fibre coating and using simulated chromatic dispersion profile of the 1090-m fibre. According to the experimental results, the TCD at 1609 nm is 0.37 ps/km/K and the TCD at 1612 nm is -0.28 ps/km/K and the zero-crossing occurs in between, at around 1610 nm. This is in good agreement with the predicted TCD variation. The frequency drift specifically at 1610 nm was not measured since any frequency drift due to the HC-PBGF is too small to be distinguished from the residual frequency drifts caused by the other components in the OEO loop. However the experimental results show that in the vicinity of the zero-TCD wavelength, there exists a >3 nm wide wavelength window where the TCD of the HC-PBGF delay-line is at least 100 times lower than that of an SMF delay-line.

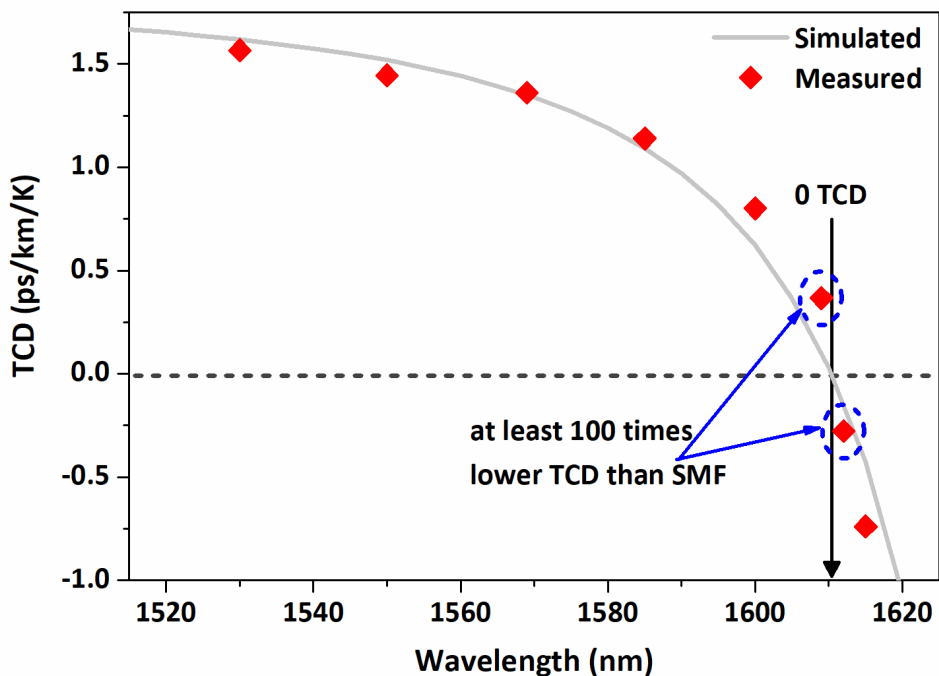


Figure 7-10 Measured TCD of the 1090-m HC-PBGF delay-line at different operational wavelengths from 1530 nm to 1615 nm. The predicted TCD variation is also shown.

7.6 Allan Deviation at 1610 nm

As a complementary measurement, I measured the Allan deviation of the OEO by stabilizing the delay-line at 26°C (by placing it inside the thermal chamber) while the rest of the OEO components are shielded from ambient temperature variations. The operational wavelength of the OEO was 1610 nm. The results are shown in by the blue-line Figure 7-11.

When compared with the minimum Allan deviation of the OEO with 860-m fibre measured at 1550 nm (shown in the previous chapter and also shown by the grey-line in Figure 7-11), when the fibre and the other components in the OEO loop were passively stabilized, it can be seen that the Allan deviation between 10 and 100 s sampling times is similar suggesting that the frequency

stability in that region is dominated by the residual frequency drifts of the other components in the OEO loop. However the at 1 s sampling time, Allan deviation of the OEO with 1090-m fibre is 2.7 times lower and at 1000 s sampling time, the Allan deviation is 3.6 times lower compared to the OEO with 860-m fibre. This improvement of stability can be attributed to both the low (near-zero) TCD of the 1090-m fibre as well as the active temperature stabilization of the fibre.

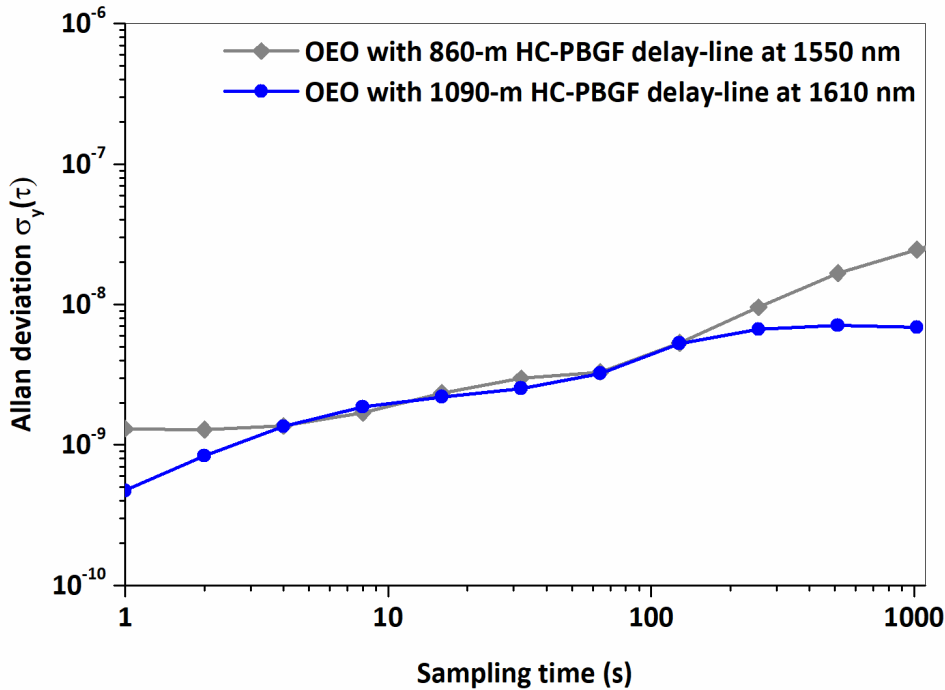


Figure 7-11 Allan deviation of the OEO at 1610 when the 1090-m HC-PBGF delay-line was stabilized at 26°C inside the thermal chamber while the other components of the OEO loop were shielded from ambient temperature variations (blue-line). Grey-line shows the previously shown minimum Allan deviation of the 860-m HC-PBGF delay-line incorporated OEO at 1550 nm.

7.7 Phase Noise Measurements

7.7.1 Without Frequency Modulation of the Laser

I measured the phase noise of the OEO with 1090-m fibre delay-line at two different wavelengths: at 1550 nm when the TCD of the delay-line is positive (1.45 ps/km/K) and at 1612 nm when the TCD of the delay-line is negative (-0.28 ps/km/K). For comparison, the phase noise of the OEO was also measured by incorporating a 700 m long SMF delay-line which induced a similar delay of 3.43 μ s to that of the 1090-m HC-PBGF fibre delay-line. The optical attenuator of the OEO was adjusted to maintain a constant optical power of -6 dBm at the photodiode of the OEO for both delay lines at the two different wavelengths. Phase noise was measured using the photonic-delay scheme

(explained in section 3.1.3). Similar to the previous phase noise measurements, for each measurement, phase noise spectra were obtained using two delay-lines (5.2 km and 1 km) in the phase noise measurement setup and the two spectra were stitched together (at 26.5 kHz offset frequency) to get the final phase noise spectrum. Furthermore, the noise floor was obtained by bypassing the delay-line in the phase noise measurement setup.

The phase noise measurements of the OEO at 1550 nm and 1612 nm are shown in Figure 7-12 and Figure 7-13 respectively. It can be seen that with both HC-PBGF and SMF delay-lines, changing the operating wavelength does not change the phase noise characteristics significantly. However, the phase noise of the OEO with HC-PBGF delay-line is higher than that with the SMF delay-line. At 100 Hz offset frequency, phase noise is \sim 15 dB higher and at 1 kHz offset frequency, phase noise is \sim 13 dB higher. At higher offset frequencies (>15 kHz) phase noise characteristics of the OEO with the two delay-lines are similar. As discussed earlier, the increase of phase noise of the OEO with the HC-PBGF delay-line can be mainly attributed to the intensity noise caused by multipath interference in the HC-PBGF which gets converted into phase noise at photodetectors and RF amplifiers in the OEO [144], [146].

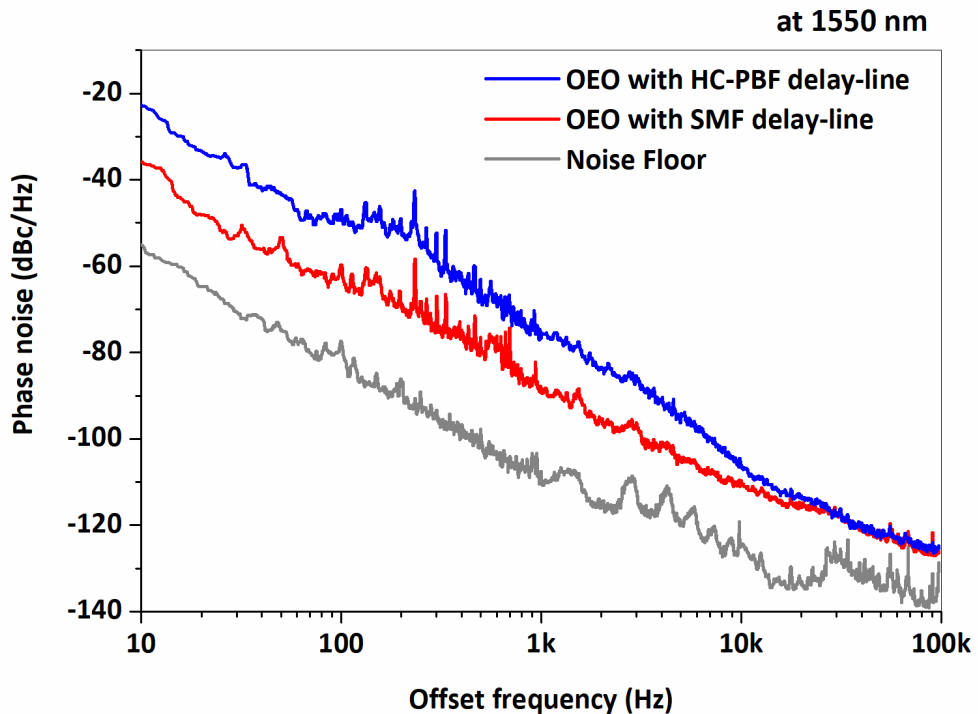


Figure 7-12 Phase noise spectra of the OEO with 1090-m HC-PBGF delay-line and 700 m SMF delay-line at 1550 nm (without laser frequency modulation).

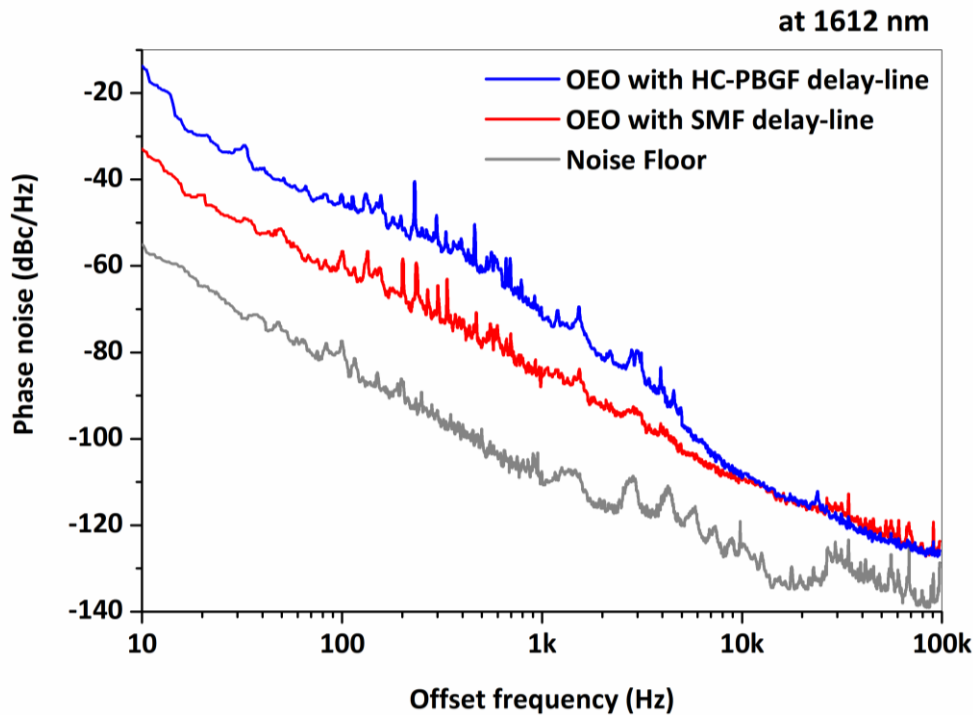


Figure 7-13 Phase noise spectra of the OEO with 1090-m HC-PBGF delay-line and 700 m SMF delay-line at 1612 nm (without laser frequency modulation).

7.7.2 With Frequency Modulation of the Laser

It has been shown that frequency modulation of the laser source can be used to suppress intensity noise caused by multipath interference in HC-PBGFs [144]. Furthermore frequency modulation of the laser source has also been used as a method of reducing phase noise in OEOs by suppressing the intensity noise caused by scattering and reflections in the fibre delay-lines [146], [149]. In these cases, frequency modulation suppresses noise by spreading noise power among the harmonic peaks of the modulation frequency [149].

Since it is the intensity noise that increases the phase noise when HC-PBGF delay-line is used in the OEO, I re-measured phase noise spectra of the OEO after turning on the in-built frequency modulation function ('coherence control') of the laser source. It should be noted that frequency modulation introduces peaks at the harmonics of modulation frequency, in the phase noise spectrum. As shown in Figure 7-14, in this case, the laser's frequency modulation function introduced peaks at harmonics of 977 Hz (and the modulation frequency was not tunable). Using a high modulation frequency (81 MHz modulation frequency has been used in ref. [144] to suppress intensity noise in a HC-PBGF) so that modulation harmonic peaks can be filtered by the RF band-pass filter in the OEO or using a pseudo-random modulation scheme [150] can be suggested as possible methods of reducing the effect of the harmonics of the modulation peaks.

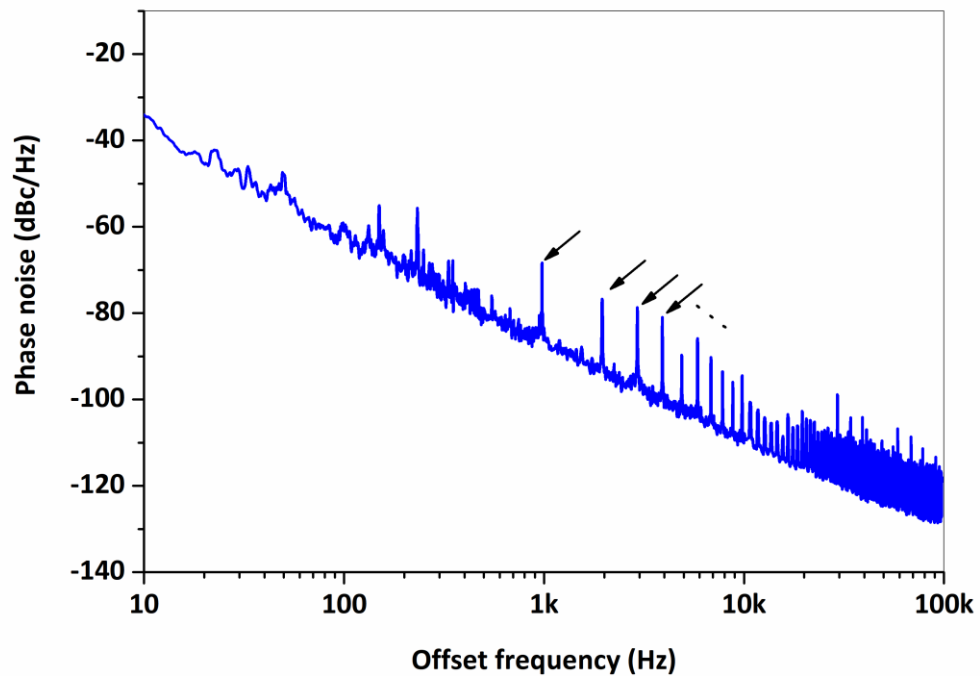


Figure 7-14 Phase noise spectrum with modulation harmonic peaks due to laser frequency modulation

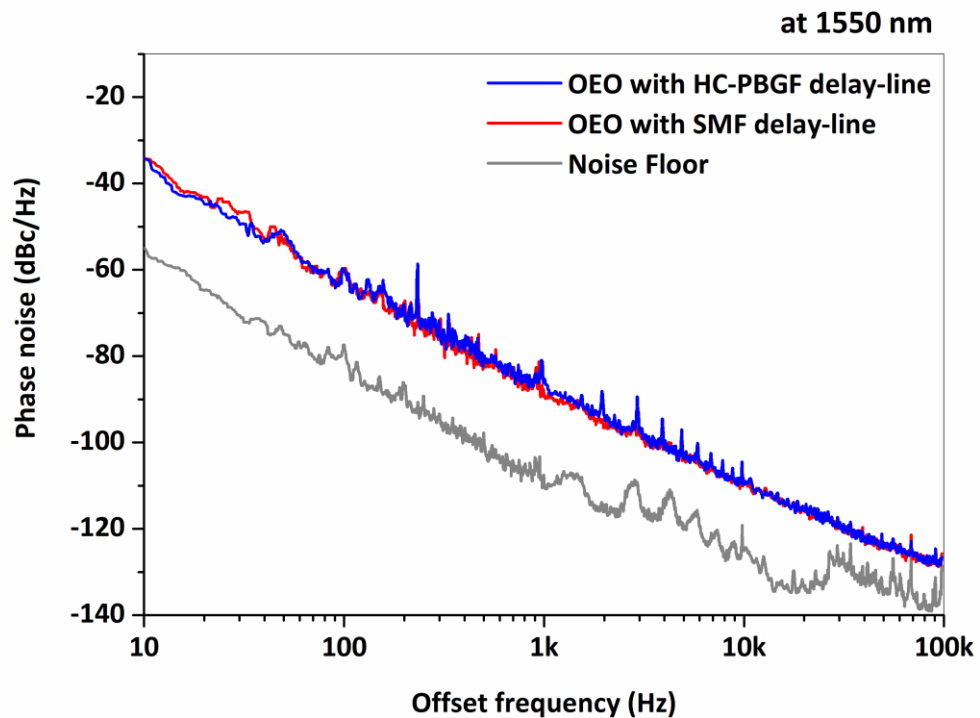


Figure 7-15 Phase noise spectra of the OEO with 1090-m HC-PBGF delay-line and 700-m SMF delay-line at 1550 nm (with laser frequency modulation).

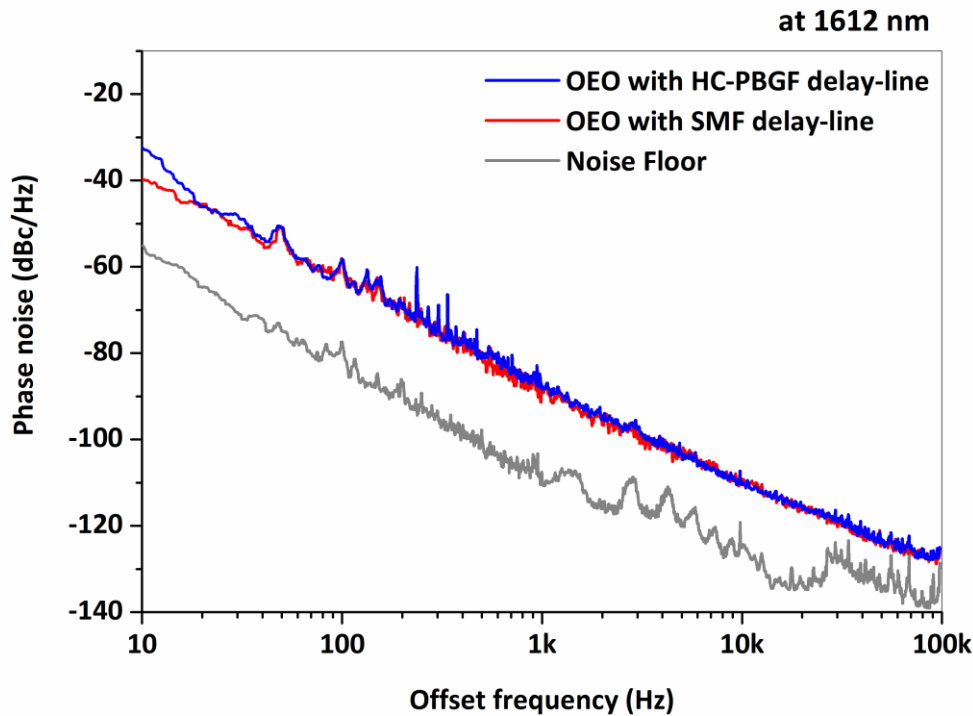


Figure 7-16 Phase noise spectra of the OEO with 1090-m HC-PBGF delay-line and 700-m SMF delay-line at 1612 nm (with laser frequency modulation).

Figure 7-15 and Figure 7-16 show the phase noise measurements of the OEO at 1550 nm and 1612 nm with frequency modulation of laser source. Note that a moving window filter (percentile filter with window size of 20 and percentile of 40) was applied to filter out frequency modulation harmonic peaks to reveal the trend of phase noise spectra. It can be seen from the figures that when laser frequency modulation is applied, the phase noise levels of the OEO with the HC-PBGF delay-line and with the SMF delay-line becomes similar. Furthermore similar phase noise levels can be seen at 1550 nm and at 1612 nm. This suggests that increased phase noise in the OEO with HC-PBGF delay-line was caused by intensity noise due to multipath interference and once that noise is suppressed, same phase noise levels can be achieved in the OEO with the two different delay-lines.

7.8 Conclusions

In this chapter I experimentally demonstrated zero and negative thermal characteristics in a long-length (>1 km) HC-PBGF incorporated in an OEO by changing the operational wavelength of the laser. This was achieved by compensating the effect of temperature induced fibre elongations by temperature induced group index change that has an opposite effect so that light propagates faster in the thermally elongated fibre (and slower in a thermally shrunk fibre).

By examining the measured chromatic dispersion profiles and insertion loss profiles of the available fibres, a 1090 m long HC-PBGF that had the lowest insertion loss when the chromatic dispersion is 79 ps/nm/km (the approximated value of chromatic dispersion corresponding to zero-TCD [16]) was selected for the experiments.

Using the OEO setup, the chromatic dispersion of the whole length of the fibre was measured by measuring the change of OEO output signal frequency when the operational wavelength is varied. The results were similar to the chromatic dispersion measurements measured using the Mach-Zehnder interferometric method [16] with a short sample length (~ 3.5 m).

Then by placing the HC-PBGF delay-line in a thermal chamber and changing its temperature by 35°C (while minimizing the temperature induced frequency drifts caused by the rest of the OEO components), the corresponding frequency drifts of the OEO were measured at different operational wavelengths. Using the measured frequency drifts, the TCD of the HC-PBGF delay-line was calculated for the different operational wavelengths. The results showed that zero-TCD occurs near 1610 nm and that the TCD of the HC-delay-line is lower than that of an SMF by a factor of more than 100, in a 3 nm wide wavelength window between 1609 nm and 1612 nm.

As a complementary measurement, the Allan deviation of the OEO was measured at 1610 nm, after actively stabilizing the temperature of the HC-PBGF delay-line at 26°C and minimizing the frequency drifts caused by other OEO components. Compared to the minimum Allan deviation that was measured for the 860-m HC-PBGF delay-line based OEO in the previous chapter, an improvement could be seen at 1s and 1000 s sampling times. This improvement can be attributed to the operation of the OEO near the zero-TCD wavelength of the HC-PBGF delay-line as well as to the active stabilization of the HC-PBGF delay-line.

Phase noise of the OEO was measured at two wavelengths: at 1550 nm (when the TCD is positive) and 1612 nm (when the TCD is negative) with the HC-PBGF delay-line as well as with a 700 m long SMF delay-line for comparison. The operational wavelength did not change phase noise significantly. However due to multipath interference induced intensity noise, phase noise of the OEO with the HC-PBGF delay-line was higher than that with the SMF delay-line at 1550 nm as well as at 1612 nm. In order to improve the phase noise of the OEO with the HC-PBGF delay-line, laser source of the OEO was frequency modulated. With frequency modulation of the laser, the phase noise levels of the OEO with the HC-PBGF delay-line and with the SMF delay-line became similar (at 1550 nm as well as at 1612 nm).

Parts of the work presented in this chapter have been published [151].

Chapter 8 Passive Fibre-optic Depolarizers for Narrow-linewidth Signal Depolarization: Configurations, Theoretical Analysis and Simulations

As discussed in Chapter 5, passive fibre-optic depolarizer can be seen as a more feasible method of producing depolarized light in fibre-optic systems compared to active or free-space optics based depolarizers. While broad-linewidth optical signal depolarization can be done by using simple fibre-Lyot depolarizers, narrow-linewidth signal depolarization is more challenging. Furthermore, in order to be incorporated into a practical signal depolarizing application, a depolarizer must be robust, stable, input-SOP independent, easily integratable, and free from post-fabrication alignments. Insertion loss and PDL of the depolarizer needs to be low as well. In addition it is highly desired that the depolarizer is cost effective and has a straight forward fabrication procedure. Optical fibre based, passive narrow-linewidth signal depolarizers that have been proposed in the literature lack at least one of these properties. This limits their usability in practical scenarios.

In this chapter, I propose two fully-fibreized passive depolarizer configurations to address the issues related to the already reported passive narrow-linewidth signal depolarizers. After presenting the depolarizer configurations, a mathematical model of the depolarizers is presented. The results of the simulations carried out using the mathematical model which show how the depolarizer performance is affected by non-ideal component and fabrication errors are also presented.

8.1 Depolarizer Configurations

The first depolarizer follows the previously reported Mach-Zehnder depolarizer [123], but with an all-PM design approach. The device has a low insertion loss and in terms of cost-effectiveness, more suitable for depolarization of input signals with linewidths >5 MHz (this depolarizer will be referred to as the PM-depolarizer in the text). The second depolarizer allows SMFs to be used as delay-lines in a reflection based setup with FRMs similar to the Michelson depolarizer [125]. In terms of fabrication costs, this depolarizer (which will be referred to as the SMF-depolarizer in the text) is more suitable for depolarization of input signals with linewidths <5 MHz (down to sub-megahertz linewidths). Both depolarizers are fully fibreized with SMF input and output ports. The fabrication process of the depolarizers is straight forward and they do not require any polarization alignments during operation.

8.1.1 PM-depolarizer

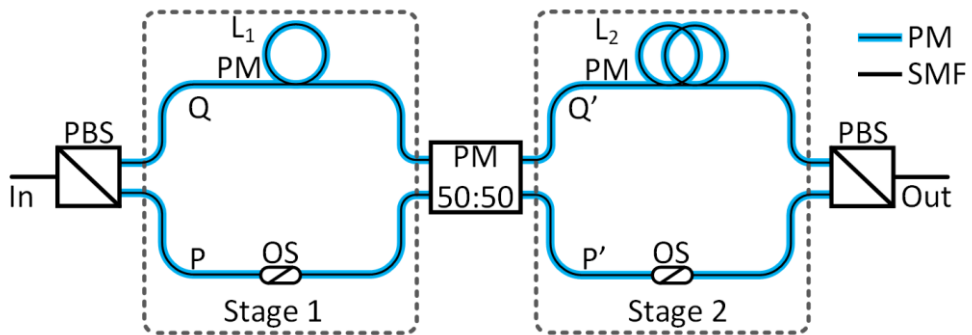


Figure 8-1 Schematic of the PM-depolarizer. PBS: Polarization beam splitter, OS: Offset splice. Losses of P and P' are intentionally increased at OSs during splicing to match the losses of Q and Q' respectively.

The schematic diagram of the proposed PM-depolarizer is shown in Figure 8-1. The difference between this depolarizer and the previously reported Mach-Zehnder depolarizer [123] is that all the components of this depolarizer including the PBSs, the coupler and the delay-lines are PM type. The PBSs in the setup are three port components with one SMF port (as the input) and two PM fibre ports (as output ports). Signals are coupled to the slow axes of the PM fibre ports of the PBS while the fast axes are being blocked (hence known as a fast axis blocking). The 2×2 PM fibre coupler is also a fast axis blocking component and has a 50:50 coupling ratio. The PM-depolarizer has two depolarizing stages (Stage 1 and Stage 2) and each stage consists of two fibre paths (P and Q in Stage 1 and P' and Q' in Stage 2). The path difference between fibres in Stage 1 and Stage 2 are L_1 and L_2 . The differential delays induced in Stage 1 and Stage 2 are set to 1:2 ratio by setting L_2 two times longer than L_1 .

The input signal is split by a PBS into orthogonal components (will be referred to as x and y components) and launched into P and Q along the slow axes. Signals propagating through P and Q paths are coupled into the two input ports of the fibre coupler (along the slow axes). Signals exiting the coupler along the slow axes of its two output ports are launched into P' and Q' paths along the slow axes. The ends of P' and Q' paths are connected to the two PM ports of a second PBS and again, the signals are launched into PM ports along their slow axes. The PBS (now operating as a polarization beam combiner, PBC) recombines the signals and delivers the depolarized output signal through its SMF port. In order to control the power balance between P, Q and P', Q' paths, offset splices (OS, shown in Figure 8-1) are made by intentionally offsetting the fibres at the splice points in P and P' paths to increase splice losses.

8.1.2 SMF-depolarizer

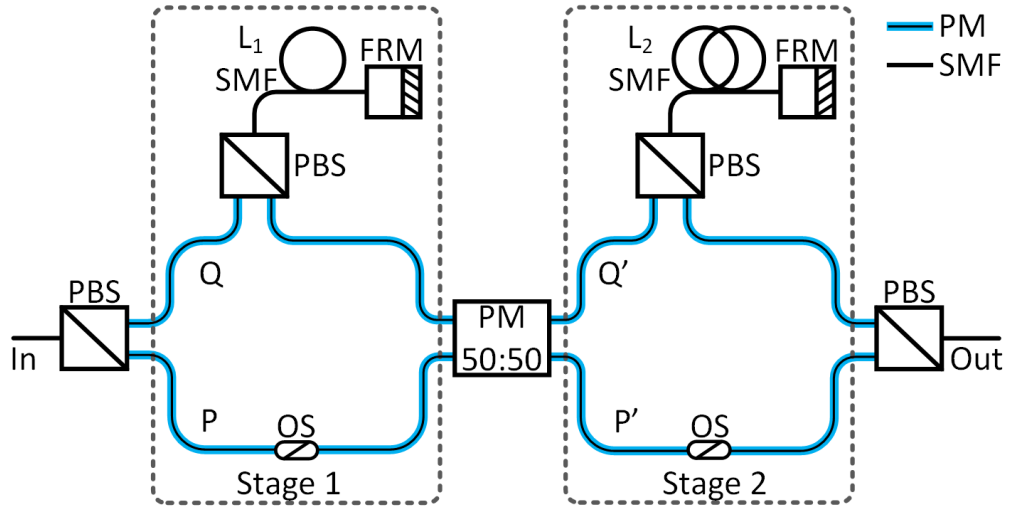


Figure 8-2 Schematic of the SMF-depolarizer. PBS: Polarization beam splitter, FRM: Faraday rotator mirror, OS: Offset splice. Losses of P and P' are intentionally increased at OSs during splicing to match the losses of Q and Q' respectively.

The Schematic diagram of the proposed SMF-depolarizer is shown in Figure 8-2. Similar to the PM-depolarizer, the SMF-depolarizer has a two-stage depolarizing setup with 1:2 delay ratio and consists of two fast axis blocking PBSs at the input and the output. A fast axis blocking 2×2 fibre coupler with a 50:50 coupling ratio is used to cascade the two depolarizing stages. Similar to the PM-depolarizer, the input signal is split and propagated along the slow axes of the PM components. However in contrast to the PM-depolarizer, SMF-based delays consisting of a fast axis blocking PBS (similar to the ones at the input and output), an SMF delay-line and a fibre coupled FRM with 90° double pass rotation are used to induce delays. One end of the SMF delay-line is connected to the SMF port of the PBS and the other end is connected to the FRM. When a signal is launched along the slow axis of one of the PM ports of the PBS, signal exits through the SMF port and propagates through the SMF delay-line. Then the signal gets reflected from the FRM, propagates back through the SMF delay-line and arrives at the PBS with a 90° rotated SOP compared to the input-SOP irrespective of SOP changes that occur along the SMF (SOP changes that occur in the signal during the transmission is reversed when reflecting back through the same fibre) [152], [153]. In addition to allowing low-cost SMFs to be used in the depolarizer, the reflection based setup doubles the delay induced by each delay-line, further reducing the fabrication costs. One key difference between this depolarizer and the previously reported Michelson depolarizer [125] is the replacement of the half-wave plate cascading the depolarizing stages with a fibre coupler. Furthermore, similar to the PM-depolarizer, offset splices are used in P and P' paths to control the power balance between P, Q and P', Q' paths.

As explained, in both PM-depolarizer and SMF-depolarizer, input signal components are propagated only through the slow axes of the PM components. Furthermore the fast-axis blocking fibre couplers and PBSs used in the depolarizers are commercially available and by using them the fabrication process can be simplified and the splicing between PM components can be done simply with 0° rotation to allow slow axis signal propagation. Furthermore the use of fast-axis-blocking components also helps to improve the depolarizer performance by minimizing potential polarization cross-talk.

8.2 Theoretical Analysis of the Depolarizers

The Lyot depolarizer has been theoretically studied in prior work [118], [121], [154], [155] and being linear two-stage depolarizers, the Lyot depolarizer and the proposed depolarizers share a similar operational principle. However there are differences in the implementations and hence, some factors affecting the performance in the proposed configurations need to be studied in detail. For example, in a fibre-Lyot depolarizer, signals get coupled from the first fibre (Stage 1) to the second fibre (Stage 2) at the interface of the two fibres and the required 45° relative rotation of birefringent axes can be set during the fabrication. However in the proposed depolarizers PM-fibre couplers with fixed coupling ratios are used to couple signals from Stage 1 to Stage 2 and it is important to analyse how depolarizer performance vary with coupling ratio variations. Furthermore due to insertion losses of components and splices, the proposed depolarizers have dissimilar losses associated with the two fibre paths in each depolarizing stage. This is different from a fibre-Lyot depolarizer where signals propagate along the slow and the fast axes of the same fibre so that they experience similar losses. The dependency of DOP on the losses of the arms of the Michelson-depolarizer has been studied [125] but assuming that the coupling between the two depolarizing stages is ideal. It is important to study how the depolarizer performance vary with fibre path losses when the coupling is non-ideal (which is the case in practice) and to investigate if the effect of non-ideal coupling ratio of the coupler can be compensated by tuning the fibre path losses.

Following previous work on Lyot depolarizers [118], [154], [155], I derived a mathematical model to analyse how coupling ratio variations and fibre paths losses affect the output signal DOP and PDL of the proposed depolarizers. It should be noted here that since the two proposed depolarizers, apart from the technique of inducing delays, are equivalent, this theoretical analysis is equally valid for both of them.

The x , y components of the input launched in to P and Q paths (denoted by E_x and E_y respectively) can be written as,

$$\text{Input} = \begin{bmatrix} E_x \\ E_y \end{bmatrix} = \begin{bmatrix} E(t) \cos(\alpha) \\ E(t) \sin(\alpha) \end{bmatrix}, \quad 8-1$$

where $E(t)$ represents the analytical signal of the input and input-SOP is denoted by α . Input signal gets fully coupled to P when α is 0° and gets fully coupled into Q when α is 90° . When the coupling ratio of the 2×2 coupler is $C:(100-C)$ its transformation matrix can be written as,

$$R = \begin{bmatrix} \sqrt{r} & -\sqrt{1-r} \\ \sqrt{1-r} & \sqrt{r} \end{bmatrix}, \quad 8-2$$

where $r=C/100$. When differential delays of the Stage 1 and Stage 2 are τ_1 and τ_2 (corresponding to L_1 and L_2 respectively) and when A_K denotes the losses of the fibre paths P, Q, P', and Q' ($0 \leq A_K \leq 1$, K denotes the fibre path the loss associated with), the x, y components of the output signal can be written as,

$$\text{Output} = \begin{bmatrix} E_{x'} \\ E_{y'} \end{bmatrix} = \begin{bmatrix} A_P A_P, \sqrt{r} E(t + \tau_1 + \tau_2) \cos(\alpha) - A_Q A_P, \sqrt{1-r} E(t + \tau_2) \sin(\alpha) \\ A_Q A_Q, \sqrt{r} E(t) \sin(\alpha) + A_P A_Q, \sqrt{1-r} E(t + \tau_1) \cos(\alpha) \end{bmatrix}. \quad 8-3$$

The coherency matrix J corresponding to the output signal can be written according to [156],

$$J = \begin{bmatrix} \langle E_{x'}^* E_{x'} \rangle & \langle E_{x'}^* E_{y'} \rangle \\ \langle E_{y'}^* E_{x'} \rangle & \langle E_{y'}^* E_{y'} \rangle \end{bmatrix} = \begin{bmatrix} J_{xx} & J_{xy} \\ J_{yx} & J_{yy} \end{bmatrix}, \quad 8-4$$

where time averages are denoted by angled brackets ($\langle \rangle$) and complex conjugates are denoted by $*$. Using elements of J , DOP can be calculated according to [156],

$$\text{DOP} = \sqrt{1 - \frac{4(J_{xx} \cdot J_{yy} - |J_{xy}|^2)}{(J_{xx} + J_{yy})^2}}. \quad 8-5$$

Furthermore the total intensity of the signal is given by the sum of the diagonal elements ($J_{xx} + J_{yy}$) of the coherency matrix [157]. PDL can be calculated from the maximum and minimum values of $J_{xx} + J_{yy}$ obtained when the input-SOP is varied according to,

$$\text{PDL} = 10 \log \left[\frac{(J_{xx} + J_{yy})_{\max}}{(J_{xx} + J_{yy})_{\min}} \right], \quad 8-6$$

Using equation 8-3 and following ref. [155], the elements of J corresponding to the depolarizer output signal can be written as,

$$J_{xx} = IA_P,^2 [A_P^2 r \cos^2(\alpha) + A_Q^2 (1-r) \sin^2(\alpha) - A_P A_Q \sqrt{r-r^2} \text{Re}\{\gamma(\tau_1)\} \sin(2\alpha)], \quad 8-7$$

$$J_{yy} = IA_Q^2 [A_Q^2 r \sin^2(\alpha) + A_P^2 (1-r) \cos^2(\alpha) + A_P A_Q \sqrt{r-r^2} \operatorname{Re}\{\gamma(\tau_1)\} \sin(2\alpha)], \quad 8-8$$

$$J_{xy} = \frac{I}{2} A_P' A_Q' [A_P A_Q \sin(2\alpha) [r\gamma^*(\tau_1 + \tau_2) - (1-r)\gamma^*(\tau_2 - \tau_1)] + 2\sqrt{r-r^2}\gamma^*(\tau_2)(A_P^2 \cos^2(\alpha) - A_Q^2 \sin^2(\alpha))], \quad 8-9$$

$$J_{yx} = J_{xy}^*, \quad 8-10$$

where I denotes irradiance, $\gamma(t)$ denotes complex degree of coherence function and $\operatorname{Re}\{\}$ denotes real component. The function $\gamma(t)$ is a measure of correlation between two time delayed signals and it depends on the delay τ , centre frequency (f_0), FWHM (Δf) and spectral shape of the signal. The $\gamma(t)$ functions corresponding to Gaussian and Lorentzian spectral-shaped signals are as follows [158]:

$$\gamma_{Gaussian}(\tau) = e^{-\left(\frac{\pi\Delta f \tau}{2\sqrt{\ln 2}}\right)^2} e^{-j2\pi f_0 \tau}, \quad 8-11$$

$$\gamma_{Lorentzian}(\tau) = e^{-\pi\Delta f |\tau|} e^{-j2\pi f_0 \tau}. \quad 8-12$$

8.3 Simulations

Based on the theoretical analysis, I carried out several simulations. The objective of these simulations was to investigate how depolarizer parameters and input signal parameters affect the performance of the depolarizers. First of all, the effect of the drifts of time delays induced by the delay-lines (τ_1 and τ_2) and the centre frequency of the input signal (f_0) on output signal DOP is studied. Next, the relationship between linewidth of the signal to be depolarized and the required delay-line lengths in the depolarizers is plotted. Then the effect of coupling ratio of the fibre coupler on output signal DOP is studied. The effect of losses of fibre paths on DOP of the output signal is studied afterwards. Finally the effects of the coupling ratio of the coupler and fibre path losses on PDL of the output-signal is studied. Specifically, the study is focused on how the above mentioned parameters must be controlled in order to maintain the output signal DOP below 5% when all input-SOPs are considered. Furthermore, since the experimental work presented later is also based on similar input signals, for this theoretical study I considered fully polarized input-signals of Lorentzian spectral shape.

8.3.1 Effect of the Fluctuations of Centre Frequency (f_0) and Induced Time Delays (τ_1 and τ_2)

It can be seen from equation 8-12 that the value of $\gamma(t)$ oscillates depending on the values of f_0 and τ . As a result, variations of DOP can also be expected for fluctuations of f_0 and τ . Such

fluctuations are common in practice, for example, variations of f_0 , can occur due to input-signal variations caused by the signal source and fluctuations of τ_1 and τ_2 can occur due to delay-line length fluctuations caused by ambient temperature variations and acoustic waves. In order to study the effect of these fluctuations on the DOP of the output signal, DOP was plotted against the linewidth (Δf) of the input-signal by varying f_0 around 193.5 THz (1550 nm) and a similar variation can be expected for fluctuations of τ_1 and τ_2 as well. An SMF-depolarizer with L_1 and L_2 values of 10 and 20 m (20 and 40 m delay-lines in the case of a PM-depolarizer) was assumed. For the simulation results shown in Figure 8-3, α was set to 45° and similar variations occur at other input-SOPs as well.

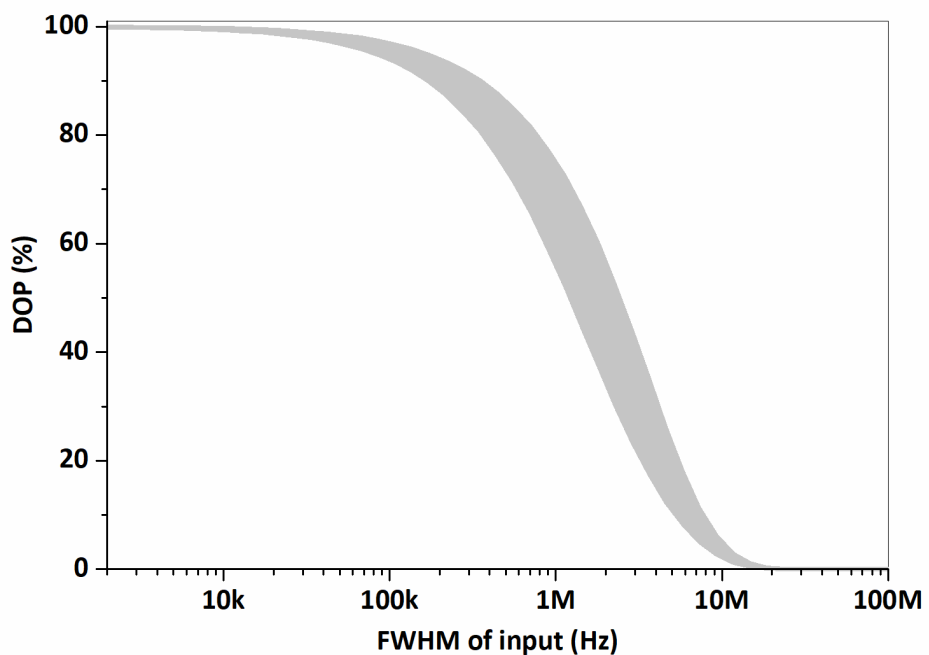


Figure 8-3 The range of DOP variation of the output signal that can be expected for fluctuations of the centre frequency of the input signals (f_0) and/or the induced time delays (τ_1, τ_2). The DOP variation corresponding to an input-SOP of 45° is shown.

The total range of DOP variation that can be expected for fluctuations of f_0 (or τ_1 and τ_2) is shown by the greyed area in Figure 8-3. The upper boundary of the grey-area corresponds to the maximum DOP (worst-case) that can be expected due to these fluctuations. These boundary values can be obtained by replacing $\gamma(t)$ with $|\gamma(t)|$ in equation 8-7 to equation 8-10. Since the objective is to identify the limiting performance of the depolarizer (worst-case performance) and then optimize it, in following simulations $\gamma(t)$ functions were replaced with $|\gamma(t)|$. Furthermore it is important to note that the model becomes independent of f_0 after this replacement (see equation 8-12).

8.3.2 Delay-line Length Requirements

The minimum fibre delay-line length requirement in Stage 1 (L_1) of the proposed depolarizers in order to depolarize an input-signal with an arbitrary SOP to a residual DOP below 5% was plotted against the FWHM of the input signal (delay-line length in Stage 2 (L_2) is set to $2L_1$). As shown in Figure 8-4, input-signals with FWHM in 100s of megahertz-scale can be depolarized with several meters of fibres and input-signals with FWHMs in 1 megahertz-scale requires 100s of meters of delay-lines for depolarization. Furthermore, the SMF-depolarizer requires 2 times less delay-line length compared to the PM-depolarizer for depolarization.

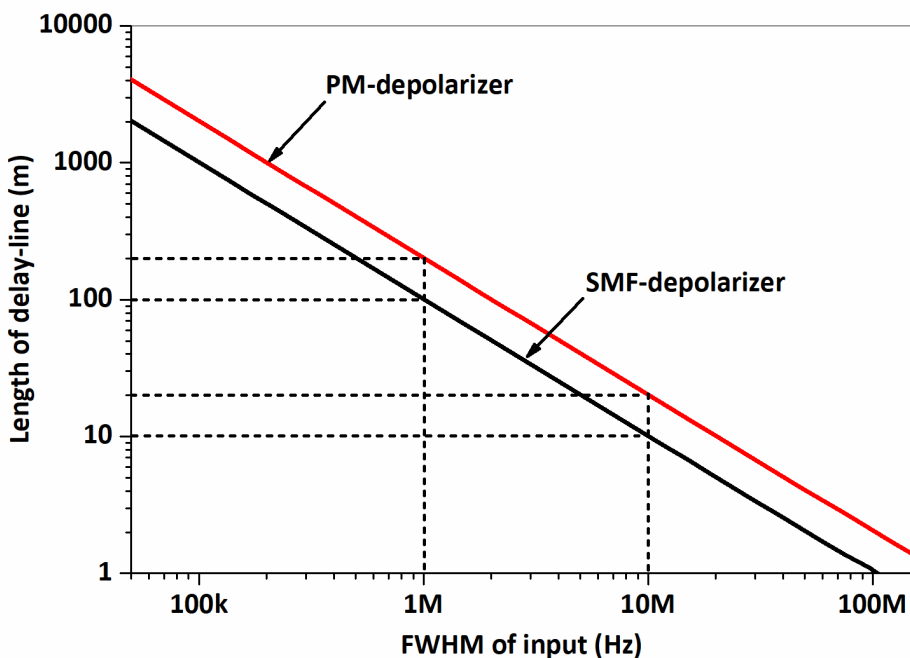


Figure 8-4 The variation of minimum required delay-line lengths in Stage 1 (L_1) of the proposed depolarizers (when L_2 is set to $2L_1$) to reach output signal DOP level below 5% when FWHM linewidth of the input signal is varied.

8.3.3 Dependency of the DOP on Coupling Ratio Variations of the Coupler

The effect of coupling ratio variation of the coupler on the DOP of the output signal was studied by plotting output signal DOP against coupling ratio for input signals with different input-SOPs. For this simulation, an input-signal with an increased linewidth so that $\tau_c \ll \tau_1, \tau_2$ was assumed. This was done to ensure that simulated DOP variations are a resulted by coupling ratio variations and not limited by the induced delays of delay-lines. The results are shown in Figure 8-5. It can be seen that 50:50 indeed is the ideal coupling ratio and that 0% DOP can be obtained for any input-SOP at this coupling ratio. When the coupling ratio deviates from the ideal value, DOP becomes input-SOP dependent. When coupling ratio is non-ideal, DOP gets maximized when input-SOP is

0° or 90° because input-signal propagates through either P or Q so that no depolarization occurs in Stage 1. DOP gets minimized when input-SOP is 45° so that input signal gets equally split between P and Q and completely depolarized in Stage 1. Moreover if deviation of a coupler from the ideal 50:50 ratio is d ($0 \leq d \leq 50$) so that,

$$\text{Coupling ratio} = (50 - d):(50 + d), \quad 8-13$$

it can be observed from Figure 8-5 that the maximum DOP (DOP_{\max}) that can be expected if that coupler is used in the depolarizer is,

$$DOP_{\max} = 2d. \quad 8-14$$

Therefore it is clear that in order to maintain the output signal DOP below 5%, the coupling ratio of the coupler used in the depolarizer needs to be between 47.5:52.5 and 52.5:47.5 (as shown in Figure 8-5).

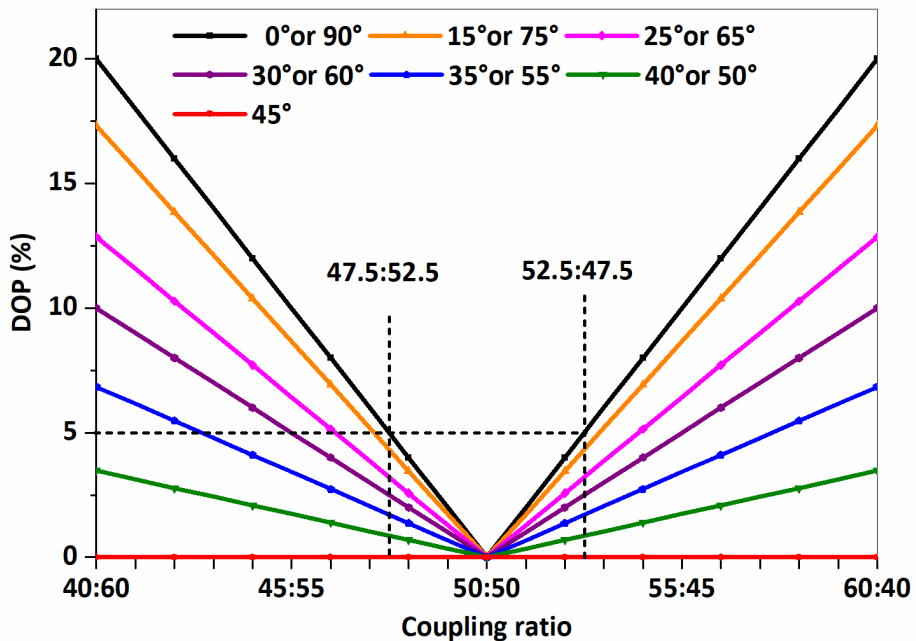


Figure 8-5 The variation of output signal DOP as a function of the coupling ratio of the coupler for different input-SOPs. To maintain output signal DOP below 5% for all input-SOPs, the coupling ratio must be between 47.5:52.5 and 47.5:52.5.

8.3.4 Dependency of DOP on Fibre Path Losses in Stage 1

When it comes to the losses of fibre paths, it is the differential loss between fibre paths in each depolarizing stage (Stage 1 and Stage 2) that affects the DOP of the output-signal (note that the differential loss can be either positive or negative depending on which path is more lossy). When simulating the effects of these differential losses, again, for both Stage 1 and Stage 2, an input

signal with an increased linewidth (so that $\tau_c \ll \tau_1, \tau_2$) was assumed to ensure that the results are not limited by the induced time delays.

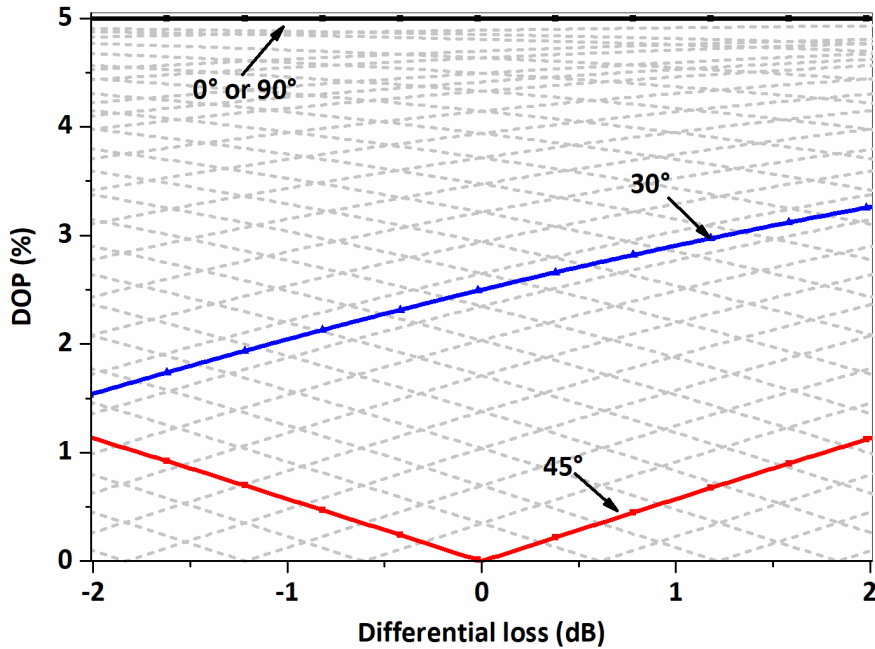


Figure 8-6 The variation of output signal DOP as a function of the differential loss between fibre paths in Stage 1 when the coupling ratio of the coupler is 47.5:52.5. DOP variations for different input-SOPs are shown.

If the coupling ratio of the coupler has an ideal 50:50 ratio, 0% DOP can be achieved for all input-SOPs, irrespective of the differential losses in Stage 1 (Note that introducing a differential loss in Stage 1 is the same as input-SOP being changed and the simulation on coupling ratio also confirmed that 0% DOP can be achieved irrespective of input-SOP if the coupling ratio is 50:50). However when the coupling ratio is not 50:50, output signal DOP becomes both differential loss and input-SOP dependent. The DOP variation corresponding to a coupling ratio of 47.5:52.5 is shown in Figure 8-6. The grey-lines show the DOP variations for different input-SOPs and the DOP variations corresponding to 0°, 30°, 45° and 90° SOPs have been labelled. When the coupling ratio is 47.5:52.5, a DOP variation between 0 and 5% can be expected irrespective of the differential loss. DOP gets minimized (0%) when differential loss is counter balanced by input-SOP and regardless of the differential loss, DOP gets maximized (5%) when input-SOP is 0° and 90° (i.e. when no depolarization occur in Stage 1). The value of maximum DOP (5%) is determined by coupling ratio.

8.3.5 Dependency of DOP on Fibre Path Losses in Stage 2

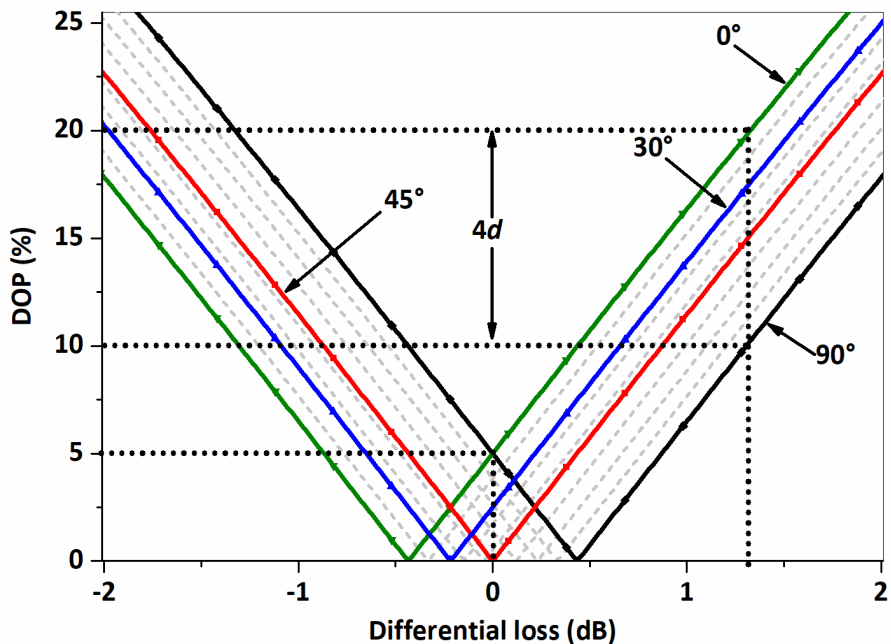


Figure 8-7 The variation of output signal DOP as a function of the differential loss between fibre paths in Stage 2 when the coupling ratio of the coupler is 47.5:52.5. DOP variations for different input-SOPs are shown. The red-line also shows the DOP variation for any input-SOP when the coupling ratio of the coupler is 50:50.

The differential loss between fibre paths in Stage 2 is responsible for the output signal DOP directly because it changes the power balance between the x , y components of the output signal. When the coupling ratio is 50:50, the DOP variation (as shown by the red-line in Figure 8-7) increases with the differential loss. However the DOP variation is independent of the input-SOP because x , y components of input signal (propagating through P and Q) are equally split between P' and Q' by the coupler. In this case DOP can be minimized (down to 0%) by minimizing differential losses. When the coupling ratio is not 50:50, DOP becomes both input-SOP and differential loss dependent. The DOP variation corresponding to a coupling ratio of 47.5:52.5 is shown in Figure 8-7. The grey-lines show the DOP variation for different input-SOPs and the DOP variations corresponding to input-SOPs of 30°, 45°, and also 0° and 90° (which bounds the range of DOP variation) have been labelled. When the coupling ratio is not ideal, DOP gets minimized and maximized when input-SOP is 0° and 90° depending on the sign of the differential loss. Only when the differential loss is relatively low (less than ~ 0.5 dB in the case of 47.5:52.5 coupling ratio), a minimum DOP of 0% can be achieved when differential loss is counter balanced by input-SOP. However it should be noted that for a given differential loss, 0% DOP cannot be achieved at all input-SOPs and the coupling-ratio-limited best possible performance (maximum output DOP of $\leq 5\%$ in this case) can be obtained by minimizing differential losses.

8.3.6 Indirect Estimation of Coupling Ratio of the Coupler

Figure 8-7 offers a method of indirectly measuring the coupling ratio of the coupler used in the depolarizer. This is done by increasing the differential loss in Stage 2 temporarily (by bending a fibre) and measuring the DOP variation. As shown in Figure 8-7, in the case of 47.5:52.5 coupling ratio (where $d=2.5$), when the differential loss is increased to a value between 1 and 2 dB and the input-SOP is varied, the output signal DOP varies by 10% (e.g., between 10% and 20% as shown in Figure 8-7). The deviation d of the coupler can be obtained by dividing the measured DOP variation by 4 ($d= (10/4) =2.5$). Such method is useful in practice because it can be used to accurately estimate the coupling ratio even after the fabrication of the depolarizer.

8.3.7 Dependency of PDL on Fibre Path Losses in Stage 1

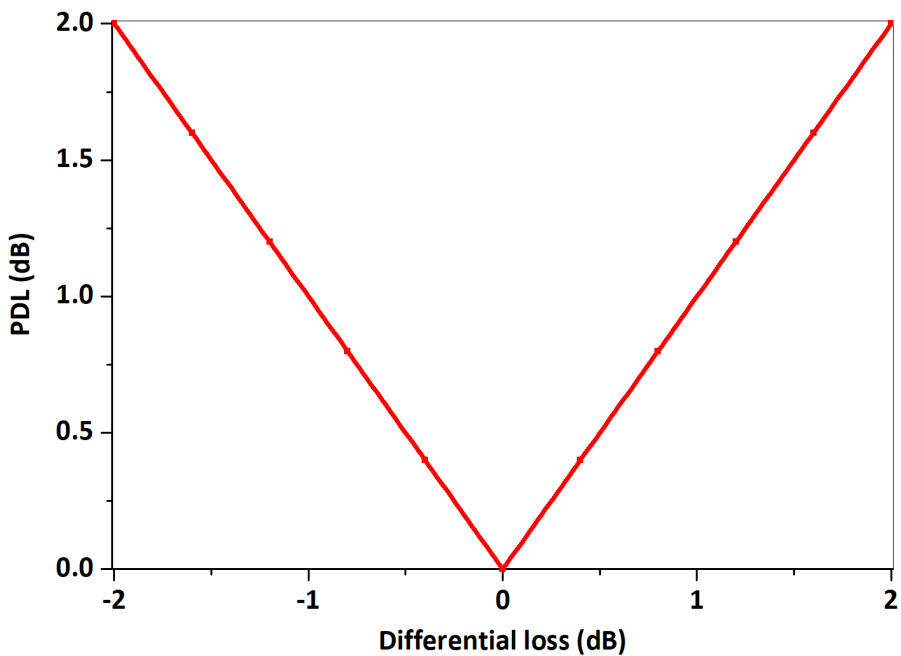


Figure 8-8 The variation of output signal PDL as a function of the differential loss between fibre paths in Stage 1. PDL variation does not depend on coupling ratio.

It can be seen from Figure 8-8 that PDL has a strong dependence of the differential loss of Stage 1. In fact, the PDL is equal to the differential loss of Stage 1 because the output signal power gets minimized when input signal propagates only through the higher loss path in Stage 1 and gets maximized when the input signal propagates only through the lower loss path Stage 1. Furthermore since all the light that is launched into the input ports of a coupler exits from the output ports irrespective of the coupling ratio (assuming a loss-less coupler), PDL is independent of the coupling ratio of the coupler. This shows that even though the DOP is independent of the differential loss of Stage 1, it needs to be minimized in order to minimize the PDL.

8.3.8 Dependency of PDL on Fibre Path Losses in Stage 2

The variation of PDL as a function of the differential loss in Stage 2 at two coupling ratios (50:50 and 47.5:52.5) and two differential loss levels in Stage 1 (0 dB and 0.05 dB) is shown in Figure 8-9. As shown by the blue-line, if the coupling ratio is 50:50, the PDL is equal to the differential loss of Stage 1 irrespective of the differential loss of Stage 2. However if the coupling ratio is not 50:50, PDL is determined by the differential loss of both Stage 1 and Stage 2 as well as the coupling ratio of the coupler. In addition, it can be seen that the effect of the differential loss of Stage 2 is significantly lower than that of the differential loss of Stage 1.

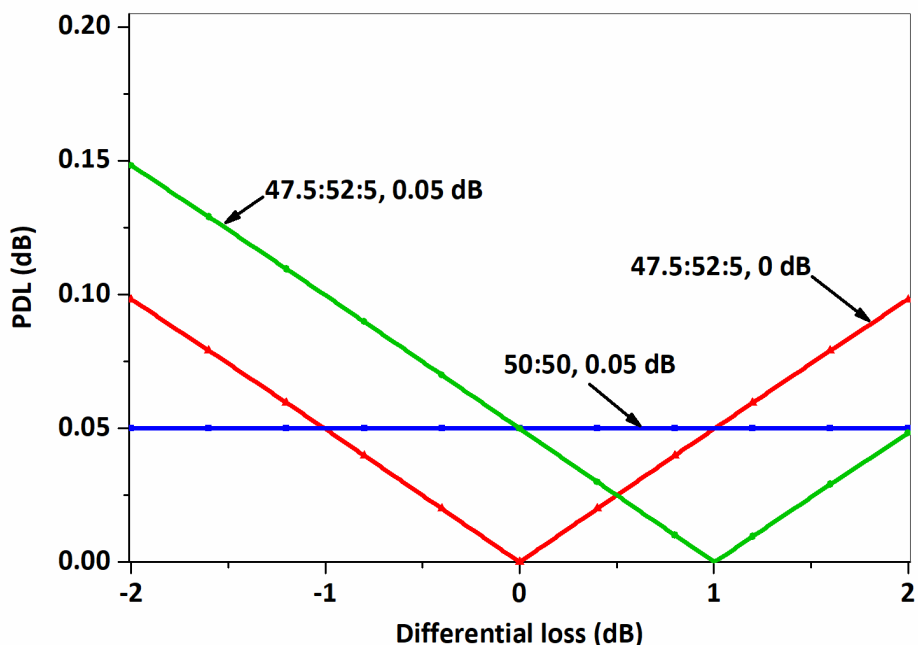


Figure 8-9 The variation of output signal PDL as a function the differential loss between fibre paths in Stage 2 when the coupling ratio is 50:50 and when the coupling ratio is 47.5:52.5.

Since the simulated characteristics can be approximated with linear relationships, simplified analytical formulas were later developed to calculate the effects of coupling ratio imperfections and differential losses of fibre paths on DOP and PDL. These formulas are given in Appendix A.

8.4 Conclusions

From the simulation results it can be concluded that fibre coupler is the most crucial component of the depolarizer and that 50:50 is the ideal coupling ratio. When the coupling ratio is ideal, depolarization is immune to differential losses in Stage 1. However differential losses in Stage 2 degrades depolarization performance in an input-SOP independent manner. When the coupling

Chapter 8

ratio is not-ideal, output DOP of an input signal becomes a function of the input-SOP, the differential loss in Stage 1 and the differential loss Stage 2. However when all input-SOPs are considered, DOP does not depend on differential losses in Stage 1 but the DOP variation increases with the differential losses in Stage 2. In addition the effect of a non-ideal coupling ratio cannot be compensated by adjusting the losses of the fibre paths so that depolarization is improved for all input-SOPs. The differential loss of Stage 1 strongly affects the PDL hence needs to be minimized even though it does not affect the DOP. The differential loss of Stage 2 also affects the PDL if the coupling ratio of the coupler is not 50:50. However its effect on PDL is significantly lower than that of Stage 1. In conclusion, for optimum performance of the depolarizer in terms of both the DOP and the PDL, a coupler with a coupling ratio as close as possible to 50:50 must be used and the differential losses of Stage 1 and Stage 2 must be minimized.

Parts of the work presented in this chapter have been published [159].

Chapter 9 Passive Fibre-optic Depolarizers for Narrow-linewidth Signal Depolarization: Fabrication and Characterization

Following simulation results of the previous chapter and identifying how the performance of the proposed depolarizers vary with the differential losses of fibre paths and coupling ratio of the coupler, a fabrication procedure for the depolarizers was developed and several prototypes of the proposed depolarizer configurations were fabricated and characterised. The depolarizer fabrication procedure, the characterisation procedure and the performance of the fabricated depolarizers are presented in this chapter.

9.1 Wavelength Dependency of Couplers

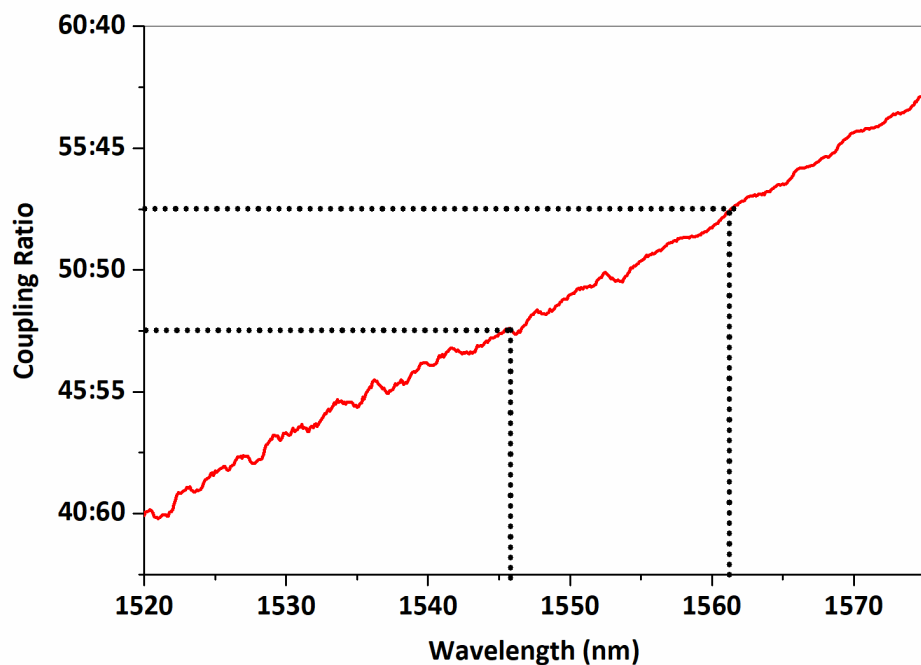


Figure 9-1 Experimentally measured coupling ratio variation of a PM coupler when the operational wavelength is varied. With this coupler, the operational wavelength range must be within 1546 nm and 1561 nm to maintain output signal DOP below 5%.

The simulations suggested that the ultimate performance of the depolarizer is limited by the coupling-ratio of the coupler. In practice the coupling-ratio of a coupler is wavelength dependent. For example, Figure 9-1 shows the coupling ratio variation of a 50:50 PM fused coupler that I

measured. It can be seen that if this coupler is to be used in a depolarizer, the input-signal needs to be between 1546 nm and 1561 nm in order to keep the coupling ratio better than 47.5: 52.5 so that the output signal DOP can be maintained below 5%. This also suggests that in some applications, tuning the wavelength of the input-signal can be used as a feasible method of optimizing the performance of the depolarizer.

It should be noted that this was a measurement of a common fused coupler that was available in the laboratory. I presented this measurement as an example of the wavelength dependency of the fibre-optic couplers (and fibre-optic components in general) and this measurement was made after fabricating the depolarizers. The particular fast-axis blocking PM couplers that I used to fabricate depolarizers had a specified operational wavelength range of ± 40 nm centred at 1550 nm (however I did not measure the wavelength dependency of these couplers before incorporating them in the depolarizers) and such couplers can be fabricated using thin-film technology. The used PBSs also had a specified operational wavelength range ± 40 nm centred at 1550 nm. The specified centre wavelength of the used FRMs was 1550 nm. The operational wavelength range of the FRMs was not specified in the datasheet, however in general, it is in the order of several tens of nanometres.

9.2 Depolarizer Fabrication Procedure

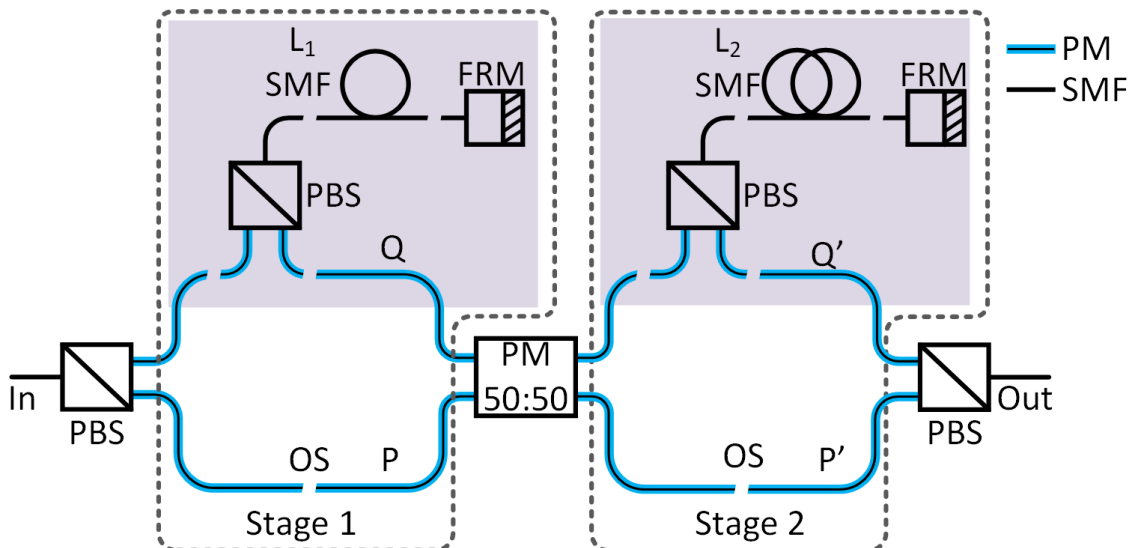


Figure 9-2 Schematic of SMF-depolarizer with all the splice points shown by terminating the paths. PBS: Polarization Beam Splitter, FRM: Faraday Rotator Mirror, OS: offset splice.

This fabrication procedure is equally applicable to both the PM-depolarizer and the SMF-depolarizer. The schematic diagram of the SMF-depolarizer shown in Figure 9-2, with splice points

shown by terminating the fibre paths, is used as the reference figure for this explanation. The first step of the fabrication procedure is to select a coupler with an acceptable coupling ratio over the wavelength range of operation. The next step is to splice the components together. The PM splices between components should be done with 0° relative rotation between fibres and the fabrication strategy that can be used to minimize differential losses between fibre paths in Stage 1 and Stage 2 of the depolarizers can be outlined as follows: The paths Q and Q' suffer from higher losses compared to P and P' due to the additional components used to induce delays. Hence the losses in P and P' need to be increased to match the losses of Q and Q' respectively.

To complete Stage 1, first, all the splices in Q (splices inside the shaded area of Stage 1 in Figure 9-2) are done with minimum splice losses. Next the fibres that need to be spliced to complete P are placed in the fibre splicer and aligned (but not spliced). Then a polarized broad-linewidth signal is launched into the coupler through P' and Q' one at a time while measuring the DOP at the input port with a polarization analyser. The fibres in the splicer are now manually misaligned until the DOP converges in to a same minimum value for both cases (when signal is launched through P' and through Q') and then they are spliced.

To complete Stage 2, all the splices in Q' (splices inside the shaded area of Stage 2 in Figure 9-2) are done with minimum splice losses. Next, the fibres that need to be spliced to complete P' are placed in the fibre splicer and aligned (but not spliced). A Polarized broad-linewidth signal is launched into the depolarizer through the input port while monitoring DOP at the output port. Similar to Stage 1, the signal should be launched into the coupler through P and Q one at a time while fully blocking the signal through the other. However since P and Q are now fully spliced, this is can be done non-destructively by bending the fibres. Again, the fibres in the splicer are manually misaligned until the DOP converges into the same minimum value for both cases (when signal is launched through P' and through Q') and then they are spliced.

9.3 Depolarizer Characterization

9.3.1 Variable Linewidth Input Signal Generation

I characterized the depolarizers by measuring the output signal DOP by varying the FWHM of the input signal. Input signals with variable linewidths were generated by varying the bias current of three laser diodes (LD₁, LD₂ and LD₃). The lasers were driven with a low noise laser driver. Due to the wavelength dependency of couplers used in the depolarizers, the measurements were made at different wavelengths. LD₁ and LD₂ were operating at 1547 nm and LD₃ was operating at 1555 nm. The lasers produced fully polarized Lorentzian spectral shaped signals and I used the self-

heterodyne linewidth measurement scheme [160] to measure the FWHM linewidth of the lasers. Using LD₁ and LD₂ a total linewidth variation from 100 kHz to 21.5 MHz was obtained at 1547 nm. LD₃ provided a linewidth variation from 525 kHz to 23 MHz (see Figure 9-3).

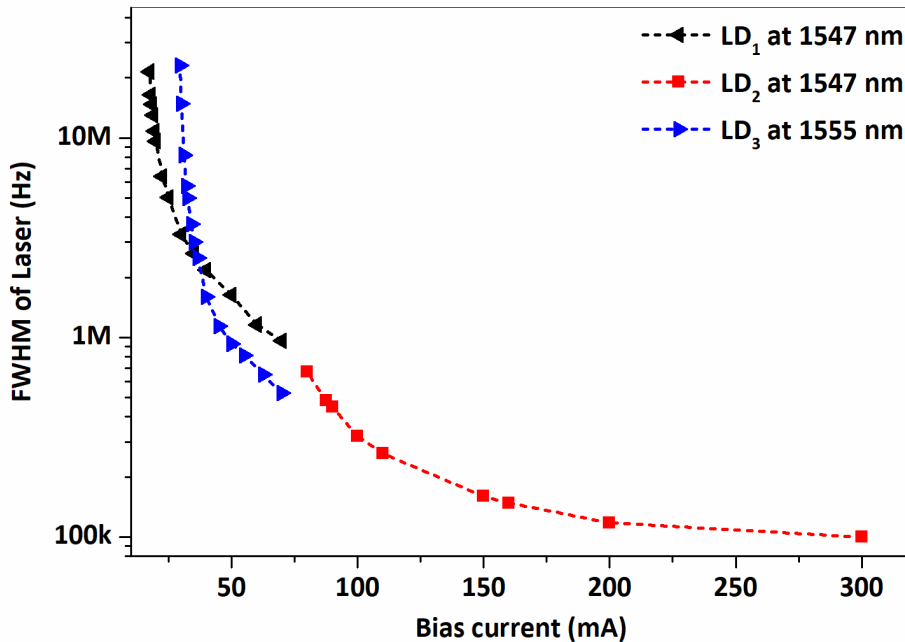


Figure 9-3 The FWHM linewidth variation of the lasers when the bias current is varied. LD₁ and LD₂ operates at 1547 nm and LD₃ operates at 1555 nm.

9.3.1.1 Laser Linewidth Measurement Scheme

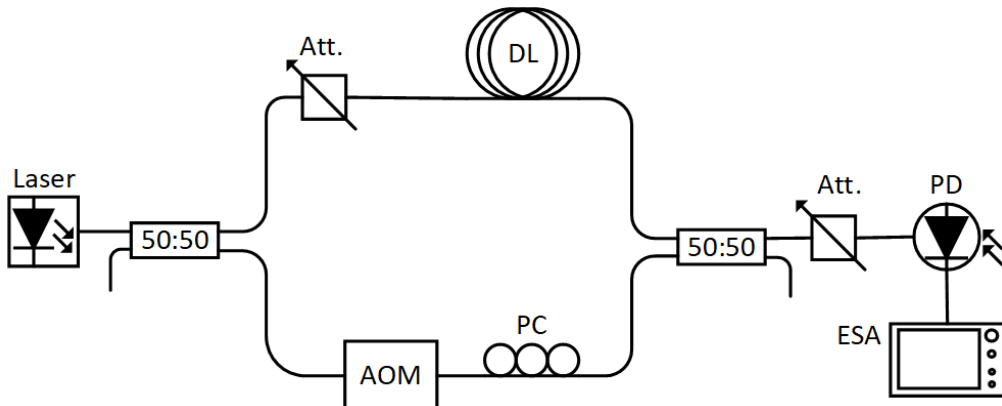


Figure 9-4 Schematic of the self-heterodyne linewidth measurement scheme. DL: Delay-line, AOM: Acousto-optic modulator, PC: Polarization controller, Att.: Optical attenuator, PD: Photodiode, ESA: Electrical spectrum analyser.

Linewidth of a laser can be measured from the beating between the laser signal and a local oscillator signal (signal from a stable narrow-linewidth laser) [161]. However obtaining a stable reference oscillator operating at a frequency close to the laser under test can be difficult. On the other hand, the laser signal can also be beaten with a delayed version of itself to obtain the laser linewidth. This scheme is known as the self-heterodyne linewidth measurement scheme and is

more convenient as there is no need for a local oscillator [160], [161]. This scheme was used to measure the linewidths of the lasers used for the characterization of depolarizers.

The schematic diagram of the linewidth measurement scheme is shown in Figure 9-4. In this scheme, the signal is split by a 50:50 coupler and launched into two paths. In one path, light is launched through an acousto-optic modulator (AOM) to introduce a 35 MHz frequency shift and in the other path, light is launched through a 10 km long SMF to decorrelate the signals in the two paths. Then, light from the two paths are recombined by a 50:50 coupler and the RF beating at 35 MHz is monitored by an electrical spectrum analyser. When the RF beating spectrum is Lorentzian shaped, the actual laser linewidth is given by half of the FWHM of the RF beating spectrum [160].

9.3.2 DOP Measurement Setups

I used two setups to obtain DOP measurements. In the first setup, an HP8509B polarization analyser was used to measure DOP values. DOP can be calculated from Stokes parameters [162] and the polarization analyser computes the Stokes parameters of the input signal using a setup of four photodiodes [163]. Since DOP is dependent on the input-SOP, a polarization controller was used to vary the SOP of the input signal before launching into the depolarizer. At different input signal linewidths, I varied the SOP of the input signal and recorded the maximum DOP value (which corresponds to the worst-case performance). The setup is shown in Figure 9-5. Unless specifically mentioned, this setup was used as the default measurement scheme for DOP measurements in the experimental work.

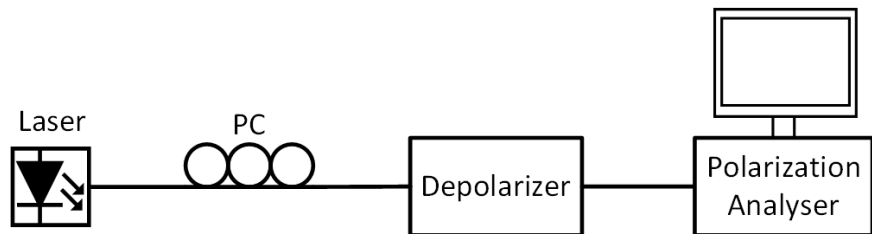


Figure 9-5 Schematic of the DOP measurement setup with polarization analyser (default setup). PC: Polarization controller.

However when DOP of the signal fluctuates rapidly (e.g., due to fluctuations of τ_1 , τ_2 , and f_0) and when the acquisition rate of the polarization analyser is not capable of measuring these fast variations (due to the limited acquisition rate), DOP values measured by the polarization analyser can become erroneous. In this case, I used a second setup to measure DOP. The setup is shown in Figure 9-6 and its operation is as follows: When a fully depolarized optical signal is launched through a polarizer one half of the signal gets through while the other half is being blocked. When a fully polarized optical signal is launched through a polarizer, the amount of light that exits the

polarizer depends on the relative orientation of the SOP of the input signal and the polarization axis of the polarizer, and the signal can be fully blocked or fully allowed through by changing their relative orientation. Hence when partially polarized depolarizer output signal (that consists of both polarized and depolarized components) is launched through a polarizer and the SOP of the signal is varied using a polarization controller, the minimum intensity (I_{min}) and the maximum intensity (I_{max}) of the signal at the polarizer output can be written in terms of the intensities of polarized ($I_{polarized}$) and depolarized ($I_{depolarized}$) components according to,

$$I_{min} = \frac{I_{depolarized}}{2}, \quad 9-1$$

$$I_{max} = \frac{I_{depolarized}}{2} + I_{polarized}. \quad 9-2$$

The DOP which is defined as [164],

$$DOP = \frac{I_{polarized}}{I_{total}}, \quad 9-3$$

where I_{total} is the total intensity of light, can be written in terms of I_{min} and I_{max} according to,

$$DOP = \frac{I_{max} - I_{min}}{I_{max} + I_{min}}. \quad 9-4$$

This second setup is shown in Figure 9-6. In the setup, depolarizer output signal is launched into a polarizer through a polarization controller. A photodiode is placed after the polarizer to generate electrical signals proportional to the intensity of the optical signal incident on it. The electrical signals are measured using an oscilloscope. DOP can be calculated by using the minimum and maximum electrical signal values (V_{min} and V_{max}) according to,

$$DOP = \frac{V_{max} - V_{min}}{V_{max} + V_{min}}. \quad 9-5$$

Here again a polarization controller is used to change the SOP of the depolarizer input signal and the maximum DOP values were recorded at different input signal linewidths.

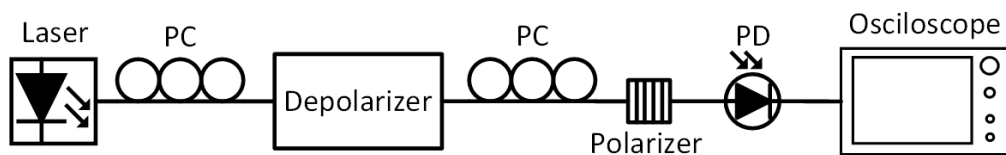


Figure 9-6 Schematic of the manual DOP measurement setup used when the acquisition time of the polarization analyser was not sufficient (secondary setup). PC: Polarization controller, PD: Photodiode

9.4 Experimental Results

In order to test the performance of the proposed depolarizers in practice, three depolarizers were built and characterized. First one is a PM-depolarizer with 20 and 40 m delay-lines for the depolarization of input signals with 10s of megahertz-scale linewidths (a cost-effective choice of delay-line lengths for a typical PM-depolarizer). The second one is an SMF-depolarizer with 10 and 20 m delay-lines. This depolarizer induces similar differential delays to that of the first one allowing a direct performance comparison between them. The third one is an SMF-depolarizer with 200 and 400 m delay-lines for the depolarization of input-signals with few megahertz-scale linewidths. This choice of delay-line lengths is typical for the SMF-depolarizer and hence, allows evaluation of their true narrow-linewidth signal depolarization capability. Furthermore the coupling ratios of the couplers used in the depolarizers were measured during the characterization using the method discussed in section 8.3.6 and the simulated maximum DOP variations of the three depolarizers are also presented along with the experimental results.

9.4.1 PM-depolarizer with 20 and 40 m Delay-lines

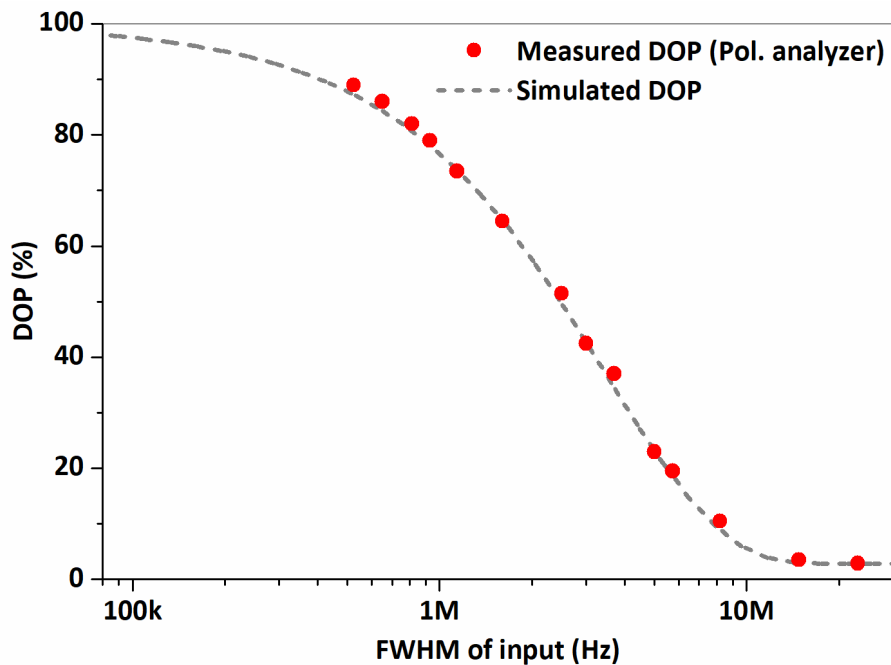


Figure 9-7 Experimentally measured output signal DOP variation of the PM-depolarizer with 20 and 40 m PM delay-lines at 1555 nm. Simulated DOP variation is also shown.

Measured maximum DOP variation of the PM-depolarizer with 20 and 40 m PM fibre delay-lines are shown in Figure 9-7. The depolarizer DOP was measured at 1555 nm (using LD_3) and at this wavelength the coupling ratio of the coupler was measured to be 48.6:51.4. The simulated

maximum DOP variation of the depolarizer for this coupling ratio is also shown. The experimental results and simulated curve closely follow each other and agree on the minimum achievable DOP of $\sim 3\%$ for signal linewidths above 20 MHz. This indicates the depolarization performance of the device is limited by the coupling ratio and that the differential loss in Stage 2 of the depolarizer is minimum. The measured insertion loss of the depolarizer was 1.35 dB. The PDL was 0.2 dB. Since the differential loss of Stage 2 is minimum, PDL suggests that the differential loss of Stage 1 should be 0.2 dB.

9.4.2 SMF-depolarizer with 10 and 20 m Delay-lines

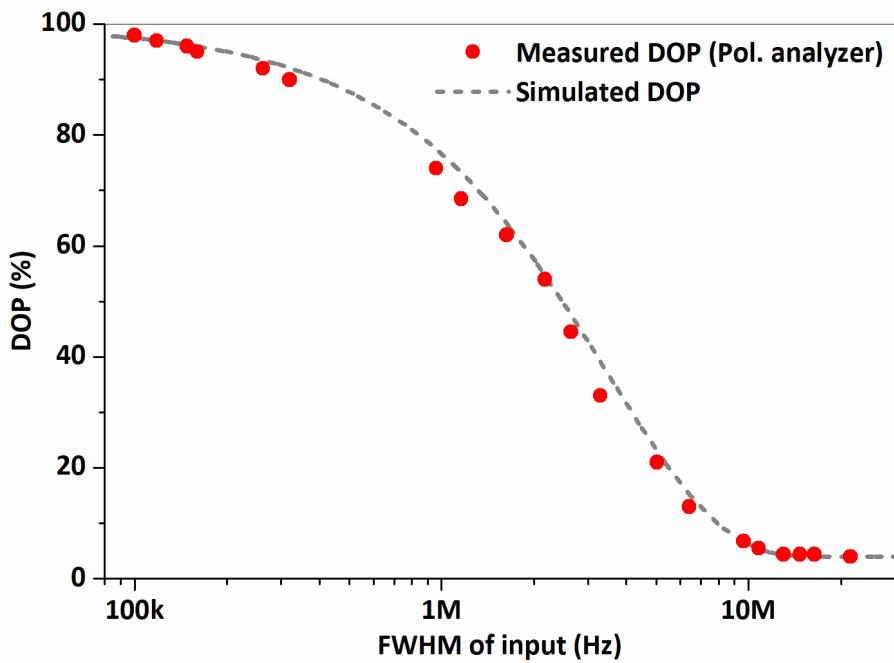


Figure 9-8 Experimentally measured output signal DOP variation of the SMF-depolarizer with 10 and 20 m PM delay-lines at 1547 nm. Simulated DOP variation is also shown.

The measured maximum DOP variation of the SMF-depolarizer with 10 and 20 m SMF delay-lines are shown in Figure 9-8. Depolarizer was characterized at 1547 nm (using LD_1 and LD_2) and at this wavelength the coupling ratio of the coupler was measured to be 48:52. The simulated maximum DOP variation of the depolarizer with this coupling ratio is also shown. The experimental results closely follow the simulated curve and agree on the minimum achievable DOP level of $\sim 4\%$ for signal linewidths above 20 MHz. This shows that the differential loss in Stage 2 of the depolarizer is minimum and the minimum achievable DOP is limited by the coupling ratio. When compared with the PM-depolarizer, it can be seen that the depolarizing characteristics of the two devices are same. It is important to note that the SMF-depolarizer achieves the same performance using two times shorter SMF delay-lines compared to the PM-depolarizer. However due to the

additional components such as PBSs and FRMs, the insertion loss of the SMF-depolarizer is higher than the PM-depolarizer and the insertion loss of this device was measured to be 4 dB. The PDL was 0.14 dB. Since the differential loss of Stage 2 is minimum, PDL suggests that the differential loss of Stage 1 should be 0.14 dB.

9.4.3 SMF-depolarizer with 200 and 400 m Delay-lines

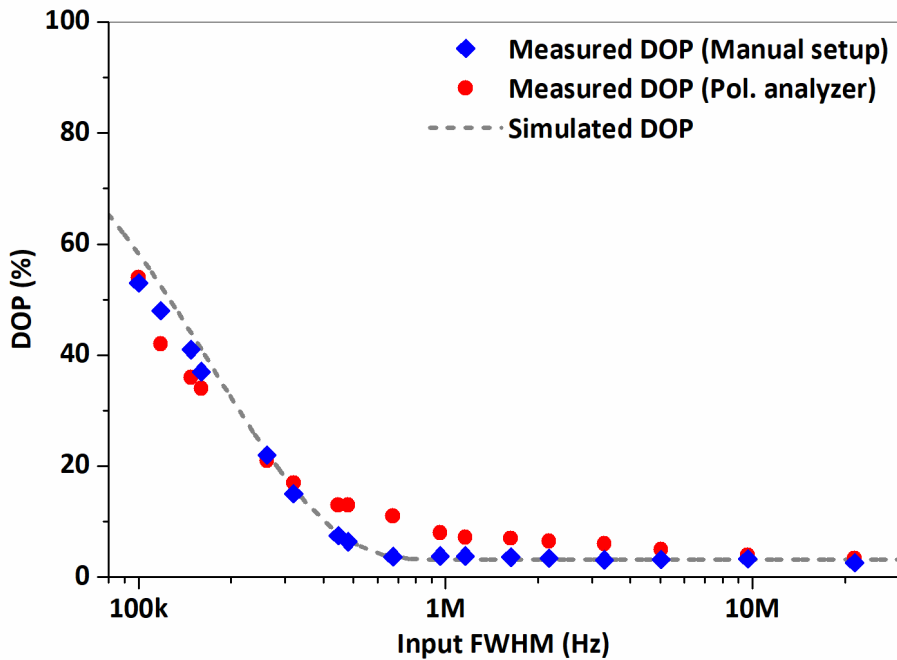


Figure 9-9 Experimentally measured output signal DOP variation of the SMF-depolarizer at 1547 nm with 200 and 400 m PM delay-lines. Simulated DOP variation is also shown.

Measured maximum DOP variation of the SMF-depolarizer with 200 and 400 m delay-lines are shown in Figure 9-9. The depolarizer was characterized at 1547 nm (using LD_1 and LD_2) and at this wavelength, the coupling ratio of the coupler was measured to be 49:51. Minimum achievable DOP limited by the coupler should be 2%. However the experimentally measured minimum achievable DOP was $\sim 3\%$, suggesting a slight power imbalance between fibre paths (a differential loss) in Stage 2. I simulated the DOP variation of the depolarizer with a 49:51 coupling ratio and a 0.1 dB differential loss in Stage 2. The simulated curve (shown in Figure 9-9) agrees with the minimum achievable DOP. However it can be seen that even though there is an agreement on the minimum achievable DOP and the overall trend, the measurements obtained using the default setup (using the polarization analyser) do not closely follow the simulated curve. This can occur when the rapid fluctuations of DOP (due to fluctuations of τ_1 , τ_2 , and f_0) are being erroneously measured by the polarization analyser due to its limited acquisition speed.

Hence the measurements were repeated using the second DOP measurement setup (in Figure 9-6). The measurement results shown by the diamond symbols in Figure 9-9 closely follow the simulated curve over the whole measurement range and also agree on the minimum achievable DOP. The insertion loss of the device which was measured to be 5.6 dB is slightly higher than the previous SMF-depolarizer due to higher losses of the components. The PDL of this depolarizer was measured to be 0.05 dB. According to simulations, if the coupling ratio is 49:51 and the differential loss of Stage 2 is 0.1 dB, the differential loss of Stage 1 should be 0.048 dB or 0.052 dB (depending on the exact sign of differential loss of Stage 1 and the coupling ratio) for the PDL to be 0.05 dB.

9.5 Conclusions

In this work I proposed and fabricated two fully fibreized depolarizer configurations that operate in the spectral domain for narrow-linewidth signal depolarization. Both configurations are input-SOP independent and are free from post-fabrication alignments. Out of the two configurations, the PM-depolarizer uses PM delay-lines to induce time delays. This device is a cost-effective solution for depolarization of signals with >5 MHz linewidths. The SMF-depolarizer uses SMF delay-lines to induce differential delays in a reflection based setup with FRMs. This depolarizer is cost-effective for the depolarization of input signals with <5 MHz linewidths.

The simulations revealed that the ultimate depolarization performance of the depolarizers is determined by the coupling ratio of the coupler used in the depolarizers and the differential loss of fibre paths of the Stage 2 of the depolarizers. The PDL is mainly governed by the differential losses of Stage 1.

Following the findings of simulations, I outlined a straightforward procedure for the fabrication of depolarizers and the depolarizer can be built with commercially available fibre-optic components. I fabricated three depolarizer prototypes: a PM-depolarizer and an SMF-depolarizer capable of depolarizing input signals with linewidths >20 MHz, and another SMF-depolarizer that is capable of depolarizing input signals with linewidths >1 MHz. The output signal DOP of all depolarizers was below 4% and the PDLs was below 0.2 dB. Out of the fabricated prototypes, PM-depolarizer has lower insertion loss of 1.35 dB. Even though SMF-depolarizers have higher insertion loss (4 dB and 5.6 dB in the prototypes) due to the higher component count, allowing SMFs to be used as delay-lines cut back costs significantly when it comes to narrow-linewidth (few megahertz or lower) signal depolarization.

Parts of the work presented in this chapter have been published [159].

Chapter 10 Conclusions and Suggestions for Future Work

The incorporation of HC-PBGFs in OEOs to improve the temperature stability of the OEO generated signals was investigated in the work presented in this thesis. First, I built a 10 GHz single-loop OEO setup incorporating an 860 m long HC-PBGF with 19-cell core structure. By operating the OEO at 1550 nm, I showed that frequency drifts caused by temperature induced delay changes of the delay-line can be reduced by a factor of 15.8 by using a HC-PBGF delay-line instead of an SMF delay-line of similar delay. At this operational wavelength, the HC-PBGF delay-line had a measured TCD of 2.2 ps/km/K which was mainly caused by the temperature induced fibre elongations of the HC-PBGF. The short term stability of the OEO was also investigated by measuring the phase noise. The phase noise of the OEO was higher (by 11 dB at a 1 kHz offset and 3 dB at a 10 kHz offset) with the HC-PBGF delay-line compared to the phase noise of the OEO when an SMF delay-line of similar delay and similar loss was used. This phase noise degradation can be attributed to the multipath interference induced intensity noise in the HC-PBGF. To the best of my knowledge, this is the first time a long-length (>800 m) of HC-PBGF was incorporated in an OEO. Furthermore to the best of my knowledge, this is the first time phase noise properties of long-length (>800 m) HC-PBGF delay-line based OEO were measured in detail.

Next, by building another OEO setup and incorporating a different 19-cell structured HC-PBGF, I showed that by changing the operational wavelength of the OEO, temperature induced frequency drifts of the OEO can be further reduced by reaching zero and even negative TCD characteristics of a HC-PBGFs. This was done by operating the OEO near the long-wavelength edge of the bandgap at which the group index gets decreased when the temperature is increased. In this wavelength region the effect of fibre elongations gets counterbalanced by the increase of group velocity (i.e. light propagates faster in the elongated fibre) so that by tuning the operational wavelength, zero and even negative TCD characteristics of the HC-PBGF can be reached [16].

Even though zero-TCD characteristics can be reached in any HC-PBGF in theory [16], making use of the zero-TCD characteristic of HC-PBGFs can be limited by the high insertion loss of the HC-PBGFs at the long-wavelength edge of the bandgap in practice. For example, the insertion loss of the 860 m long HC-PBGF delay-line used in the previous experiments was estimated to be ~ 20 dB at its approximated zero-TCD wavelength of 1600 nm. Hence for this experiment, a 1090 m long HC-PBGF with much lower insertion loss of < 11 dB at its approximated zero-TCD wavelength of 1607 nm was used. The approximated zero-TCD wavelengths were obtained by analysing the chromatic dispersion profiles of the HC-PBGFs and identifying wavelengths corresponding to the approximated zero-TCD dispersion of 79 ps/nm/km [16].

The chromatic dispersion of the whole length of the delay-line used in the OEO can also be measured using the OEO setup itself. This can be done by measuring the change of OEO output signal frequency for a slight change of the operational wavelength of the OEO. I measured the chromatic dispersion of the 1090 m long HC-PBGF between 1520 and 1616 nm using this method and the results showed a good agreement with the chromatic dispersion profile of the fibre measured using a free-space Mach-Zehnder interferometric method [16]. To the best of my knowledge, measurement of chromatic dispersion of the incorporated delay-line using the OEO setup itself has not been demonstrated before.

I used this 1090 m long HC-PBGF in the OEO and varied the operational wavelength from 1530 nm to 1615 nm and identified that zero-TCD wavelength is between 1609 nm and 1612 nm. Furthermore it could be seen that the TCD of the HC-PBGF within a 3 nm wavelength window between 1609 and 1612 nm is lower than the ~ 40 ps/km/K TCD of SMF by a factor of more than 100. Similar to the previous case, the phase noise of this OEO with the HC-PBGF delay-line was higher than that with an SMF delay-line of similar delay (and similar loss) due to multipath interference in the HC-PBGF. However by frequency modulation of the laser source, phase noise of the OEO with the HC-PBGF delay-line could be reduced to the level of the phase noise of the OEO with the SMF delay-line.

HC-PBFs with insertion loss as low as 4 dB/km (at 1550 nm) were used as delay-lines in OEOs in the experiments. In general, the HC-PBGFs that are currently being fabricated exhibit higher insertion loss compared to that of standard SMFs. Hence a HC-PBGF delay-line based OEO requires higher amplification in the OEO loop compared to an OEO with an SMF delay-line of similar delay. The phase noise of the OEO can degrade when additional RF amplifiers are used in the OEO loop (to provide the additional amplification) [165]. However it should be noted that an overall improvement of short-term stability of HC-PBGF delay-line based OEOs can be expected in the future when lower insertion loss HC-PBGFs become available. Furthermore it can be expected that optimized HC-PBGFs in which the zero-TCD wavelength lie within the lowest transmission loss region of the bandgap and designed to have a broad wavelength window with near-zero TCD characteristics will be available in the future [16]. These improvements will further increase the usability of HC-PBGFs in temperature insensitive applications and also expand the application space of HC-PBGFs.

The work presented in this thesis was focused on investigating the temperature stability improvement that can be obtained by using HC-PBGFs in a specific application; microwave signal generation using delay-line based OEO. For this work, OEO setups with single-loop architecture were used. Similarly, HC-PBGF delay-lines can also be incorporated in other delay-line based OEO

configurations such as multi-loop OEOs, COEOs and injection locked OEOs (discussed in Chapter 2) to improve the temperature stability. Furthermore the results of the investigations show that in addition to OEOs, HC-PBGFs can also be used to improve various other instrumentation, synchronization and signal transmission applications.

HC-PBGFs can be used in instrumentations applications in which long optical delay-lines are used; for example, in fibre-optic gyroscopes [104] and in delay-line based laser stabilization systems [16], [105]. In addition, HC-PBGFs can be used in precise synchronization and timing applications due to their superior temperature sensitivity characteristics. Synchronization of high-speed robots in industrial manufacturing and processing is one potential application [16]. Timing and synchronization is extremely important in large-scale scientific experiments, e.g., in synchrotrons, free electron laser facilities [102] and linear particle accelerators [14][16]. HC-PBGFs can potentially be used in such large-scale experiments to transfer signals between different instruments and sub-systems to keep them synchronized. In large telescope arrays, precise timing signals need to be distributed among the individual telescopes located over a large area [14]. Moreover, optical fibre links needs to be used to compare optical clocks in laboratories at different locations. The accuracy of such experiments can degrade when the propagation time through the signal distribution links change due to ambient temperature variations [16]. HC-PBGFs can be seen a potential candidate to be used as signal distribution links in such demanding situations. Additionally it can be seen that HC-PBGFs have the potential to be used in high-speed data transfer applications in data centres and 5G networks [16], [103] where precise timing and synchronization is critical. It should be noted that in some of the applications mentioned above, standard SMFs are/can be used with various active stabilization methods (including active temperature stabilization and locking methods). However by using HC-PBGFs, the systems can either be simplified by removing active stabilization methods or HC-PBGFs can be used together with active stabilization methods to achieve a significant performance improvement.

In conclusion it can be said that the work presented in this thesis not only show that a superior temperature stability can be achieved in OEOs by replacing the standard SMF delay-lines with HC-PBGF delay-lines but also provide a strong basis for future work by proving low-loss long-length HC-PBGFs are ready to be employed in real-world applications.

Since HC-PBGFs can exhibit undesired polarization properties such as PDL and polarization mode coupling [20]–[22], and since the performance of a HC-PBGF delay-line incorporated OEO can be degraded due to these properties, I developed two fibre-optic depolarizer configurations to be used in OEOs and other applications to suppress polarization sensitivity. These depolarizers are

passive, fully fibreized and capable of narrow-linewidth (down to sub-megahertz-scale) signal depolarization irrespective of the input-SOP and without any post-fabrication alignments.

The depolarization in these depolarizers is obtained by decorrelating components of the input signal by inducing differential delays between them. The first depolarizer (PM-depolarizer) uses PM fibre delay-lines and PM fibre-optic components, and is cost effective for >5 MHz linewidth signal depolarization. Due to the low component count, the Insertion loss of the depolarizer can be as low as 1.35 dB. The second depolarizer (SMF-depolarizer) also uses PM fibre-optic components but allows SMFs to be employed as delay-lines so that narrow linewidth signals can be depolarized without using long lengths of expensive PM fibre delay-lines. This depolarizer is more cost effective for the depolarization of input signals with <5 MHz linewidths, where the lower cost of the SMF delay-lines overcomes the cost of its additional components. Due to these additional fibre-optic components, the insertion loss of the depolarizer was higher than the PM-depolarizer (but can be as low as 4 dB).

After carrying out simulations to identify how fabrication and component imperfections affect the performance of the depolarizers, I developed a fabrication procedure to obtain the optimum performance of the depolarizers. The use of fast-axis blocking PM fibre coupler and PBSs is crucial in these depolarizer and fabrication procedure can be streamlined by using them. It should also be noted that all the fibre-optic components used to fabricate these depolarizers are available commercially. The fabricated depolarizer are capable of reducing the DOP of fully polarized input signals below 4% and the PDL of the depolarizers are below 0.2 dB.

The proposed depolarizers provide cost effective, narrow-linewidth signal depolarization solutions in robust, fully fibreized packages with post-fabrication alignment free and input-SOP independent operation. They have low PDL and low insertion loss. The depolarizers proposed in this thesis fill a current market gap by providing all the above mentioned features in a single product. Due to the compactness and fibreized nature, these depolarizers can be easily integrated into fibre-optic systems and due to the passive nature they do not require power and/or signal lines. These depolarizers can also operate as standalone devices to obtain depolarized narrow-linewidth light signals in various applications ranging from measurement systems [114] to sensing applications [115] and they are now being commercialized by Phoenix Photonics Ltd, UK (introduced at ECOC 2017).

10.1 Suggestions for Future Work

Even though the depolarizers developed during this work were finalized to a level at which they were commercialized to be used in general applications, they were not incorporated in OEOs to

investigate the performance improvement they can provide by suppressing the polarization related issues of HC-PBGFs. The main reasons for this was the higher insertion losses of the HC-PBGFs and time constraints (as my work on OEOs was carried out simultaneously with the work on the depolarizers). In addition, to identify the improvement that can be obtained, the polarization properties of the HC-PBGFs need to characterize in detail. These fibre characterizations could not be performed during the time of experimentations. Characterizing polarization properties of the HC-PBGFs and investigating how the proposed depolarizers can suppress polarization sensitivity of HC-PBGFs could be investigated as the next step. Afterwards the depolarizers could be incorporated into HC-PBGF delay-line based OEOs to evaluate the performance improvements that can be obtained. Power limitations due to the insertion loss of depolarizers could be overcome by higher power laser sources and/or optical amplifiers. It is worth pointing out that when employing a depolarizer in an OEO, the depolarizer can be placed outside the OEO loop (e.g., between the laser source and the optical modulator) so that the temperature induced delay changes in the (SMF or PM fibre) delay-lines of the depolarizer do not change OEO loop delay (and hence do not change the frequency of the OEO generated signal).

However it could be seen that the output signal DOP of the proposed depolarizers can vary due to temperature induced delay changes of delay-line fibres. Furthermore it could be seen that these DOP variations become rapid when long delay-lines are used. Developing an SMF-depolarizer type depolarizer by replacing SMFs with HC-PBGFs could reduce these DOP fluctuations significantly. However due to the higher insertion losses of the HC-PBGFs currently being fabricated, such depolarizers will suffer from high insertion loss.

These suggested work on OEOs and depolarizers can be investigated immediately. However on a broader perspective, it is important carry out further experimental work on long length HC-PBGF based applications (discussed in the first part of this chapter). Different applications have different requirements and they may also impose unique challenges and these challenges need to be overcome in order to use HC-PBGFs in more real-world applications.

Appendix A Analytical Formulas to Calculate how DOP and PDL is Affected by Coupling Ratio Imperfections and Fibre Path Losses

The following approximated linear formulas were derived with M. Ding to calculate how the minimum achievable DOP and PDL is affected by coupler coupling ratio and the differential losses of fibre paths (note: the work presented in this section have been published [159]). For this derivations $\gamma(t)$ functions were approximated to be zero by assuming a broad-linewidth input signal so that $\tau_c \ll \tau_1, \tau_2$. This simplifies in the elements of the coherency matrix as,

$$J_{xx} = IA_P'^2 [A_P^2 r \cos^2(\alpha) + A_Q^2 (1-r) \sin^2(\alpha)], \quad \text{A-1}$$

$$J_{yy} = IA_Q'^2 [A_Q^2 r \sin^2(\alpha) + A_P^2 (1-r) \cos^2(\alpha)], \quad \text{A-2}$$

$$J_{xy} = J_{yx} = 0, \quad \text{A-3}$$

and the DOP can be simplified as,

$$\text{DOP} = \left| \frac{J_{xx} - J_{yy}}{J_{xx} + J_{yy}} \right|. \quad \text{A-4}$$

Assuming $A_P = A_Q = A_P' = A_Q' = 1$, $I = 1$, and $r = 0.5 + \Delta r$ (Δr is the deviation from the ideal coupling ratio of 0.5), the relationship between minimum achievable DOP and Δr can be derived using equation A-1 to equation A-4 as,

$$\text{DOP} = |2\Delta r|. \quad \text{A-5}$$

Assuming $A_P = A_Q = 1$, $I = 1$, and $r = 0.5 + \Delta r$, DOP can be written using equation A-1 to equation A-4 as,

$$\text{DOP} = \left| \frac{\frac{A_P'^2}{A_Q'^2} [0.5 + \Delta r \cos(2\alpha)] - [0.5 - \Delta r \cos(2\alpha)]}{\frac{A_P'^2}{A_Q'^2} [0.5 + \Delta r \cos(2\alpha)] + [0.5 - \Delta r \cos(2\alpha)]} \right|. \quad \text{A-6}$$

By replacing $(A_P'/A_Q')^2$ with $10^{DL_2/10}$ where DL_2 is the differential loss of Stage 2 in decibels and using the first order Taylor series approximation of $10^{DL_2/10} \approx (1 + \ln(10)DL_2/10)$,

$$\text{DOP} = \left| \frac{\ln(10) DL_2 [0.5 + \Delta r \cos(2\alpha)]/10 + 2\Delta r \cos(2\alpha)}{\ln(10) DL_2 [0.5 + \Delta r \cos(2\alpha)]/10 + 1} \right|. \quad \text{A-7}$$

Appendix A

By approximating the denominator to be 1, the relationship between minimum achievable DOP and differential loss of Stage 2 can be written as (for small values of DL_2 and Δr),

$$DOP = \frac{\ln(10)|DL_2| [0.5 + |\Delta r|]}{10} + 2|\Delta r|. \quad A-8$$

By assuming $A_P = A_Q = 1$, $l = 1$, $r = 0.5 + \Delta$ and replacing $(A_P/A_Q)^2$ with $10^{DL_1/10}$ where DL_1 is the differential loss of Stage 1 in decibels, the relationship between DL_1 and PDL can be derived using maximum and minimum values of $J_{xx} + J_{yy}$ according to,

$$PDL = \left| 10 \log \left[\frac{A_Q^2 [10^{DL_1/10}]}{A_Q^2} \right] \right| = |DL_1|. \quad A-9$$

By assuming $l = 1$, $r = 0.5 + \Delta r$, replacing $(A_P/A_Q)^2$, $(A_{P'}/A_Q)^2$ with $10^{DL_1/10}$, $10^{DL_2/10}$ respectively and then using the first order Taylor series approximation of $10^{DL_2/10} \approx (1 + \ln(10)DL_2/10)$, PDL can be written as,

$$PDL = \left| DL_1 + 10 \log \left[1 + \frac{\ln(10)(0.5 + \Delta r)DL_2}{10} \right] - 10 \log \left[1 + \frac{\ln(10)(0.5 - \Delta r)DL_2}{10} \right] \right|. \quad A-10$$

Since $\log(1+x) \approx x/\ln(10)$, the relationship between DL_2 and PDL can be written according to,

$$PDL = |DL_1 + 2DL_2\Delta r|. \quad A-11$$

List of References

- [1] P. Devgan, "A review of optoelectronic oscillators for high speed signal processing applications," *ISRN Electronics*, vol. 2013, 2013.
- [2] L. Maleki and A. B. Matsko, "Optical generation of microwave reference frequencies," in *2011 XXXth URSI General Assembly and Scientific Symposium*, Istanbul, Turkey, 2011, pp. 1–4.
- [3] R. J. Matthys, *Crystal oscillator circuits*, Revised. Malabar, FL, USA: Kriger publishing company, 1992.
- [4] J. K. Plourde and C. L. Ren, "Application of dielectric resonators in microwave components," *IEEE Transactions on Microwave Theory and Techniques*, vol. 29, no. 8, pp. 754–770, 1981.
- [5] T. E. Parker and G. K. Montress, "Precision surface-acoustic-wave (SAW) oscillators," *IEEE Transactions on Ultrasonics, Ferroelectrics, and Frequency Control*, vol. 35, no. 3, pp. 342–364, 1988.
- [6] A. P. S. Khanna, "Microwave oscillators: The state of the technology," *Microwave Journal*, vol. 49, no. 4, pp. 22–28, 2006.
- [7] X. S. Yao and L. Maleki, "Optoelectronic microwave oscillator," *Journal of the Optical Society of America B*, vol. 13, no. 8, pp. 1725–1735, 1996.
- [8] X. S. Yao and L. Maleki, "A light-induced microwave oscillator," *The Telecommunications and Data Acquisition Progress Report 42-123*. pp. 47–68, 1995.
- [9] X. S. Yao, L. Maleki, and D. Eliyahu, "Progress in the opto-electronic oscillator - a ten year anniversary review," in *2004 IEEE MTT-S International Microwave Symposium Digest (IEEE Cat. No.04CH37535)*, Fort Worth, TX, USA, 2004, pp. 287–290.
- [10] L. Maleki, "The opto-electronic oscillator (OEO): Review and recent progress," in *2012 European Frequency and Time Forum*, Gothenburg, Sweden, 2012, pp. 497–500.
- [11] K. Saleh, P. H. Merrer, O. Llopis, and G. Cibiel, "Optoelectronic oscillator based on fiber ring resonator: Overall system optimization and phase noise reduction," in *2012 IEEE International Frequency Control Symposium Proceedings*, Baltimore, MD, USA, 2012, pp. 1–6.

List of References

- [12] A. B. Matsko, L. Maleki, A. A. Savchenkov, and V. S. Ilchenko, "Whispering gallery mode based optoelectronic microwave oscillator," *Journal of Modern Optics*, vol. 50, no. 15–17, pp. 2523–2542, 2003.
- [13] A. H. Hartog, A. J. Conduit, and D. N. Payne, "Variation of pulse delay with stress and temperature in jacketed and unjacketed optical fibres," *Optical and Quantum Electronics*, vol. 11, no. 3, pp. 265–273, 1979.
- [14] R. Slavík, G. Marra, E. N. Fokoua, N. Baddela, N. V. Wheeler, M. Petrovich, F. Poletti, and D. J. Richardson, "Ultralow thermal sensitivity of phase and propagation delay in hollow core optical fibres," *Scientific Reports*, vol. 5, p. 15447, 2015.
- [15] F. Poletti, N. V Wheeler, M. N. Petrovich, N. Baddela, E. Numkam Fokoua, J. R. Hayes, D. R. Gray, Z. Li, R. Slavík, and D. J. Richardson, "Towards high-capacity fibre-optic communications at the speed of light in vacuum," *Nature Photonics*, vol. 7, no. 4, pp. 279–284, 2013.
- [16] E. Numkam Fokoua, M. N. Petrovich, T. Bradley, F. Poletti, D. J. Richardson, and R. Slavík, "How to make the propagation time through an optical fiber fully insensitive to temperature variations," *Optica*, vol. 4, no. 6, pp. 659–668, 2017.
- [17] A. S. Daryoush, "Thermal sensitivity of photonic crystal fibers in opto-electronic oscillators," *Journal of China Universities of Posts and Telecommunications*, vol. 16, no. 4, pp. 1–6, 2009.
- [18] G. Beck, L. Bigot, G. Bouwmans, A. Kudlinski, J.-P. Vilcot, and M. Douay, "Benefits of photonic bandgap fibers for the thermal stabilization of optoelectronic oscillators," *IEEE Photonics Journal*, vol. 4, no. 3, pp. 789–794, 2012.
- [19] L. Zhang, V. Madhavan, R. P. Patel, A. K. Poddar, U. L. Rohde, and A. S. Daryoush, "Ultra low FM noise in passively temperature compensated microwave opto-electronic oscillators," in *IEEE MTT-S International Microwave and RF Conference*, New Delhi, India, 2013, pp. 1–4.
- [20] G. Bouwmans, F. Luan, J. Knight, P. St. J. Russell, L. Farr, B. Mangan, and H. Sabert, "Properties of a hollow-core photonic bandgap fiber at 850 nm wavelength," *Optics Express*, vol. 11, no. 14, p. 1613, 2003.
- [21] M. Wegmuller, M. Legré, N. Gisin, T. P. Hansen, C. Jakobsen, and J. Broeng, "Experimental investigation of the polarization properties of a hollow core photonic bandgap fiber for

1550 nm,” *Optics Express*, vol. 13, no. 5, p. 1457, 2005.

[22] F. Poletti, M. N. Petrovich, and D. J. Richardson, “Hollow-core photonic bandgap fibers: technology and applications,” *Nanophotonics*, vol. 2, no. 5–6, pp. 315–340, 2013.

[23] X. S. Yao and L. Maleki, “High frequency optical subcarrier generator,” *Electronics Letters*, vol. 30, no. 18, pp. 1525–1526, 1994.

[24] X. S. Yao and L. Maleki, “Converting light into spectrally pure microwave oscillation,” *Optics letters*, vol. 21, no. 7, pp. 483–485, 1996.

[25] D. Eliyahu, D. Seidel, and L. Maleki, “Phase noise of a high performance OEO and an ultra low noise floor cross-correlation microwave photonic homodyne system,” in *2008 IEEE International Frequency Control Symposium, FCS*, Honolulu, HI, USA, 2008, pp. 811–814.

[26] X. S. Yao and L. Maleki, “A novel photonic oscillator,” *The Telecommunications and Data Acquisition Progress Report 42-122*, pp. 32–43, 1995.

[27] X. S. Yao and L. Maleki, “Multiloop optoelectronic oscillator,” *IEEE Journal of Quantum Electronics*, vol. 36, no. 1, pp. 79–84, 2000.

[28] I. Ozdur, D. Mandridis, N. Hoghooghi, and P. J. Delfyett, “Low noise optically tunable optoelectronic oscillator with Fabry-Perot etalon,” *Journal of Lightwave Technology*, vol. 28, no. 21, pp. 3100–3106, 2010.

[29] X. S. Yao, “High-quality microwave signal generation by use of Brillouin scattering in optical fibers,” *Optics Letters*, vol. 22, no. 17, pp. 1329–1331, 1997.

[30] M. Merklein, B. Stiller, I. V. Kabakova, U. S. Mutugala, K. Vu, S. J. Madden, B. J. Eggleton, and R. Slavík, “Widely tunable, low phase noise microwave source based on a photonic chip,” *Optics Letters*, vol. 41, no. 20, pp. 4633–4636, 2016.

[31] D. Eliyahu and L. Maleki, “Low phase noise and spurious level in multi-loop opto-electronic oscillators,” in *IEEE International Frequency Control Symposium and PDA Exhibition Jointly with the 17th European Frequency and Time Forum, 2003. Proceedings of the 2003*, Tampa, FL, USA, 2003, pp. 405–410.

[32] J. Yang, Y. Jin-Long, W. Yao-Tian, Z. Li-Tai, and Y. En-Ze, “An optical domain combined dual-loop optoelectronic oscillator,” *IEEE Photonics Technology Letters*, vol. 19, no. 11, pp. 807–809, 2007.

[33] W. Zhou and G. Blasche, “Injection-locked dual opto-electronic oscillator with ultra-low

List of References

phase noise and ultra-low spurious level," *IEEE Transactions on Microwave Theory and Techniques*, vol. 53, no. 3, pp. 929–933, 2005.

[34] X. S. Yao and L. Maleki, "Dual microwave and optical oscillator," *Optics letters*, vol. 22, no. 24, pp. 1867–1869, 1997.

[35] N. Yu, E. Salik, and L. Maleki, "Ultralow-noise mode-locked laser with coupled optoelectronic oscillator configuration," *Optics Letters*, vol. 30, no. 10, pp. 1231–1233, 2005.

[36] E. Salik, N. Yu, and L. Maleki, "An ultralow phase noise coupled optoelectronic oscillator," *IEEE Photonics Technology Letters*, vol. 19, no. 6, pp. 444–446, 2007.

[37] J. Lasri, P. Devgan, R. Tang, and P. Kumar, "Self-starting optoelectronic oscillator for generating ultra-low-jitter high-rate (10GHz or higher) optical pulses," *Optics Express*, vol. 11, no. 12, pp. 1430–1435, 2003.

[38] D. Eliyahu, K. Sariri, A. Kamran, and M. Tokhmakhian, "Improving short and long term frequency stability of the opto-electronic oscillator," in *Proceedings of the 2002 IEEE International Frequency Control Symposium and PDA Exhibition (Cat. No.02CH37234)*, New Orleans, LA, USA, 2002, pp. 580–583.

[39] T. Sakamoto, T. Kawanishi, and M. Izutsu, "Optoelectronic oscillator using a LiNbO₃ phase modulator for self-oscillating frequency comb generation," *Optics Letters*, vol. 31, no. 6, pp. 811–813, 2006.

[40] S. Pan and J. Yao, "A frequency-doubling optoelectronic oscillator using a polarization modulator," *IEEE Photonics Technology Letters*, vol. 21, no. 13, pp. 929–931, 2009.

[41] Z. Tang, S. Pan, D. Zhu, R. Guo, Y. Zhao, M. Pan, D. Ben, and J. Yao, "Tunable optoelectronic oscillator based on a polarization modulator and a chirped FBG," *IEEE Photonics Technology Letters*, vol. 24, no. 17, pp. 1487–1489, 2012.

[42] H. K. Sung, X. Zhao, E. K. Lau, D. Parekh, C. J. Chang-Hasnain, and M. C. Wu, "Optoelectronic oscillators using direct-modulated semiconductor lasers under strong optical injection," *IEEE Journal on Selected Topics in Quantum Electronics*, vol. 15, no. 3, pp. 572–577, 2009.

[43] V. S. Ilchenko, X. S. Yao, and L. Maleki, "High-Q microsphere cavity for laser stabilization and optoelectronic microwave oscillator," in *Proceedings of SPIE 3611, Laser Resonators II*, San Jose, CA, USA, 1999, vol. 3611, pp. 190–198.

- [44] K. Volyanskiy, P. Salzenstein, H. Tavernier, M. Pogurmirschi, Y. K. Chembo, and L. Larger, "Compact optoelectronic microwave oscillators using ultra-high Q whispering gallery mode disk-resonators and phase modulation," *Optics Express*, vol. 18, no. 21, pp. 22358–22363, 2010.
- [45] P. Del'Haye, A. Schliesser, O. Arcizet, T. Wilken, R. Holzwarth, and T. J. Kippenberg, "Optical frequency comb generation from a monolithic microresonator," *Nature*, vol. 450, no. 7173, pp. 1214–1217, 2007.
- [46] A. A. Savchenkov, V. S. Ilchenko, J. Byrd, W. Liang, D. Eliyahu, A. B. Matsko, D. Seidel, and L. Maleki, "Whispering-gallery mode based opto-electronic oscillators," in *2010 IEEE International Frequency Control Symposium*, Newport Beach, CA, USA, 2010, pp. 554–557.
- [47] X. S. Yao and L. Maleki, "Optoelectronic oscillator for photonic systems," *IEEE Journal of Quantum Electronics*, vol. 32, no. 7, pp. 1141–1149, 1996.
- [48] X. S. Yao and G. Lutes, "A high-speed photonic clock and carrier recovery device," *IEEE Photonics Technology Letters*, vol. 8, no. 5, pp. 688–690, 1996.
- [49] H. Tsuchida and M. Suzuki, "40-Gb/s optical clock recovery using an injection-locked optoelectronic oscillator," *IEEE Photonics Technology Letters*, vol. 17, no. 1, pp. 211–213, 2005.
- [50] J. Lasri, P. Devgan, R. Tang, and P. Kumar, "Ultralow timing jitter 40-Gb/s clock recovery using a self-starting optoelectronic oscillator," *IEEE Photonics Technology Letters*, vol. 16, no. 1, pp. 263–265, 2004.
- [51] Z. Tang and S. Pan, "Transmission of 3-Gb/s uncompressed HD video in a optoelectronic-oscillator-based radio over fiber link," in *2013 IEEE Topical Conference on Biomedical Wireless Technologies, Networks, and Sensing Systems*, Austin, TX, USA, 2013, pp. 142–144.
- [52] J. Tao, P. Wang, L. Huang, Y. Zhang, D. Chen, P. Xiang, J. Zheng, G. W. Lu, X. Chen, and T. Pu, "All-optical signal upconversion using optically-injected DFB laser and embedded optoelectronic oscillator for radio-over-fiber applications," in *2017 Optical Fiber Communications Conference and Exhibition (OFC)*, Los Angeles, CA, USA, 2017, pp. 1–3.
- [53] D. Lu, X. Zhao, C. Lou, and L. Huo, "Synchronized clock multiplication through optical subharmonic injection locking of an optoelectronic oscillator," *Optics Communications*, vol. 284, no. 12, pp. 2742–2746, 2011.

List of References

- [54] V. J. Urick, P. S. Devgan, J. D. McKinney, F. Bucholtz, and K. J. Williams, "Channelisation of radio-frequency signals using optoelectronic oscillator," *Electronics Letters*, vol. 45, no. 24, pp. 1242–1244, 2009.
- [55] P. S. Devgan, M. W. Pruessner, V. J. Urick, and K. J. Williams, "Detecting low-power RF signals using a multimode optoelectronic oscillator and integrated optical filter," *IEEE Photonics Technology Letters*, vol. 22, no. 3, pp. 152–154, 2010.
- [56] X. Xie, T. Sun, H. Peng, C. Zhang, P. Guo, L. Zhu, W. Hu, and Z. Chen, "Low-noise and broadband optical frequency comb generation based on an optoelectronic oscillator," *Optics Letters*, vol. 39, no. 4, pp. 785–788, 2014.
- [57] E. Rubiola, *Phase noise and frequency stability in oscillators*, 1st ed. Cambridge, UK: Cambridge University Press, 2009.
- [58] E. Rubiola, E. Salik, S. Huang, N. Yu, and L. Maleki, "Photonic-delay technique for phase-noise measurement of microwave oscillators," *Journal of the Optical Society of America B*, vol. 22, no. 5, pp. 987–997, 2005.
- [59] A. L. Lance, W. D. Seal, and F. Labaar, "Phase noise and AM noise measurements in the frequency domain," in *Infrared and Millimeter Waves*, vol. 11, Academic Press, 1984, pp. 239–289.
- [60] E. Salik, N. Yu, L. Maleki, and E. Rubiola, "Dual photonic-delay line cross correlation method for phase noise measurement," in *Proceedings of the 2004 IEEE International Frequency Control Symposium and Exposition*, 2004, Montreal, Quebec, Canada, 2004, pp. 303–306.
- [61] Fairview Microwave Inc., "SCE18110505 Data sheet." 2017.
- [62] Corning Inc., "Corning® SMF-28e+® Optical fiber product information." 2013.
- [63] Hewlett Packard, "Product note 11729C-2 Phase noise characterization of microwave oscillators." 1985.
- [64] E. Rubiola, "Tutorial on the double balanced mixer." 2006.
- [65] W. J. Riley, *NIST special publication 1065 Handbook of frequency stability analysis*. Boulder, CO, USA: National Institute of Standards and Technology, 2008.
- [66] D. Eliyahu, K. Sariri, J. Taylor, and L. Maleki, "Optoelectronic oscillator with improved phase noise and frequency stability," in *Proceedings of SPIE 4998, Photonic Integrated Systems*, San Jose, CA, USA, 2003, pp. 139–147.

[67] D. Hou, X. P. Xie, Y. L. Zhang, J. T. Wu, Z. Y. Chen, and J. Y. Zhao, "Highly stable wideband microwave extraction by synchronizing widely tunable optoelectronic oscillator with optical frequency comb.," *Scientific Reports*, vol. 3, p. 3509, 2013.

[68] Y. Zhang, D. Hou, and J. Zhao, "Long-term frequency stabilization of an optoelectronic oscillator using phase-locked loop," *Journal of Lightwave Technology*, vol. 32, no. 13, pp. 2408–2414, 2014.

[69] D. E. Gray, Ed., *American institute of physics handbook*, 3rd ed. New York, NY, USA: McGraw-Hill, 1957.

[70] M. Bousonville, M. K. Bock, M. Felber, T. Ladwig, T. Lamb, H. Schlarb, S. Schulz, C. Sydlo, S. Hunziker, P. Kownacki, and S. Jablonski, "New phase stable optical fiber," in *Beam Instrumentation Workshop 2012 (B/IW2012)*, Newport News, VA, USA, 2012, pp. 101–103.

[71] L. Thévenaz, Ed., *Advanced fiber optics: concepts and technology*, 1st ed. Lausanne, Switzerland: EPFL Press, 2011.

[72] F. Poli, A. Cucinotta, and S. Selleri, *Photonic crystal fibers: properties and applications*, 1st ed. Dordrecht, Netherlands: Springer, 2007.

[73] T. M. Monro, P. J. Bennett, N. G. R. Broderick, and D. J. Richardson, "Holey fibers with random cladding distributions," *Optics Letters*, vol. 25, no. 4, pp. 206–208, 2000.

[74] P. Yeh, A. Yariv, and E. Marom, "Theory of Bragg fiber*," *Journal of the Optical Society of America*, vol. 68, no. 9, pp. 1196–1201, 1978.

[75] N. M. Litchinitser, A. K. Abeeluck, C. Headley, and B. J. Eggleton, "Antiresonant reflecting photonic crystal optical waveguides," *Optics Letters*, vol. 27, no. 18, pp. 1592–1594, 2002.

[76] S. Février, B. Beaudou, and P. Viale, "Understanding origin of loss in large pitch hollow-core photonic crystal fibers and their design simplification," *Optics Express*, vol. 18, no. 5, pp. 5142–5150, 2010.

[77] F. Poletti, "Nested antiresonant nodeless hollow core fiber," *Optics Express*, vol. 22, no. 20, pp. 23807–23828, 2014.

[78] Y. Chen, Z. Liu, S. R. Sandoghchi, Jasion G T, T. D. Bradley, E. Numkam Fokoua, J. R. Hayes, N. V Wheeler, D. R. Gray, B. J. Mangan, R. Slavík, F. Poletti, M. N. Petrovich, and D. J. Richardson, "Multi-kilometer long, longitudinally uniform hollow core photonic bandgap fibers for broadband low latency data transmission," *Journal of Lightwave Technology*, vol.

List of References

34, no. 1, pp. 104–113, 2016.

[79] P. J. Roberts, F. Couny, H. Sabert, B. J. Mangan, D. P. Williams, L. Farr, M. W. Mason, A. Tomlinson, T. A. Birks, J. C. Knight, and P. St. J. Russell, “Ultimate low loss of hollow-core photonic crystal fibres,” *Optics Express*, vol. 13, no. 1, p. 236, 2005.

[80] D. C. Jones, C. R. Bennett, M. A. Smith, and A. M. Scott, “High-power beam transport through a hollow-core photonic bandgap fiber,” *Optics Letters*, vol. 39, no. 11, pp. 3122–3125, 2014.

[81] D. G. Ouzounov, F. R. Ahmad, D. Müller, N. Venkataraman, M. T. Gallagher, M. G. Thomas, J. Silcox, K. W. Koch, and A. L. Gaeta, “Generation of megawatt optical solitons in hollow-core photonic band-gap fibers,” *Science*, vol. 301, no. 5640, pp. 1702–1704, 2008.

[82] J. D. Shephard, J. D. C. Jones, D. P. Hand, G. Bouwmans, J. C. Knight, P. S. J. Russell, and B. J. Mangan, “High energy nanosecond laser pulses delivered single-mode through hollow-core PBG fibers,” *Optics Express*, vol. 12, no. 4, pp. 717–723, 2004.

[83] M. Kuschnerov, V. A. J. M. J. M. Sleiffer, Y. Chen, E. De Man, Y. Chen, Z. Liu, S. R. Sandoghchi, G. T. Jasion, T. Bradley, E. Numkam Fokoua, J. R. Hayes, N. V. Wheeler, D. R. Gray, R. Slavik, Y. Jung, N. L. Wong, B. J. Mangan, F. Poletti, *et al.*, “Data transmission through up to 74.8 km of hollow-core fiber with coherent and direct-detect transceivers,” in *2015 European Conference on Optical Communication (ECOC)*, Valencia, Spain, 2015, pp. 1–3.

[84] V. A. J. M. Sleiffer, Y. Jung, N. K. Baddela, J. Surof, M. Kuschnerov, V. Veljanovski, J. R. Hayes, N. V. Wheeler, E. R. Numkam Fokoua, J. P. Wooler, D. R. Gray, N. H. L. Wong, F. R. Parmigiani, S. U. Alam, M. N. Petrovich, F. Poletti, D. J. Richardson, and H. De Waardt, “High capacity mode-division multiplexed optical transmission in a novel 37-cell hollow-core photonic bandgap fiber,” *Journal of Lightwave Technology*, vol. 32, no. 4, pp. 854–863, 2014.

[85] F. Benabid, J. C. Knight, and P. S. J. Russell, “Particle levitation and guidance in hollow-core photonic crystal fiber,” *Optics Express*, vol. 10, no. 21, p. 1195, 2002.

[86] M. J. Renn, D. Montgomery, O. Vdovin, D. Z. Anderson, C. E. Wieman, and E. A. Cornell, “Laser-guided atoms in hollow-core optical fibers,” *Physical Review Letters*, vol. 75, no. 18, pp. 3253–3256, 1995.

[87] A. Ashkin and J. Dziedzic, “Optical trapping and manipulation of viruses and bacteria,”

Science, vol. 235, no. 4795, pp. 1517–1520, 1987.

[88] E. Higurashi, H. Ukita, H. Tanaka, and O. Ohguchi, “Optically induced rotation of anisotropic micro-objects fabricated by surface micromachining,” *Applied Physics Letters*, vol. 64, no. 17, pp. 2209–2210, 1994.

[89] D. Hall, B. Todd Huffman, and A. Weidberg, “The radiation induced attenuation of optical fibres below -20°C exposed to lifetime HL-LHC doses at a dose rate of 700 Gy(Si)/hr,” *Journal of Instrumentation*, vol. 7, no. 1, p. C01047, 2012.

[90] L. Olanterä, C. Sigaud, J. Troska, F. Vasey, M. N. Petrovich, F. Poletti, N. V. Wheeler, J. P. Wooler, and D. J. Richardson, “Gamma irradiation of minimal latency hollow-core photonic bandgap fibres,” *Journal of Instrumentation*, vol. 8, no. 12, p. C12010, 2013.

[91] W. Jin, H. F. Xuan, and H. L. Ho, “Sensing with hollow-core photonic bandgap fibers,” *Measurement Science and Technology*, vol. 21, no. 9, p. 094014, 2010.

[92] T. Ritari, J. Tuominen, H. Ludvigsen, J. C. Petersen, T. Sørensen, T. P. Hansen, and H. R. Simonsen, “Gas sensing using air-guiding photonic bandgap fibers,” *Optics Express*, vol. 12, no. 17, pp. 4080–4087, 2004.

[93] A. M. Cubillas, J. Hald, and J. C. Petersen, “High resolution spectroscopy of ammonia in a hollow-core fiber,” *Optics express*, vol. 16, no. 6, pp. 3976–3985, 2008.

[94] J. A. Nwaboh, J. Hald, J. K. Lyngsø, J. C. Petersen, and O. Werhahn, “Measurements of CO₂ in a multipass cell and in a hollow-core photonic bandgap fiber at 2 μm,” *Applied Physics B: Lasers and Optics*, vol. 110, no. 2, pp. 187–194, 2013.

[95] F. Benabid, F. Couny, J. C. Knight, T. A. Birks, and Russell P St. J., “Compact, stable and efficient all-fibre gas cells using hollow-core photonic crystal fibres,” *Nature*, vol. 434, no. 7032, pp. 488–491, 2005.

[96] H. Xuan, W. Jin, J. Ju, H. L. Ho, M. Zhang, and Y. Liao, “Low-contrast photonic bandgap fibers and their potential applications in liquid-base sensors,” in *Proceedings of SPIE 6619, Third European Workshop on Optical Fibre Sensors*, Napoli, Italy, 2007, vol. 6619, p. 661936.

[97] Q. Shi, F. Lv, Z. Wang, L. Jin, J. Hu, Z. Liu, G. Kai, and X. Dong, “Environmentally stable Fabry-Pérot-type strain sensor based on hollow-core photonic bandgap fiber,” *IEEE Photonics Technology Letters*, vol. 20, no. 4, pp. 2008–2010, 2008.

List of References

- [98] M. Pang and W. Jin, "Detection of acoustic pressure with hollow-core photonic bandgap fiber," *Optics Express*, vol. 17, no. 13, pp. 11088–11097, 2009.
- [99] K. Saitoh and M. Koshiba, "Photonic bandgap fibers with high birefringence," *IEEE Photonics Technology Letters*, vol. 14, no. 9, pp. 1291–1293, 2002.
- [100] X. Chen, M. Li, N. Venkataraman, M. Gallagher, W. Wood, A. Crowley, J. Carberry, L. Zenteno, and K. Koch, "Highly birefringent hollow-core photonic bandgap fiber," *Optics express*, vol. 12, no. 16, pp. 3888–3893, 2004.
- [101] F. Poletti, N. G. R. Broderick, D. J. Richardson, and T. M. Monro, "The effect of core asymmetries on the polarization properties of hollow core photonic bandgap fibers," *Optics Express*, vol. 13, no. 22, p. 9115, 2005.
- [102] F. Loehl, V. Arsov, M. Felber, K. Hacker, B. Lorbeer, F. Ludwig, K. Matthiesen, H. Schlarb, B. Schmidt, A. Winter, S. Schulz, J. Zemella, J. Szewinski, and W. Jalmuzna, "Measurement and stabilization of the bunch arrival time at FLASH," in *Proceedings of the 11th European Particle Accelerator Conference (EPAC'08)*, Genoa, Italy, 2008, pp. 3360–3362.
- [103] M. Koivisto, M. Costa, J. Werner, K. Heiska, J. Talvitie, K. Leppanen, V. Koivunen, and M. Valkama, "Joint device positioning and clock synchronization in 5G ultra-dense networks," *IEEE Transactions on Wireless Communications*, vol. 16, no. 5, pp. 2866–2881, 2017.
- [104] S. Blin, H. K. Kim, M. J. F. Digonnet, and G. S. Kino, "Reduced thermal sensitivity of a fiber-optic gyroscope using an air-core photonic-bandgap fiber," *Journal of Lightwave Technology*, vol. 25, no. 3, pp. 861–865, 2007.
- [105] F. Kéfélian, H. Jiang, P. Lemonde, and G. Santarelli, "Ultralow-frequency-noise stabilization of a laser by locking to an optical fiber-delay line," *Optics letters*, vol. 34, no. 7, pp. 914–916, 2009.
- [106] J. Caron, J. Bézy, G. Courrèges-Lacoste, Bazalgette, B. Sierk, R. Meynart, M. Richert, and D. Loiseaux, "Polarization scramblers in earth observing spectrometers: lessons learned from Sentinel-4 and 5 phases A/B1," in *Proceedings of SPIE 10564, International Conference on Space Optics — ICSO 2012*, Ajaccio, Corsica, France, 2012, p. 105642B.
- [107] P. Schau, L. Fu, K. Frenner, M. Schäferling, H. Schweizer, H. Giessen, L. M. G. Venancio, and W. Osten, "Polarization scramblers with plasmonic meander-type metamaterials," *Optics Express*, vol. 20, no. 20, pp. 22700–22711, 2012.
- [108] J. B. Breckinridge, "Polarization properties of a grating spectrograph," *Applied Optics*, vol.

10, no. 2, pp. 286–294, 1971.

[109] J. P. McGuire and R. A. Chipman, “Analysis of spatial pseudodepolarizers in imaging systems,” *Optical Engineering*, vol. 29, no. 12, pp. 1478–1484, 1990.

[110] J. S. Wang, J. R. Costelloe, and R. H. Stolen, “Reduction of the degree of polarization of a laser diode with a fiber Lyot depolarizer,” *IEEE Photonics Technology Letters*, vol. 11, no. 11, pp. 1449–1451, 1999.

[111] W. K. Burns and A. D. Kersey, “Fiber-optic gyroscopes with depolarized Light,” *Journal of Lightwave Technology*, vol. 10, no. 7, pp. 992–999, 1992.

[112] X. Fang, “A variable-loop sagnac interferometer for distributed impact sensing,” *Journal of Lightwave Technology*, vol. 14, no. 10, pp. 2250–2254, 1996.

[113] R. Slavík, J. Homola, J. Tyroký, and E. Brynda, “Novel spectral fiber optic sensor based on surface plasmon resonance,” *Sensors and Actuators, B: Chemical*, vol. 74, no. 1–3, pp. 106–111, 2001.

[114] K. Takada, A. Himeno, K. Kato, and M. Okuno, “Development of fiber-optic depolarizer and its application to measurement systems for polarization-insensitive operation of silica-waveguide matrix switches,” *Journal of Lightwave Technology*, vol. 12, no. 9, pp. 1640–1647, 1994.

[115] Y. D. Gong, “Guideline for the design of a fiber optic distributed temperature and strain sensor,” *Optics Communications*, vol. 272, no. 1, pp. 227–237, 2007.

[116] T. Yang, C. Shu, and C. Lin, “Depolarization technique for wavelength conversion using four-wave mixing in a dispersion-flattened photonic crystal fiber,” *Optics Express*, vol. 13, no. 14, pp. 5409–5415, 2005.

[117] D. Clarke and J. Grainger, *Polarized light and optical measurement*, 1st ed. Oxford, UK: Pergamon press, 1971.

[118] W. K. Burns, “Degree of polarization in the Lyot depolarizer,” *Journal of Lightwave Technology*, vol. 1, no. 3, pp. 475–479, 1983.

[119] B. Lyot, “Recherche sur la polarisation de la lumière des planètes et de quelques substances terrestres,” *Annales de l'Observatoire de Paris (Meudon)*, vol. Tome VIII, no. Facs. I, 1929.

[120] W. Burns, R. P. Moeller, and C. Chen, “Depolarization in a single mode fiber,” *Journal of Lightwave Technology*, vol. LT-1, no. 1, pp. 44–50, 1983.

List of References

- [121] K. Bohm, K. Petermann, and E. Weidel, "Performance of Lyot depolarizers with birefringent single-mode fibers," *Journal of Lightwave Technology*, vol. LT-1, no. 1, pp. 71–74, 1983.
- [122] K. Takada, K. Okamoto, and J. Noda, "New fiber-optic depolarizer," *Journal of Lightwave Technology*, vol. LT-4, no. 2, pp. 213–219, 1986.
- [123] N. Azami, E. Villeneuve, A. Villeneuve, and F. Gonthier, "All-SOP all-fibre depolariser," *Electronics Letters*, vol. 39, no. 22, pp. 1573–1575, 2003.
- [124] K. Kim, H. -H Lee, C, and J. Lee, H, "Suppression of polarisation hole burning in an EDFA using an unpolarised source," *Electronics Letters*, vol. 31, no. 8, pp. 650–651.
- [125] S. Yamashita and K. Hotate, "Polarization-independent depolarizers for highly coherent light using faraday rotator mirrors," *Journal of Lightwave Technology*, vol. 15, no. 5, pp. 900–905, 1997.
- [126] B. Dörband, H. Müller, and H. Gross, *Handbook of optical systems, Volume 5: Metrology of optical components and systems*, 1st ed. Weinheim, Germany: WILEY-VCH Verlag GmbH & Co. KGaA, 2012.
- [127] M. Honma and T. Nose, "Liquid-crystal depolarizer consisting of randomly aligned hybrid orientation domains," *Applied Optics*, vol. 43, no. 24, pp. 4667–4671, 2004.
- [128] B.-Y. Wei, P. Chen, S.-J. Ge, L.-C. Zhang, W. Hu, and Y.-Q. Lu, "Liquid crystal depolarizer based on photoalignment technology," *Photonics Research*, vol. 4, no. 2, pp. 70–73, 2016.
- [129] B. H. Billings, "A monochromatic depolarizer," *Journal of the Optical Society of America*, vol. 41, no. 12, pp. 966–975, 1951.
- [130] R. Noe, M. Rehage, C. Harizi, and R. Ricken, "Depolariser based on acousto-optical TE-TM converters for suppression of polarisation holeburning in long haul EDFA links," *Electronics Letters*, vol. 30, no. 18, pp. 1500–1501, 1994.
- [131] F. Heismann, "Compact electro-optic polarization scramblers for optically amplified lightwave systems," *Journal of Lightwave Technology*, vol. 14, no. 8, pp. 1801–1814, 1996.
- [132] L. Yao, H. Huang, J. Chen, E. Tan, and A. Willner, "A novel scheme for achieving quasi-uniform rate polarization scrambling at 752 krad/s," *Optics Express*, vol. 20, no. 2, pp. 1691–1699, 2012.
- [133] A. D. Kersey and A. Dandridge, "Monomode fibre polarisation scrambler," *Electronics Letters*, vol. 23, no. 12, pp. 634–636, 1987.

[134] D. R. Lutz, "A passive fiber-optic depolarizer," *IEEE Photonics Technology Letters*, vol. 4, no. 4, pp. 463–465, 1993.

[135] M. Martinelli and C. Palais, J, "Dual fiber-ring depolarizer," *Journal of Lightwave Technology*, vol. 19, no. 6, pp. 899–905, 2001.

[136] I. Yoon, B. Lee, and S. Park, "A fiber depolarizer using polarization beam splitter loop structure for narrow linewidth light source," *IEEE Photonics Technology Letters*, vol. 18, no. 6, pp. 776–778, 2006.

[137] C. Wang, L. Li, and L. Peng, "One degree of freedom fiber ring depolarizer," *IEEE Photonics Technology Letters*, vol. 22, no. 12, pp. 911–913, 2010.

[138] L. Xiao, M. S. Demokan, W. Jin, Y. Wang, and C. L. Zhao, "Fusion splicing photonic crystal fibers and conventional single-mode fibers: Microhole collapse effect," *Journal of Lightwave Technology*, vol. 25, no. 11, pp. 3563–3574, 2007.

[139] J. Wooler, S. R. Sandoghchi, D. Gray, F. Poletti, M. N. Petrovich, N. V. Wheeler, N. K. Baddela, and D. Richardson, "Overcoming the challenges of splicing dissimilar diameter solid-core and hollow-core photonic band gap fibers," in *Workshop on Specialty Optical Fibers and their Applications*, (Optical Society of America, 2013), Sigtuna, Sweden, 2013, p. W3.26.

[140] L. N. Binh and N. Q. Ngo, "Active mode-locked fiber ring lasers: Implementation," in *Ultra-fast fiber lasers Principles and applications with MATLAB® models*, 1st ed., Boca Raton, FL, USA: CRC Press, 2010, pp. 71–102.

[141] J. Švarný, "Analysis of quadrature bias-point drift of Mach-Zehnder electro-optic modulator," in *2010 12th Biennial Baltic Electronics Conference*, Tallinn, Estonia, 2010, pp. 231–234.

[142] "ARDUINO," 2018. [Online]. Available: <https://www.arduino.cc/>. [Accessed: 16-Sep-2018].

[143] K. Saleh, A. Bouchier, P. H. Merrer, O. Llopis, and G. Cibiel, "Fiber ring resonator based opto-electronic oscillator - phase noise optimisation and thermal stability," in *Photonics West 2011*, San Francisco, CA, USA, 2011, p. 7936 79360A-1.

[144] G. A. Cranch and G. A. Miller, "Coherent light transmission properties of commercial photonic crystal hollow core optical fiber," *Applied Optics*, vol. 54, no. 31, pp. F8–F16, 2015.

List of References

[145] G. A. Miller and G. A. Cranch, "Reduction of intensity noise in hollow core optical fiber using angle-cleaved splices," *IEEE Photonics Technology Letters*, vol. 28, no. 4, pp. 414–417, 2016.

[146] O. Okusaga, J. P. Cahill, A. Docherty, C. R. Menyuk, W. Zhou, and G. M. Carter, "Suppression of Rayleigh-scattering-induced noise in OEOs," *Optics Express*, vol. 21, no. 19, pp. 22255–22262, 2013.

[147] U. S. Mutugala, J. Kim, T. D. Bradley, N. V. Wheeler, S. R. Sandoghchi, J. R. Hayes, E. Numkam Fokoua, F. Poletti, M. N. Petrovich, D. J. Richardson, and R. Slavík, "Optoelectronic oscillator incorporating hollow-core photonic bandgap fiber," *Optics Letters*, vol. 42, no. 13, pp. 2647–2650, 2017.

[148] U. S. Mutugala, J. Kim, T. D. Bradley, N. V. Wheeler, S. R. Sandoghchi, J. Hayes, E. Numkam-Fokoua, F. Poletti, M. N. Petrovich, D. J. Richardson, and R. Slavík, "Optoelectronic oscillator with low temperature induced frequency drift," in *2016 IEEE Photonics Conference (IPC)*, Waikoloa, HI, USA, 2017, pp. 270–271.

[149] D. Eliyahu, D. Seidel, and L. Maleki, "RF amplitude and phase-noise reduction of an optical link and an opto-electronic oscillator," *IEEE Transactions on Microwave Theory and Techniques*, vol. 56, no. 2, pp. 449–456, 2008.

[150] O. Okusaga, W. Zhou, J. Cahill, A. Docherty, and C. R. Menyuk, "Fiber-induced degradation in RF-over-fiber links," in *2012 IEEE International Frequency Control Symposium Proceedings*, Baltimore, MD, USA, 2012, pp. 1–5.

[151] U. S. Mutugala, E. R. Numkam Fokoua, Y. Chen, T. Bradley, S. R. Sandoghchi, G. T. Jasion, R. Curtis, M. N. Petrovich, F. Poletti, D. J. Richardson, and R. Slavík, "Hollow-core fibres for temperature-insensitive fibre optics and its demonstration in an optoelectronic oscillator," *Scientific Reports*, vol. 8, p. 18015, 2018.

[152] M. Martinelli, "A universal compensator for polarization changes induced by birefringence on a retracing beam," *Optics Communications*, vol. 72, no. 6, pp. 341–344, 1989.

[153] A. D. Kersey, M. J. Marrone, and M. A. Davis, "Polarisation-insensitive fibre optic Michelson interferometer," *Electronics Letters*, vol. 27, no. 6, pp. 518–520, 1991.

[154] K. Mochizuki, "Degree of polarization in jointed fibers: the Lyot depolarizer," *Applied Optics*, vol. 23, no. 19, pp. 3284–3288, 1984.

[155] P. L. Makowski, M. Z. Szymanski, and A. W. Domanski, "Lyot depolarizer in terms of the

theory of coherence—description for light of any spectrum,” *Applied Optics*, vol. 51, no. 5, pp. 626–634, 2012.

[156] L. Mandel and E. Wolf, *Optical coherence and quantum optics*, 1st ed. Cambridge, UK: Cambridge University Press, 1995.

[157] M. Born and E. Wolf, *Principles of optics*, 7th ed. Cambridge, UK: Cambridge University Press, 2005.

[158] J. Goodman, *Statistical Optics*, Classics. New York, NY, USA: Wiley, 2000.

[159] U. S. Mutugala, I. P. Giles, M. Ding, D. J. Richardson, and R. Slavík, “All-fiber passive alignment-free depolarizers capable of depolarizing narrow linewidth signals,” *Journal of Lightwave Technology*, vol. 37, no. 3, pp. 704–714, 2018.

[160] T. Okoshi, K. Kikuchi, and A. Nakayama, “Novel method for high resolution measurement of laser output spectrum,” *Electronics Letters*, vol. 16, no. 16, pp. 630–631, 1980.

[161] D. Derickson, Ed., *Fiber optic test and measurements*. Upper Saddle River, NJ, USA: Prentice Hall PTR., 1998.

[162] E. Hecht, *Optics*, 2nd ed. USA: Addison-Wesley publishing company, Inc., 1987.

[163] “Agilent 8509A/B lightwave polarization analyzer User’s guide.” Agilent Technologies, Santa Rosa, CA, USA, 2001.

[164] A. Al-Qasimi, O. Korotkova, D. James, and E. Wolf, “Definitions of the degree of polarization of a light beam,” *Optics Letters*, vol. 32, no. 9, pp. 1015–1016, 2007.

[165] R. Boudot and E. Rubiola, “Phase noise in RF and microwave amplifiers,” *IEEE Transactions on Ultrasonics, Ferroelectrics, and Frequency Control*, vol. 59, no. 12, pp. 2613–2624, 2012.